

# CHAPTER 1

## The NOvA experiment

The NuMI Off-axis  $\nu_e$  Appearance (NOvA) [1] experiment is a long-baseline neutrino oscillation experiment based at the Fermi National Accelerator Laboratory (Fermilab) [2]. NOvA receives an off-axis  $\nu_\mu$  and  $\bar{\nu}_\mu$  beam from Fermilab’s Neutrinos from the Main Injector (NuMI) neutrino source (Sec. 1.1) and measures  $\nu_e$  or  $\bar{\nu}_e$  appearance and  $\nu_\mu$  or  $\bar{\nu}_\mu$  disappearance between its two highly active and finely segmented detectors (Sec. 1.4) [3].

The capability to measure both  $\nu_e$  and the  $\bar{\nu}_e$  appearance, coupled with a significant matter effect induced by its long baseline, allows NOvA to address some of the most important questions in neutrino physics to date, such as the neutrino mass ordering, the octant of  $\theta_{23}$ , and the possible Charge conjugation - Parity (CP) symmetry violation in the neutrino sector [3–7]. NOvA data also enables measurements of  $\theta_{13}$ ,  $\theta_{23}$  and  $|\Delta m^2_{32}|$  [3], measurements of neutrino differential cross sections in the Near Detector (ND) [8–11], constraints on possible sterile neutrino models [12, 13], monitoring for supernova neutrino activity [14, 15], searches for magnetic monopoles [16], and constraints on the neutrino electromagnetic properties (this thesis). Using two functionally identical detectors mitigates the dominant systematic uncertainties of neutrino oscillation measurements, described in Sec. 1.8.

NOvA started taking data in February 2014 and is expected to run through 2026 [17], or until Fermilab begins redirecting its efforts towards the startup of the upcoming Deep Underground Neutrino Experiment (DUNE) experiment [18].

### 1.1 The Neutrino Beam

The neutrino beam for NOvA comes from the Fermilab-based NuMI neutrino source [19]. The schematic description of NuMI is shown in Fig. 1.1, starting on the left hand side with 120 GeV protons from the Main Injector (MI), part of the Fermilab accel-

erator complex. The proton beam is divided into  $10\ \mu\text{s}$  long pulses, with  $\sim 5 \times 10^{13}$  Protons On Target (POT) per spill every  $\sim 1.3\ \text{s}$  long cycle time, resulting in a proton beam power of  $\sim 800\ \text{kW}$  (current record  $959\ \text{kW}$  [20]), with upgrades currently underway to surpass  $1\ \text{MW}$  [21].

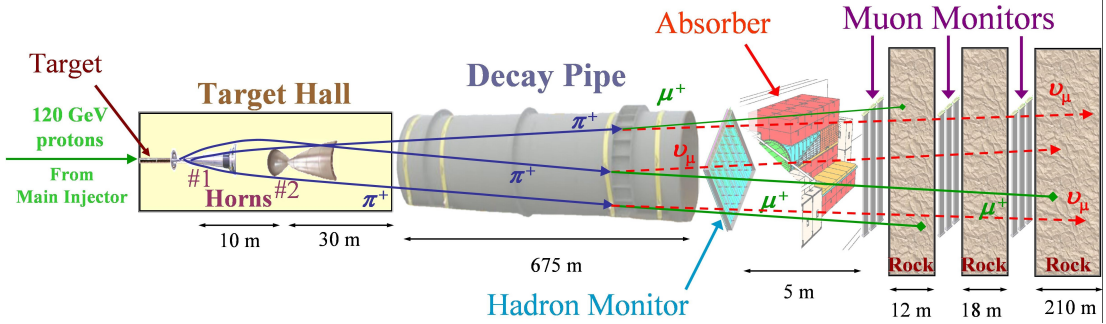


Figure 1.1: The NuMI neutrino beam starts on the left hand side with protons from the MI impinged on a graphite target producing mainly pions and kaons. These are then focused and charge-selected by two focusing horns, after which they decay inside the decay pipe into a high-purity  $\nu_\mu$  or  $\bar{\nu}_\mu$  beam. The residual hadrons are stopped and monitored in the hadron absorber and the remaining muons are recorded with muon monitors and absorbed inside the rock. Figure from [19].

The proton beam passes through a collimating baffle before hitting a  $\sim 1.2\ \text{m}$ -long (equal to about two interaction lengths) graphite target [22], producing hadrons, predominantly pions and kaons [19]. These are then focused and selected by two parabolic magnetic ‘horns’. The focused hadrons pass through a 675 m-long decay pipe filled with helium to create a low density environment for hadrons to propagate and decay in flight into either neutrinos or antineutrinos. High energy hadrons that do not decay in the decay pipe are absorbed within a massive aluminium, steel, and concrete hadron absorber and monitored with a hadron monitor. The leftover muons are ranged out in dolomite rock after the absorber and monitored using three muon monitors. The hadron and muon monitors are ionization chambers, used to monitor the quality, location and relative intensity of the beam.

Using a positive current inside the horns focuses positively charged particles, which then decay into neutrinos, and removes negatively charged particles. Reversing the horn current focuses negatively charged particles, which decay into antineutrinos, and defocuses positively charged particles. The neutrino mode is therefore called Forward Horn Current (FHC) and the antineutrino mode is called Reverse Horn Current (RHC). The composition of the neutrino beam for both these modes

at the **NOvA ND** is shown in Fig. 1.2, displaying the very high purity of the  $\nu_\mu$  or  $\bar{\nu}_\mu$  component in the **FHC** ro **RHC** beam respectively [19].

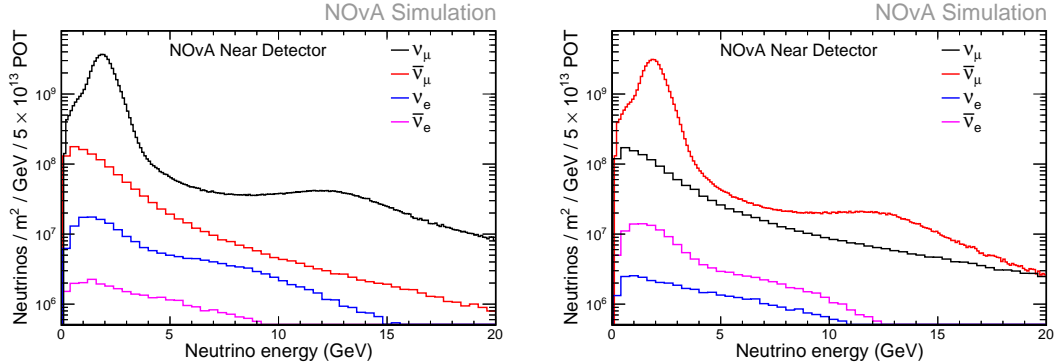


Figure 1.2: The components of the neutrino beam at the **NOvA ND** per one **NuMI** spill in the **FHC** regime shown on the left and the **RHC** regime on the right. The  $\nu_\mu$  ( $\bar{\nu}_\mu$ ) composition in the **FHC** (**RHC**) regime is 93.8% (92.5%), with a wrong sign contribution of 5.3% (6.6%) and only 0.9% (0.9%) contamination by  $\nu_e$  ( $\bar{\nu}_e$ ), showing the high purity of  $\nu_\mu$  and  $\bar{\nu}_\mu$  in the neutrino beam for **NOvA**. Beam composition values calculated for neutrinos with energies between 1 – 5 GeV. Figures are from internal **NOvA** repository [23].

The resulting neutrino beam energy distribution is peaked at  $\sim 7$  GeV with a wide energy band. However, thanks to the kinematics of the dominant pion decay, by placing the **NOvA ND** and Far Detector (FD) 14.6 mrad ( $\approx 0.8^\circ$ ) off the main **NuMI** beam axis, **NOvA** achieves a narrow band neutrino flux peaked at 1.8 GeV [7, 24], as can be seen in Fig. 1.3. Using an off-axis neutrino flux increases the neutrino beam around 2 GeV about 5-fold compared to the on-axis flux and narrow-band peak enhances background rejection for the  $\nu_e$  appearance analysis [24].

## 1.2 The **NOvA** Detectors

The two main **NOvA** detectors are the **ND**, located in **Fermilab**  $\sim 1$  km from the **NuMI** target and  $\sim 100$  m under ground, and the **FD**, located  $\sim 810$  km from **Fermilab** at Ash River in north Minnesota, partially underground with a rock overburden [24]. **NOvA** also operated a detector prototype called Near Detector on the Surface (NDOS), which was used for early research and development of detector components and analysis [4]. Additionally, **NOvA** operated a Test Beam detector, described in detail in Sec. ???. The scales of the **ND** and **FD** are shown in Fig. 1.4.

All **NOvA** detectors are highly segmented, highly active, functionally identical

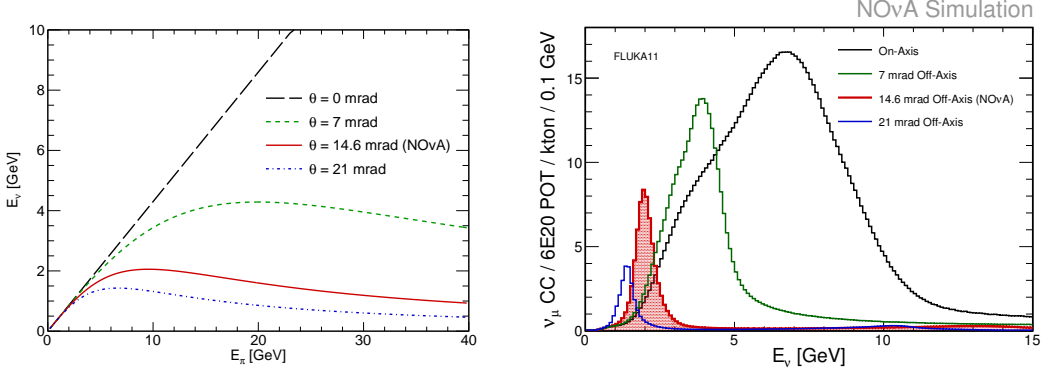


Figure 1.3: (Left) Dependence of the neutrino energy on the parent pion's energy and (right) neutrino energy distribution for an on-axis beam and three different off-axis beam designs. The case for **NOvA** is shown in red and results in a narrow neutrino energy distribution around 2 GeV, with limited dependence on the parent pion's energy. Figure from [24]

tracking calorimeters made up of Polyvinyl chloride (PVC) cells filled with liquid scintillator. Each cell is a long rectangular cuboid with depth of 5.9 cm and width of 3.8 cm (with some variations), with cell length extending to the full width/height of each detector, which is  $\sim 4.1$  m for the **ND** and  $\sim 15.6$  m for the **FD** [24]. An example of a **FD** cell is shown on the right of Fig. 1.4.

Cells are connected side-by-side into a 16 cell-wide extrusions with 3.3 mm-wide walls between cells and 4.9 mm-wide walls on the outsides of the extrusions. The first and last cell of each extrusion are  $\sim 3$  mm narrower than the rest of the cells. Two extrusions are connected side-by-side to form a 32 cell-wide module, with each module having a separate readout (see Sec. 1.3). In the **FD**, 12 modules are connected side-by-side to form one plane of the detector. In the **ND** only 3 modules make up a plane. Planes are positioned one after another, alternating between vertical and horizontal orientation, and grouped into diblocks, each containing 64 planes. The **FD** contains 14 diblocks, totalling 896 planes, whereas the **ND** contains 3 diblocks totalling 192 planes. The **ND** also contains a Muon Catcher region, positioned right after the active region, consisting of 22 planes of the normal **NOvA** detector design, 2 modules high and 3 modules wide, sandwiched with 10 steel plates to help range out muons mainly from the  $\nu_\mu$  charged current interactions [4, 24].

The **NOvA** coordinate system is centred with  $(0, 0, 0)$  in the centre of the first plane, relative to the beam direction. The x axis runs from left to right when facing the detector, y axis from bottom to top and z axis runs perpendicular to the planes

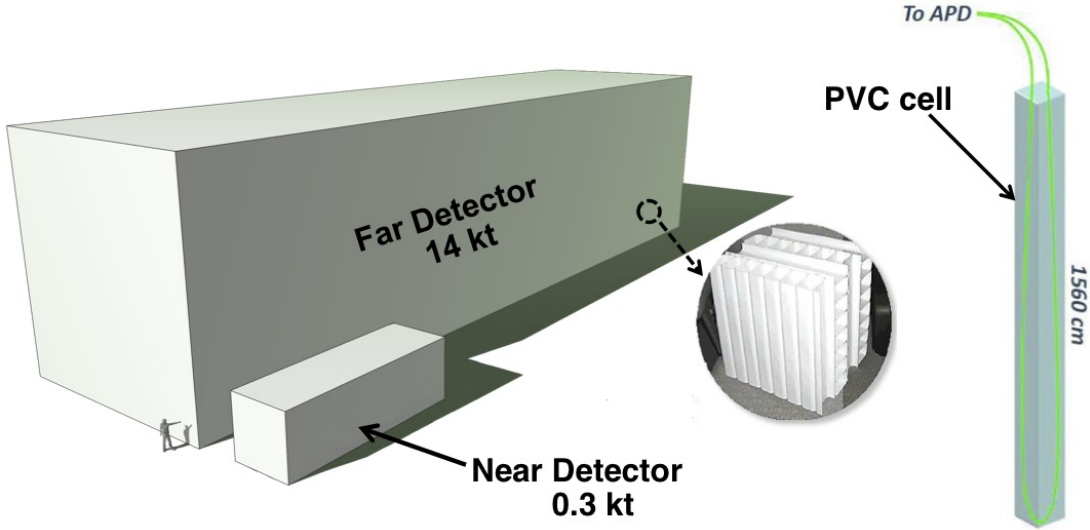


Figure 1.4: Schematic description of the scale and composition of the [NOvA ND](#) and [FD](#). The inset shows a photo of the orthogonal planes made out of [PVC](#) cells. An example of a [FD](#) cell containing liquid scintillator and a looped [WLS](#) fibre attached to an [APD](#) is shown on the right [25].

along the beam direction.

Each cell is filled with a liquid scintillator consisting of mineral oil with 4.1% pseudocumene as the scintillant [26]. Each cell contains a single wavelength shifting fibre with double the length of the cell, looping at one end and connecting to the readout at the other. The [PVC](#) walls of the cells are loaded with highly reflective titanium dioxide, with light typically bouncing off the [PVC](#) walls  $\sim 8$  times before being captured by the Wavelength Shifting (WLS) fibre [24].

The final dimensions of the [FD](#) are  $15.6\text{ m} \times 15.6\text{ m} \times 60\text{ m}$  with a total mass of 14 kT and for the [ND](#) the dimensions are  $3.8\text{ m} \times 3.8\text{ m} \times 12.8\text{ m}$  with a mass of about 0.3 kT [17]. The active volume, consisting only of the liquid scintillator without the [PVC](#) structure, makes up about 70% of the total detector volume [24].

The [NOvA](#) detectors are specifically designed for electromagnetic shower identification, with a radiation length of 38 cm, which amounts to  $\sim 7$  planes for particles travelling perpendicular to the detector planes [4]. This is particularly useful to distinguish electrons from  $\pi^0$ s.

We can calculate the minimum energy an electron needs to have to cross one cell (5.9 cm) of the [NOvA](#) detector by using the measured scintillator density  $0.86\text{ g/cm}^3$  [27], which gives us the required range of  $\sim 5\text{ g/cm}^2$ . Comparing this to measured values for the electron range [28] in the continuous slowing down approximation in

a Polyethylene (approximation of the NOvA scintillator [29]), gives us an estimate of the lowest detectable electron energy as  $E_e \gtrsim 10$  MeV.

### 1.3 Readout and Data Acquisition

The signal from the WLS fibres is read out by an Avalanche Photodiode (APD), converting the scintillation light into electrical signal, with a high quantum efficiency of  $\sim 85\%$  and a gain of 100 [24]. An example APD is shown in Fig. 1.5. Both ends of each fibre correspond to a single readout channel and are connected to one of the 32 pixels on the APD, organized in four rows of 8 pixels, with each APD reading out signal from one module. To maximise the signal to noise ratio, the APDs are cooled to  $-15^\circ\text{C}$  by a thermoelectric cooler, with heat carried away by a water cooling system.

The combination of the APD quantum efficiency and the light yield, determined by the PVC reflectivity and the scintillator and WLS fibre responses, result in a signal requirement of at least 20 Photo Electron (PE) in response to minimum ionizing radiation at the far end of the FD cell.

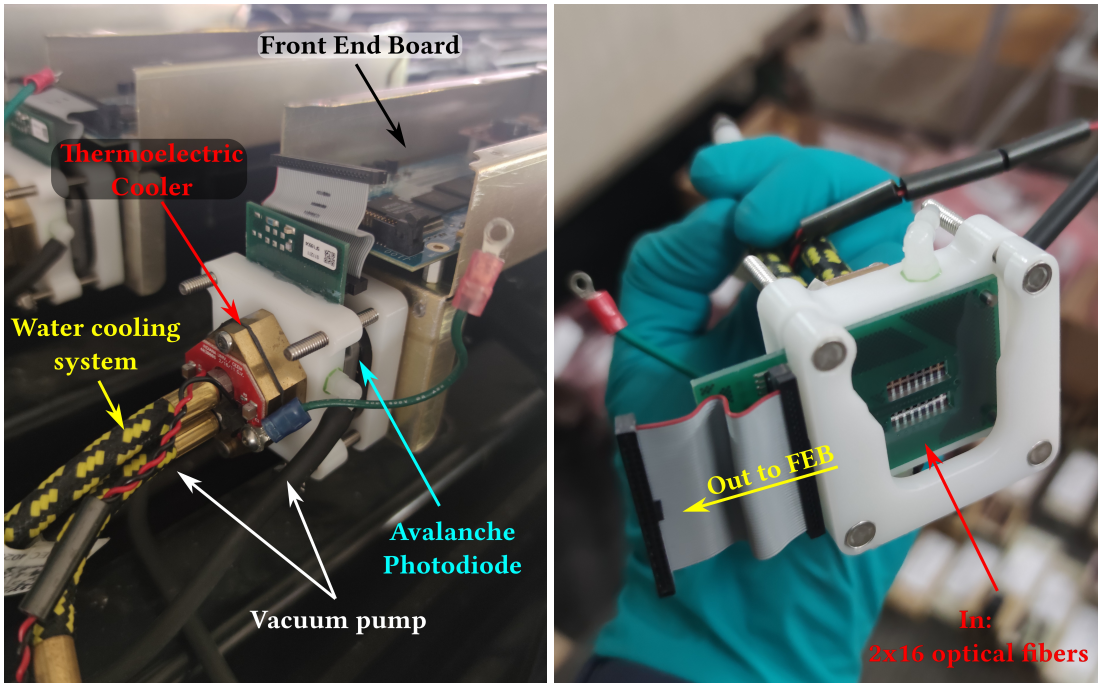


Figure 1.5: The modules with APDs for NOvA mounted on top of the detector on the left picture, and shown from the bottom on the right. The individual components of the module are described. The left picture shows a disconnected ribbon cable and ground cable, which are normally connected to the front end board.

Each APD is connected to a single Front End Board (FEB), shown in Fig. 1.6. The

FEB amplifies and integrates the **APD** signal, determines its amplitude and arrival time, before passing it to the Data Acquisition (DAQ) system. On the **FEB** the **APD** signal is first passed to a custom **NOvA** Application-Specific Integrated Circuit (ASIC), which is designed to maximize the detector sensitivity to small signals. **ASICs** amplify, shape and combine the signal, before sending it to an Analog-to-Digital Converter (ADC). The combined noise from the **APD** and the amplifier is equivalent to about 4 **PEs**, which, compared to an average **PE** yield from the far end of the **FD** cell of 30, results in a good signal and noise separation [24]. The digitized data from an **ADC** is sent to a Field Programmable Gate Array (FPGA), which extracts the time and amplitude of the **ADC** signals, while subtracting noise based on a settable threshold. The **FPGAs** employ multiple correlated sampling methods to reduce noise and improve time resolution of the signal [30].

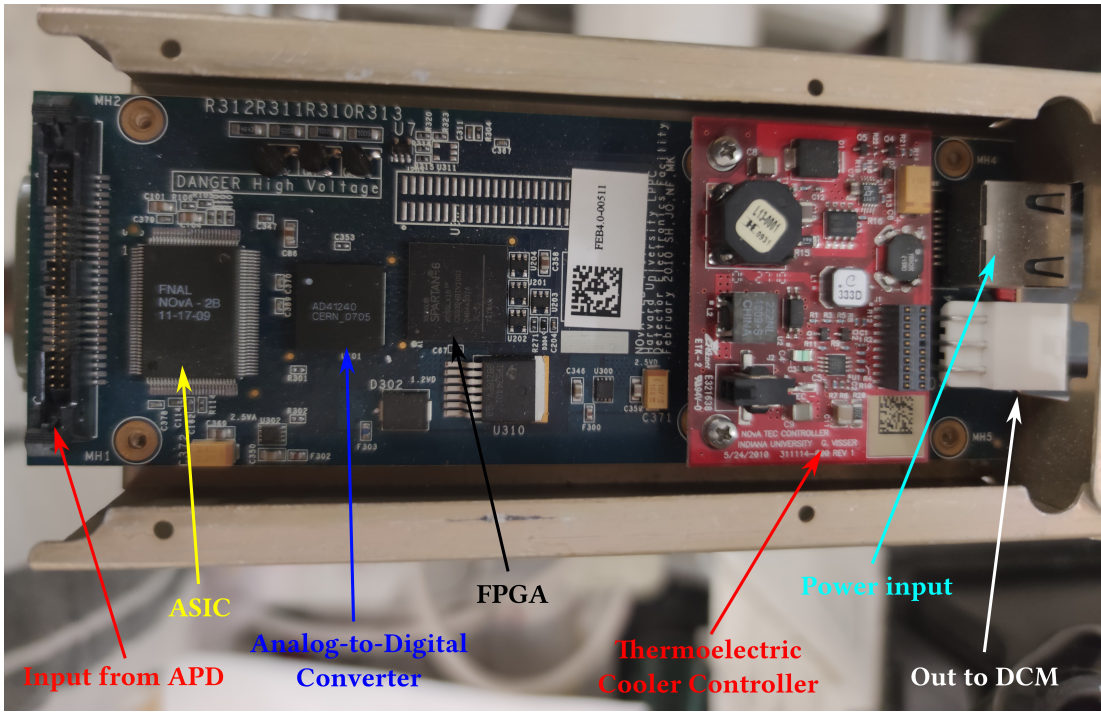


Figure 1.6: An example of a **NOvA** FEB with individual components labelled.

All of the **NOvA** front end electronics (**APDs** and **FEBs**) are operated in a continuous readout mode, without requiring any external triggers [24]. Due to higher detector activity during beam spills, the **ND FEBs** work at a higher frequency of 8 MHz, whereas the **FD FEBs** suffice with 2 MHz sampling frequency [30].

Data from up to 64 **FEBs** are concentrated in a Data Concentration Module (DCM), which concatenates and packages the data into 5 ms time slices, before sending it to

the buffer nodes. [DCMs](#) are also connected to the timing system and pass a single unified timing measurement to the [FEBs](#) to maintain synchronization across the detector [30].

The buffer nodes cache the data for at least 20 seconds while receiving information from the trigger system. Each trigger uses a time window based either on the time of the [NuMI](#) beam spill, on a periodic interval for monitoring and for the readout of cosmic events, or on one of the activity-based data-driven triggers [30]. Data that fall within any of the trigger windows are sent to a data logger system, where they are merged to form events, before being written to files for offline processing and sent to an online monitoring system. Files are organized based on a unique combination of run and subrun numbers, with runs corresponding to data taking periods with constant detector conditions and limited to either 64 subruns or 24 hours. Subruns are delineated either by a 2 GB file size constraint or a 1-hour timeout limit [31].

The detectors are continuously monitored to ensure data stability and quality. Subruns with suboptimal detector conditions or with events failing basic quality criteria are flagged as ‘bad’ and recorded in a ‘bad runs list’ [31]. Additionally, individual readout channel are assessed on a per-subrun basis, with those with too high or too low hit rates marked as ‘bad’ [32]. Both the ‘good runs’ list and the ‘bad channel’ maps are used to inform event processing and during simulation to emulate real detector conditions.

## 1.4 Simulation

To extract neutrino oscillation parameters, or to test a hypothesis, [NOvA](#) uses a series of simulations to make predictions according to various physical models [33]. The simulation chain can be divided into four parts: simulation of the neutrino beam, simulation of neutrino interactions within the [NOvA](#) detectors, simulation of cosmic particles interacting in the [NOvA](#) detector and simulation of the detector and readout response.

To simulate the neutrino beam, [NOvA](#) uses a simulation based on the GEANT4 v9.2.p03 [34] Monte Carlo (MC) event generator with a detailed model of the [NuMI](#) beamline [35], as described in Sec. 1.1. The simulation starts with the 120 GeV/c

[MI](#) protons interacting within the long carbon target and producing hadrons, mainly  $\pi$ ,  $K$  and secondary protons. This is followed by transport and possible further interaction of hadrons within the focusing system, until finally ending with hadron decays producing the neutrino beam.

To account for the inherently imprecise theoretical models used in GEANT4, [NOvA](#) uses the Package to Predict the Flux (PPFX) to incorporate external measurements of yields and cross sections of hadron interactions inside the target and the other [NuMI](#) materials into the neutrino beam prediction [36]. The current version of [PPFX](#) is limited by the results available during its creation and only corrects the most frequent interactions while assigning conservative systematic uncertainties to the rest (see Sec. 1.8). For the most common  $\pi$ ,  $K$  and  $p$  production, [PPFX](#) uses the NA49 measurements [37–39] of 158 GeV/c protons interacting on a thin (few percent of interaction length) carbon target. To expand the kinematic coverage, [PPFX](#) uses a few data points from Barton et al [40] for the  $\pi$  production and  $K/\pi$  ratios from the Main Injector Particle Production (MIPP) [41] experiment for the production of  $K$ . These results have to be scaled to the 20 – 120 GeV/c incident proton moment seen throughout [NuMI](#) using the FLUKA [42, 43] MC generator.

There are two new experiments that measure the production and interaction of hadrons on various targets and incident energies, specifically designed to improve the prediction of neutrino beams. The most impactful measurements from the NA61 experiment are of the 120 GeV/c protons on a thin carbon target [44–46], of the hadron incident interactions on various materials [47], and of the 120 GeV/c protons on a [NuMI](#) replica target [48]. The Fermilab-based EMPHATIC experiment [49] is currently analysing a broad range of hadron production and secondary and tertiary interaction measurements for neutrino beam prediction with a significant involvement of [NOvA](#) and [DUNE](#) collaborators.

The output of the neutrino beam simulation is passed to the simulation of neutrino interactions inside the detectors, which is done with the GENIE v3.0.6 [50] neutrino MC generator. GENIE allows users to choose the particular models for different types of neutrino interactions and particle propagation within the nucleus, as well as possible tunes to external measurements. The four main interaction modes in GENIE are the Quasi-Elastic (QE) Charged Current (CC) scattering, the Resonant baryon produc-

tion (Res), the Deep Inelastic Scattering (DIS), and the Coherent  $\pi$  (COH $\pi$ ) production. The special case of the two particle - two hole (2p2h) interaction via Meson Exchange Current (MEC) and the Final State Interaction (FSI) inside a nucleus are also considered. The initial state of the nucleus is represented by a local Fermi gas in the [QE](#) and 2p2h models, while a global relativistic Fermi gas is used for all other processes. All of these are set by the Comprehensive Model Configuration (CMC), which is currently N1810j0000 for [NOvA](#). Additionally, [NOvA](#) adds a costume tune to the [NOvA](#)  $\nu_\mu$ [CC](#) data for a better constraint of the [CCMEC](#) interactions. [NOvA](#) also uses a set of external  $\pi$  interaction measurements to constrain the [FSI](#) model. Table 1.1 shows the list of models and tunes for different interaction modes in [NOvA](#) [7].

Table 1.1: Models and tunes used in the [NOvA](#) simulation of neutrino interactions.

Interaction	Model	Tune
CCQE	València [51]	External $\nu - D$ data [52]
CCMEC	València [53, 54]	<a href="#">NOvA</a> $\nu_\mu$ <a href="#">CC</a> data
Res & COH $\pi$	Berger-Sehgal [55, 56]	External $\nu - A$ data
DIS	Bodek-Yang [57, 58]	External $\nu - A$ data
FSI	Semi-classical cascade [59]	External $\pi - {}^{12}C$ data

Since the [FD](#) is on the surface [NOvA](#) also uses a simulation of cosmic rays generated with the [MC](#) Cosmic-Ray Shower Generator (CRY) [60]. The simulated cosmic muons are also used to calibrate [NOvA](#) detectors [36].

Particles that are created from neutrino interactions and cosmic rays are propagated through the [NOvA](#) detectors using the GEANT4 v10.4.p02 [34], which outputs the energy deposited in the scintillator. This is then passed to a custom [NOvA](#) software of the light model [36], which calculates the amount of scintillation light produced for the deposited energy based on a Poisson distribution. The scintillation light production is parametrized using the Birks-Chou model [61], which corrects for the recombination in organic scintillators at high deposited energies. The scintillator light yield and the inherent production of the Cherenkov light, which can affect the light readout, are tuned to [NOvA](#) data [9]. The light collection by the [WLS](#) fibres, its transport to the [APDs](#), and the [APD](#) response use a parametrized simulation, as the [NOvA](#) cells and their readout are generally the same across the detectors [36]. The simulation of the readout electronics is done by another custom [NOvA](#) parametrized model, which accounts for random noise in the readout electronics and outputs true

events in the same format as the real data.

Due to the high neutrino rate in the **ND**, there are neutrinos interacting in the surrounding rock creating particles, mainly muons, that make it to the detector and act as background. However, since only a few ‘rock muons’ make it into the detector, it would be very time consuming to run a simulation which includes the rock around the **ND** for every neutrino. Instead, **NOvA** creates a separate simulation that includes the surrounding rock and then overlays these results into the nominal **NOvA** simulation chain to match the **NuMI** neutrino rate [36].

## 1.5 Data Processing and Event Reconstruction

Both data and simulation events for all **NOvA** detectors are passed through the same event reconstruction and particle identification algorithms. The reconstruction was specifically developed with the  $\nu_e$  appearance search in mind, focusing on identifying the  $\nu_e$ **CC** signal against the  $\nu_\mu$ **CC** and Neutral Current (NC) backgrounds. Each **NOvA** detector has to deal with different challenges, with multiple neutrinos interacting during one beam spill in the **ND**, and a large cosmic background in the **FD** [62].

The output from the **DAQ** system for each channel is called a *raw hit*. Hits are grouped into 550  $\mu\text{s}$ -long windows and passed to an offline reconstruction chain [62]. Reconstruction starts by grouping hits into *slices* based on their proximity to other hits in both time and space [63]. Slices are designed to ideally contain only a single neutrino interaction event.

For events that produce hadronic and electromagnetic showers, reconstruction first identifies straight lines through major features using a modified Hough transform [64], representing particle directions. These lines are passed to the Elastic Arms algorithm [65] to identify *vertex* candidates from their intersection points. Hits are then clustered into *prongs*, which are collections of hits with a start point, based on the vertex, and a direction, using a k-means algorithm called FuzzyK [66, 67]. Here ‘fuzzy’ means that each hit can belong to multiple prongs. Prongs are first created separately for each view (also called 2D prongs) and then, if possible, view-matched into 3D prongs (from here on referred to as prongs) [62]. Figure 1.7 shows an example of a simulated electron shower, where the reconstructed vertex is shown as a red

cross and the prong as a red shaded area. The prong groups together all the hits that are part of the shower, while removing the background hits, shown in grey.

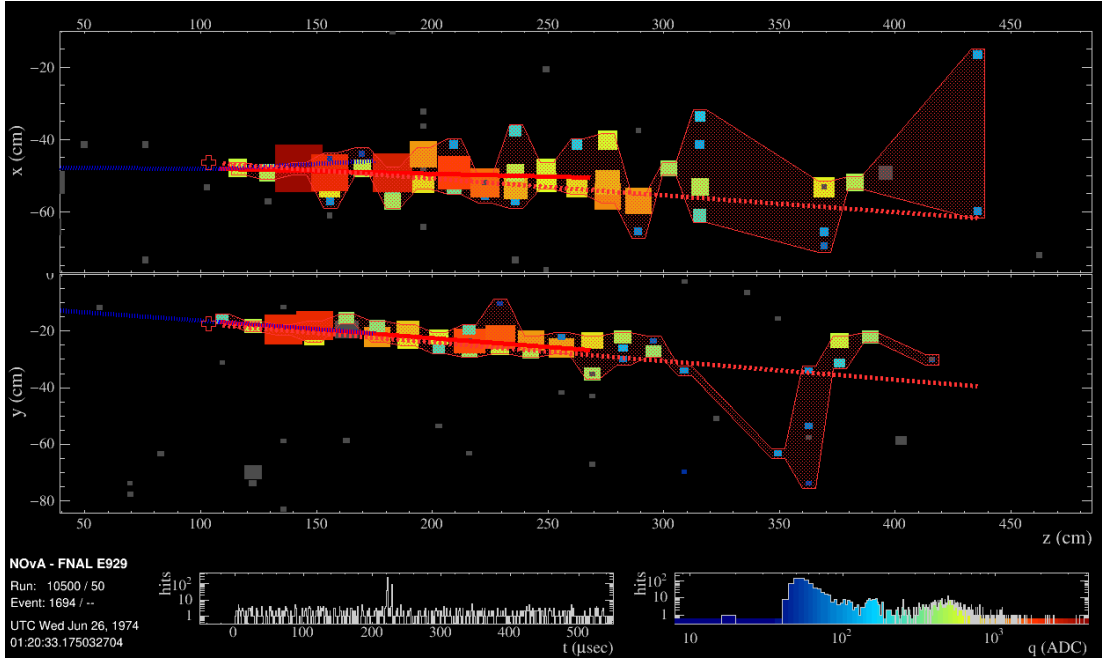


Figure 1.7: Reconstruction of a simulated single electron event in the NOvA ND. The red cross is the reconstructed vertex, the shaded area shows the cluster of hits into a prong and the dotted red line shows the estimated shower direction. The blue dotted line shows the true direct of the scattering neutrino and the solid red line the true momentum of the scattered electron. Figure from internal NOvA database [68].

For particles that are represented by tracks rather than showers (especially muons), the reconstruction takes the slice hits and forms ‘Kalman tracks’ based on a Kalman filter [69]. In addition to the start point and the direction, which exist also for prongs, tracks also contain information on the vector of trajectory points that make up the track and on the end point - and therefore on the track length. A parallel tracking algorithm takes in the Elastic Arms vertex and the Fuzzy-K prongs and forms Break Point Fitter (BPF) tracks [70, 71], using a model of Coulomb scattering and energy loss. BPF tracks also contain an information on the particle 4-momenta based on various particle assumptions, most notably the muon assumption. For cosmic particles, mostly muons, NOvA uses another track reconstruction algorithm, called ‘window cosmic track’ [72]. It uses a sliding 5 plane-long window, in which it fits a straight line to the recorded hits. The window starts from the end of the detector and then slides forward and repeats the fitting process until all hits are processed. This way it accounts for possible Coulomb scattering of cosmic muons. The intersection of each

cosmic track with the edge of the detector (or extrapolation of the track to the edge of the detector) is reconstructed as the ‘cosmic ray vertex’.

To identify individual particles and remove backgrounds, NOvA uses several Machine Learning (ML) algorithms, outputs of which are used in combination with the information from classical reconstruction algorithms for Particle Identification (PID). The most common topologies for particles interacting in NOvA detectors are shown in Fig. 1.8. Muons are easily identifiable as single long tracks which decay into an electron (or positron) if stopping inside of the detector. Both electrons and  $\pi^0$ 's produce electromagnetic showers, but thanks to the low-Z composition and high granularity of the detector, there is a gap between the interaction vertex and the electromagnetic shower for the  $\pi^0$ .

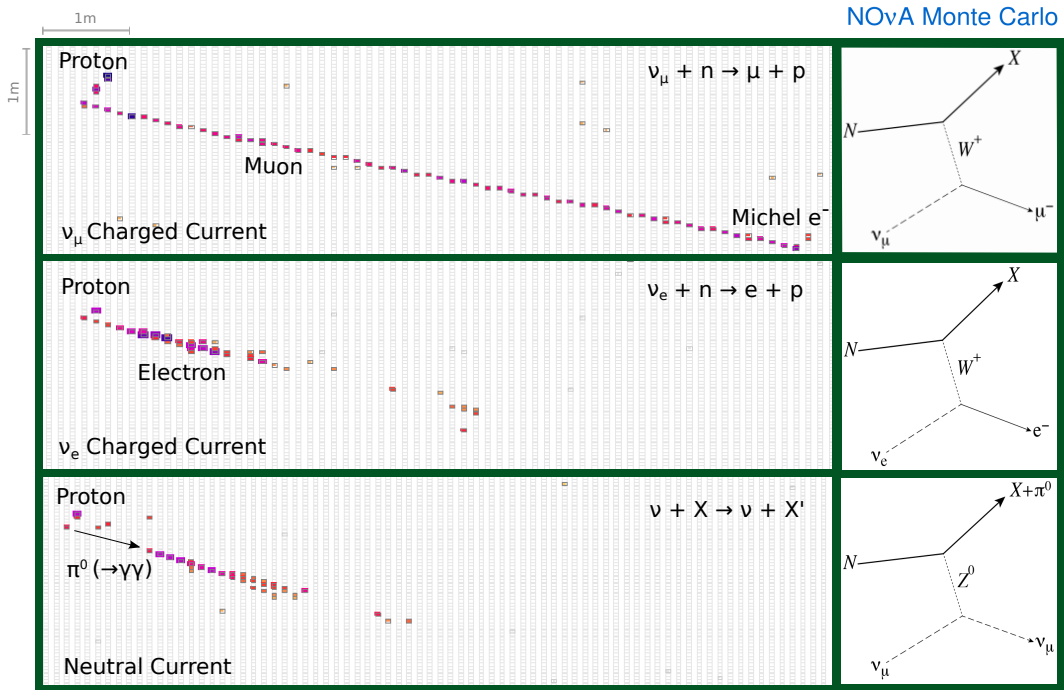


Figure 1.8: Different event topologies as seen in the NOvA detectors with corresponding Feynman diagrams [62]. Each event is a simulated 2.15 GeV neutrino interacting in a NOvA detector producing a 0.78 GeV proton and a second 1.86 GeV particle depending on the interactions type. The figure shows only one view and the colouring represents the deposited energy.

One of the ML algorithms that NOvA employs is a Convolutional Neural Network (CNN) based on the GoogLeNet [73] architecture named Convolutional Visual Network (CVN) [74]. When it is applied to identify entire events it is called *EventCVN* and uses slice hits to classify interactions into one of the five categories:  $\nu_e$ ,  $\nu_\mu$ ,  $\nu_\tau$ ,

**NC**, or cosmic. The same architecture, but applied to the Fuzzy-K prongs, is called *ProngCVN* [75], and is used to identify what particles the prongs most likely correspond to. This assignment is useful in calculation of prong energy, as described in Sec. 1.7. Another **ML** algorithm is specifically designed for identifying muons and is based on a Boosted Decision Tree (BDT). It is called Reconstructed Muon Identifier (ReMId) [69] and uses the reconstructed Kalman tracks as inputs.

## 1.6 Detector Calibration

The energy deposited within **NOvA** detectors is represented by the peak **ADC** values for each cell the particle passed through, obtained from the readout electronics, as described in Sec. 1.3. The conversion of the peak **ADC** values into physical units of energy requires calibrating the **NOvA** detectors [76], while accounting for the attenuation of light along the **WLS** fibres, or for differences between individual cells. The purpose of calibration is to calculate a conversion factor from  $\text{ADC} \rightarrow \text{MeV}$  for every part of the detector, so that the same energy deposited anywhere and at any time, is recorded as the same value of the reconstructed energy.

**NOvA** uses cosmic ray muons for calibration due to their abundance in the **NOvA** detectors and their consistent energy deposition. To calculate the absolute energy scale, **NOvA** selects a subsample of muons stopping inside of the detectors when they are almost exactly Minimum Ionising Particle (MIP) and therefore have a well understood energy deposition. The cosmic muons are collected using a periodic trigger with the same length as the beam trigger, whilst removing events with timestamps overlapping with the beam spill window. The simulation of cosmic muons is created using the **CRY** [60] **MC** generator, as outlined in Sec. 1.4.

Cosmic muon tracks are reconstructed using the window cosmic track algorithm described in Sec. 1.5. The selection of well reconstructed cosmic tracks requires that at least 80% of all hits from the reconstructed slice contribute to the track [29]. Each track must have at least 2 hits in both the x and y views and the difference in the number of planes the track crossed between the views must be at most 10% of the total number of planes. Also, the plane where each track starts or stops in one view must be within 3 planes of the start or stop plane in the other view. Additionally,

since tracks that do not cross many planes tend to not be reconstructed very well, the extent of each track in the z direction must be at least 70 cm and tracks must have at least 20% of their total track direction in the z axis. Tracks with on average more than 6 cells per plane and with path lengths through the cell larger than 10 cm are removed for the same reason. Furthermore, all the reconstructed tracks must start at most 10 cm from the edge inside of the detector and stop at most 10 cm outside of the detector. Lastly, tracks with trajectory points far away from each other are also removed. The selection of stopping muons for the absolute energy scale relies on identifying Michel electrons, which are produced by decaying muons at the end of their tracks, as can be seen on the top panel of Fig. 1.8.

Since the energy deposited in a cell is proportional to the distance the particle travels through the cell, the input variable for calibration is the deposited energy divided by the path length through the cell  $PE/cm$ . To ensure the path length is well calculated, all hits used in calibration must satisfy the so-called ‘tricell’ condition, shown in Fig. 1.9. This means that for each calibration hit, there must be a corresponding hit in both of the surrounding cells in the same plane for the same track. The path length can then be calculated simply from the height of the cell and the angle of the reconstructed track. In case there is a bad channel in a neighbouring cell (right side of Fig. 1.9), this channel is ignored and the tricell condition looks one cell further [76]. If the tricell condition fails, the hit can still pass the ‘z tricell’ condition, which is a longitudinal equivalent of the tricell condition and requires a hit in both the neighbouring planes in the same view and with the same cell number. The ‘z tricell’ hits are saved separately and may be used if there are no hits satisfying the original tricell condition. This is especially useful for the cells on the edge of the detector, which fail the tricell condition due to only having one neighbouring cell.

The calibration conversion factor from the signal recorded by the detector readout to the deposited energy can be expressed by as

$$E_{dep} \text{ [MeV]} = \text{Signal [ADC]} \times S_d \times TS_{d,i}^{\text{CALIB}} \times R_{d,i}(t) \times A_d(t). \quad (1.1)$$

The calibration scale therefore consists of four separate and complementary factors: the Scale ( $S_d$ ), the Threshold and Shielding correction ( $TS_{d,i}$ ), the Relative calibration ( $R_{d,i}(t)$ ) and the Absolute calibration ( $A_d(t)$ ), all described below. Each part is

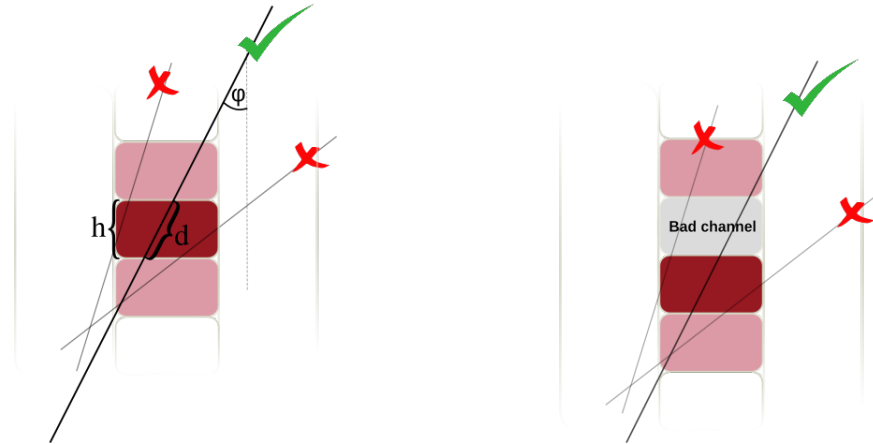


Figure 1.9: Illustration of the tricell condition. Only the hits with two surrounding hits in the same plane are used in the NOvA calibration, as shown on the left plot. This is to ensure a good quality of the path length ( $d$ ) reconstruction, which is calculated from the known cell height ( $h$ ) and the reconstructed track angle ( $\varphi$ ). In case the hit is next to a bad channel, as shown on the right plot, the bad channel is ignored and the tricell condition requires a hit in the next cell over.

calculated for each detector separately, as indicated by the subscript  $d$ . The threshold and shielding correction is only used during calibration and is omitted when applying the calibration results. The relative and absolute calibrations are calculated for each time period separately to account for possible changes in the energy deposition throughout the time, possibly caused by the ageing of the scintillator oil, or of the readout electronics. The time periods are either determined by a fixed time interval, or by running conditions separated by significant changes to the readout or the DAQ systems, including the summer shutdown.

The threshold and shielding correction and the relative calibration calculate a calibration factor for each position within the detector to account for variations caused by the attenuation of light as it travels through the WLS fibres, or by differences between individual cells. This is expressed with a subscript  $i$  in Eq. 1.1. For data, the position of a hit in the detector is described by the plane number, cell number and the position within the cell ( $w$ ).  $w$  is calculated as the projection of the cosmic track to the central cell axis and its value is equivalent to the x axis (y axis) coordinate of the projection for the horizontal (vertical) cells, with the 0 value at the centre of the cell [76].

For simulation, the calibration does not use the plane number to determine the position within a detector, as by construction all detector planes should have the same

readout. This significantly reduces the requirements for the number of events that need to be simulated, reconstructed, and calibrated, especially for the FD with 896 planes. However, in reality there are some variations in the detector response between individual planes, caused by different *brightness* qualities of the fibres, zipped or twisted fibres, different qualities of the scintillator, possible air bubbles, and potentially other factors. To include these differences in simulation without having to simulate every cell individually, all the cells are divided into 12 equally populated Fibre Brightness (FB) bins based on the uncorrected average response in the center of that cell, as shown in Fig. 1.10. These FB bins describe the relative differences in the detector response between individual cells [77].

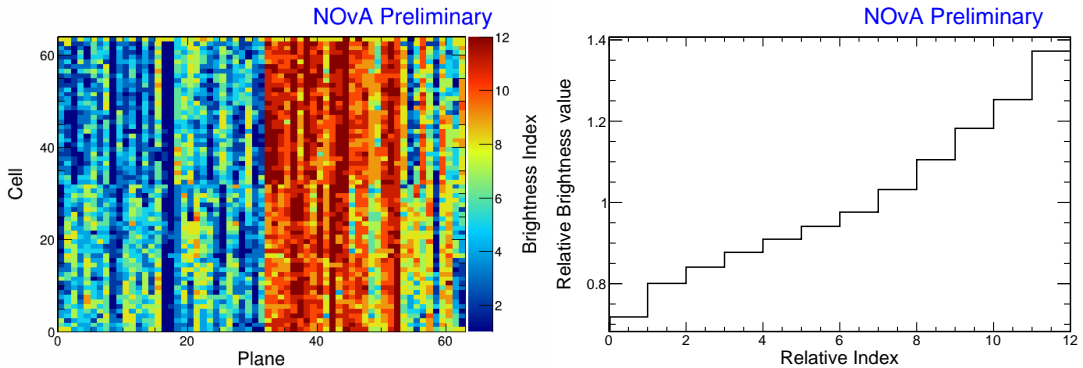


Figure 1.10: Distribution of the NOvA detector cells into 12 brightness bins (left plot), each representing a relative difference in energy response (right plot) due to different brightnesses of the fibres, scintillators, or readout. This is an example from the NOvA Test Beam detector, described in Sec. ??, where the left side of the detector (planes 1-32) has clearly lower response relative to the right side of the detector (planes 33-64).

### 1.6.1 Scale

The scale calibration factor from Eq. 1.1 is a simple conversion from the peak ADC value into the number of PEs. This factor only depends on the APD gain (which was different in the beginning of NOvA data taking) and on the FEB type (different between detectors, as described in Sec. 1.3).

### 1.6.2 Threshold and Shielding Correction

The threshold and shielding correction accounts for two assumptions, which hold true in most cases in NOvA, but fall short for some hits at the bottom of the detector, or far away from the readout, especially for the FD [76].

The first assumption is that the **ADC** response to the photon signal is linear, which is mostly true except close to the **APD** threshold. Energy deposited far away from the readout may produce photons that get attenuated enough to be shifted below the threshold. However, due to natural fluctuations of the number of photons created by the energy deposition, the same deposited energy may also produce photons that would make it over the threshold, therefore making it appear that the actual deposited energy was higher than in reality, introducing a bias to the calibration. The threshold correction is calculated using simulation, as the ratio between the mean of the Poisson distribution of the true number of the created **PE** ( $\text{PE}_{\text{Poisson}\lambda}$ ) and the number of the ‘reconstructed’ **PE** seen by the **APD** ( $\text{PE}_{\text{Reco}}$ ).

The second assumption is that the spectrum of cosmic muons is uniform within each detector. Again, this is generally true, but breaks down in the **FD**, which is big enough for the top of the detector to shield the bottom of the detector and therefore affect the energy distribution. The shielding correction is calculated from simulation as a ratio between the expected deposited energy if the particle was a **MIP** ( $E_{\text{MIP}}$ ), which is estimated from simulation for the **NOvA** scintillator as  $E_{\text{MIP}} = 1.78 \text{ MeV/cm}$  and the true deposited energy ( $E_{\text{true}}$ ).

The total threshold and shielding correction is calculated for simulated events in each cell, **FB** bin and  $w$  as

$$TS_i = \frac{\text{PE}_{\text{Poisson}\lambda}}{\text{PE}_{\text{Reco}}} \frac{E_{\text{MIP}}}{E_{\text{true}}}. \quad (1.2)$$

To ensure that the correction changes smoothly across each cell position, the final correction is calculated as a fit to the mean correction value along  $w$  in each cell and **FB** bin.

### 1.6.3 Relative Calibration

The main goal of the relative calibration is to correct for the attenuation of the scintillator light as it travels through the **WLS** fibre to the readout. The attenuation in each cell is estimated by performing an ‘attenuation fit’ to the mean response in **PE/cm**, as shown in Fig. 1.11. The relative calibration scale is then calculated as the ratio between the average response in **PE/cm** across the entire detector (can differ between

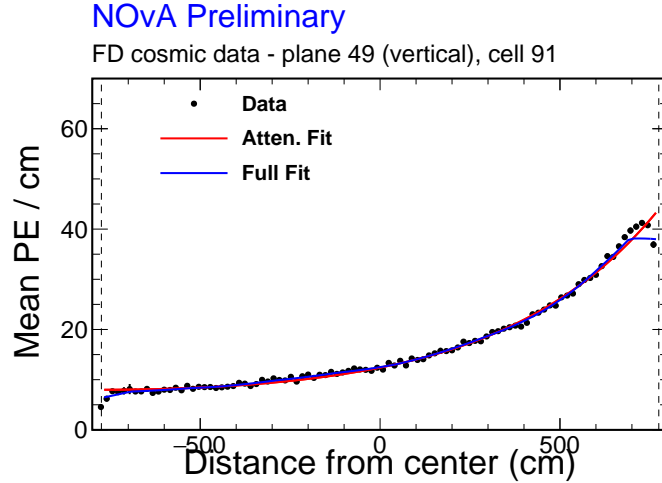


Figure 1.11: Example attenuation fit for a single cell in the NOvA FD across its full length, as shown by dashed vertical lines. The red line shows the initial exponential fit and the blue line shows the full fit after the LOWESS correction, both described in text. Figure from [78].

detectors) and the result of the attenuation fit in each particular position within the detector. The response after applying the relative calibration scale is expressed as Corrected Photo Electronss (PECorrs). Since the relative calibration scale is calculated for each cell independently, it effectively corrects for the relative differences between detector cells as well as for the attenuation. Therefore, the resulting distribution of PECorr/cm should be uniform across the detector, especially along the plane, cell and  $w$  [76].

The first step to do the attenuation fit is to create ‘attenuation profiles’ for each cell. Attenuation profiles are profile histograms of mean detector response over the path length through the cell, in the units of  $PE/cm$ , along the position within the cell. An example attenuation profile is shown in Fig. 1.11 as black dots. The threshold and shielding correction described in Sec. 1.6.2 is applied to the attenuation profiles before doing the attenuation fit, which consists of two steps.

1. The first step is a three-parameter exponential fit according to

$$y = C + A \left( \exp \left( \frac{w}{X} \right) + \exp \left( -\frac{L+w}{X} \right) \right), \quad (1.3)$$

where  $y$  is the fitted response,  $L$  is the length of the cell and  $C$ ,  $A$  and  $X$  are the fitted parameters representing the background, attenuation scale and atten-

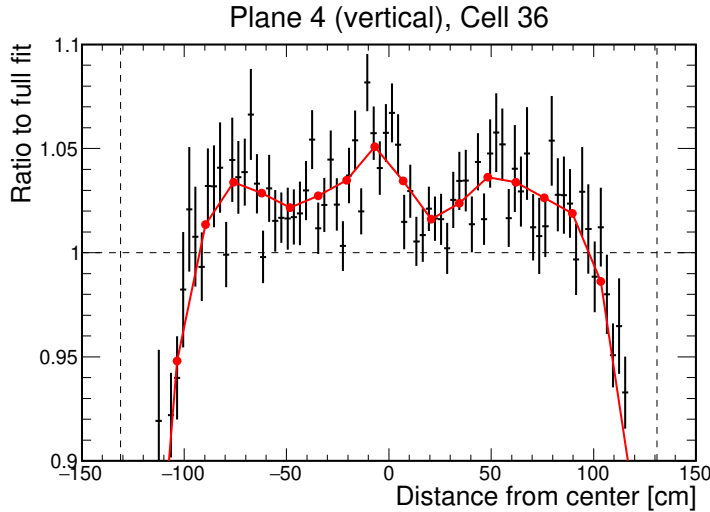


Figure 1.12: Example LOWESS correction for the residual differences after the exponential part of the attenuation fit of the NOvA relative calibration. This is an example for a single cell in the NOvA Test Beam detector with black points showing the residual differences and red line the LOWESS correction, both described in text.

uation length respectively. An example of the exponential fit is shown as a red curve in Fig. 1.11.

2. The second step is the smoothing out of residual differences between the exponential fit and the original distribution with the Locally Weighted Scatter plot Smoothing (LOWESS) method, shown in Fig. 1.12. The residual differences get evened out by creating a smooth distribution of 20 locally weighted points across the length of each cell. The result of the LOWESS correction is then combined with the exponential fit into the full attenuation fit, shown as a blue line in Fig. 1.11.

Even after applying the LOWESS correction, there are sometimes large differences between the attenuation fit and the fitted response. This is usually caused by a small number of events in that cell, common for cells at the edge of the detector. To ensure a good quality of the attenuation fit, the total  $\chi^2$  between the attenuation fit and the fitted response is calculated and only cells with the final  $\chi^2 \leq 0.2$  are counted as *calibrated*. Cells with  $\chi^2 > 0.2$  are ignored in further processing and marked as *uncalibrated*.

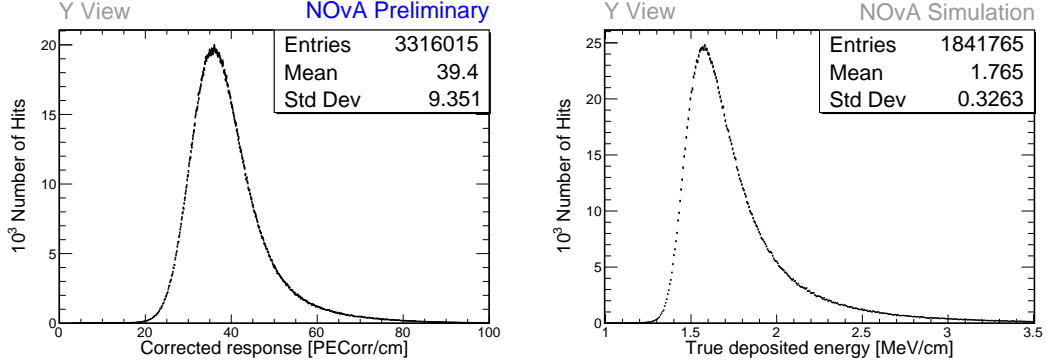


Figure 1.13: The absolute energy scale is calculated as the ratio between the simulated mean true deposited energy (right) and the mean reconstructed energy response (left) for selected stopping muons in each view and each data period or simulation.

#### 1.6.4 Absolute Calibration

The absolute calibration only uses hits from muons stopping inside of the detector, in a track window 1 – 2 m from the end of their tracks. This is when they are approximately MIP and their energy deposition is well understood. Additionally, hits at the edges of each cell are removed to mitigate the effects at the end of the WLS fibres and the lower number of events at the edge of the detector [29].

First, the relative calibration results are applied to the selected stopping muon hits to get a distribution of the corrected detector response in *PECorr*/cm, as shown on the left of Fig. 1.13. The mean of this distribution is called the *reconstructed Muon Energy Unit* (MEU) and is calculated separately in each of the two views, and in each time period or version of simulation. Analogously, the mean of the true deposited energy in MeV/cm from simulation, shown on the right of Fig. 1.13, is called the *true MEU*. The absolute energy scale (the absolute calibration scale) is then the ratio between the true and the reconstructed MEU value, where both the MEU values are taken as a simple average over the two views

$$\text{Absolute Energy Scale} = \frac{\text{MEU}_{\text{True}} \text{ [MeV/cm]}}{\text{MEU}_{\text{Reco}} \text{ [PECorr/cm]}}. \quad (1.4)$$

The values of the absolute energy scales for each data period and simulation, as well as the results of the attenuation fit, are saved in a set of lookup tables, which are then used any time a hit is recorded in the NOvA detector and processed and reconstructed with the NOvA algorithms described above.

## 1.7 Energy Estimation

The deposited energy from detector calibration (Sec. 1.6) is only the first step in estimating the neutrino energy ( $E_\nu$ ) required for the main **NOvA** analyses.

For the  $\nu_\mu$  disappearance analysis, the  $\nu_\mu$  energy is measured as the sum of the muon energy and the energy of the hadronic shower [7]. The muon energy is identified from the length of its track, without the need of the calibration results. The energy of the hadronic shower is estimated from simulation as a fit to the 2D distribution of the true  $\nu_\mu$  energy minus the reconstructed muon energy, versus the visible (not corrected for the dead material) deposited energy of the hadronic system [75].

For the  $\nu_e$  appearance analysis, the  $\nu_e$  energy is calculated using a quartic fit to the 2D distribution of the electromagnetic versus the hadronic calorimetric energies, both corrected for the energy deposition in the dead material (PVC cells) [75]. The dead material correction is currently just a simple scaling of the deposited energy from calibration for all particles and is calculated from the measurement of the  $\pi^0$  mass peak in the **NOvA ND**. This correction is correct only for electromagnetic showers and is not directly applicable to hadronic showers. The fit to determine the  $\nu_e$  energy keeps the normalization of both the electromagnetic and the hadronic energies free, so the exact value of the dead material correction is not important. It is however used in other, non-neutrino oscillation analyses.

## 1.8 Systematic Uncertainties

Systematic uncertainties in **NOvA** analyses arise from the imperfect knowledge on the individual components of the **NOvA** experiment, or from the known shortcomings of the prediction used to extract the measured parameters. Even though different analyses in **NOvA** need to consider different systematic uncertainties and their effect on the results varies, there are a few commonalities across all **NOvA** analyses that are explained below.

Both the 3-flavour [7] and the sterile neutrino [13] oscillation analyses in **NOvA** use the **ND** to constrain the **FD** prediction, which significantly reduces the effect of the neutrino beam and interaction prediction systematic uncertainties. On the other hand, these are the leading sources of systematic uncertainties for the **ND**-only anal-

yses, such as the cross section analyses [8–11]. The leading systematic uncertainty for the neutrino oscillation measurements comes from the detector calibration uncertainty. Significant uncertainties for all NOvA measurements also come from the neutron modelling, the detector simulation and the muon energy estimation. There are other sources of systematic uncertainties that are not mentioned here as they are sub-dominant, or specific to a certain analysis.

*TO DO: Mention here how are the systematics used - shifting the spectra and doing the full analysis ‘separately’ for each shifted prediction. Then we compare these shifted predictions with the nominal one*

The systematic uncertainty on the prediction of the neutrino beam consists of two parts: the hadron production and the beam focusing uncertainties [36]. The uncertainty for hadron production is estimated by the **PPFX** (describe in Sec. 1.4) using the multi-universe technique. Here we create 100 **PPFX** universes in which the inputs from the external measurements used to constrain the hadron production are randomly floated around their central values within their respective systematic uncertainties. Parts of the hadron production that are not constrained by external measurements are given a conservatively large systematic uncertainty. The beam focusing systematic uncertainties account for the uncertainties on the horn and target positions, the horn current, the beam position on the target, the beam spot size, and the effect of Earth’s magnetic field in the beam pipe. *TO DO: Describe the beam PCA and how can we limit the beam uncertainty*

*TO DO: Describe the neutrino interaction modelling systematic uncertainties* [3fl technote] There’s in total 77 neutrino interaction related systematic uncertainty knobs that are randomly varied during fitting. Only the ones that contribute are actually accepted during a fit.

*TO DO: Describe the detector modelling systematic uncertainties*

The systematic uncertainty arising from the simulation of the detector response can be divided into the scaling of the overall light level inside the simulation and of the Cherenkov light component.

The systematic uncertainty on the Cherenkov light scaling factor is calculated by profiling over the factor during the light model tune and taking the  $3\sigma$  confidence interval around the best fit value as the systematic uncertainty, resulting in a  $\pm 6.2\%$

relative uncertainty on the Cherenkov scaling factor. Similarly, the light level uncertainty was calculated by profiling over the light level scaling factor, resulting in a  $\pm 5\%$  relative uncertainty on the light level scaling factor.

*TO DO: Describe the neutron uncertainty - only if I decide I need it*

There are three systematic uncertainty arising from the calibration procedure: the absolute energy scale, the shape (relative residual variations along the cell, especially on its edges) and detector ageing.

Other standard candles are used to set the systematic uncertainty on the absolute energy scale. This is calculated as the difference between the data and simulation reconstructed energy for beam muons and protons in the ND, rock muons in the ND,  $\pi^0$  measurement in the ND and Michel electrons in the ND. These discrepancies drove the decision to set the systematic uncertainty on the absolute energy scale to 5 %. Measurements from the NOvA Test Beam experiment will help reduce this systematic uncertainty.

[3fl technote] The calibration shape systematic uncertainty was defined based on data/MC differences. The uncertainty was parameterized with a linear shape, with different slopes in the middle of the detector vs the edges, determined by linear fits to data/MC ratios.

[3fl technote] The detector ageing uncertainty is implemented as a simple linear drift downward in light level as a function of time, and a corresponding drift upward in the overall calibration scale to compensate. This is intended to mimic the impact of the number of hits above thresholds falling over time, while the overall calorimetric energy remains the same. For a more detailed summary, see Section 4.3 in the Prod5 detector simulation technote [2].

*TO DO: Describe the calibration uncertainties*

## CHAPTER 2

# Measuring the Muon Neutrino Magnetic Moment

In this analysis, I aim to detect a potential signal of the effective muon neutrino magnetic moment in the NOvA ND. This signal would manifest as an excess of neutrino-on-electron ( $\nu$ -on-e) elastic scattering interactions at low electron recoil energies, proportional to the value of the effective neutrino magnetic moment, over the Standard Model (SM) background. If no significant excess is observed, I will establish an upper limit on the effective muon neutrino magnetic moment.

Detecting the neutrino magnetic moment ( $\mu_\nu$ ) would provide a definitive evidence of new Beyond Standard Model (BSM) physics, and measuring its value would help identify the appropriate BSM theory. As current and planned experiments can only detect an anomalously large neutrino magnetic moment, observing such a signature would strongly suggest that neutrinos are Majorana particles and would have significant implications for astrophysics and cosmology [79].

The best model-independent experimental results on the neutrino magnetic moment come from experiments searching for dark matter using xenon-based detectors. These highly sensitive detectors detect solar neutrinos, which are part of the background in dark matter searches but can be reanalyzed for other purposes. In 2020, the XENON1T experiment observed [80] a low energy excess of solar neutrinos, which could correspond to a signal from an anomalously large effective magnetic moment within  $\mu_{\nu_\odot} \in (0.14, 0.29) \times 10^{-10} \mu_B$  at 90 % Confidence Level (C.L.), where  $\nu_\odot$  marks solar neutrinos. However, this result was disfavoured by the follow-up XENONnT experiment in 2022 [81], which saw no excess and set the current world-leading limit on neutrino magnetic moment at  $\mu_{\nu_\odot} < 0.063 \times 10^{-10} \mu_B$  at 90 % C.L.. Other solar neutrino experiments also reported null results regarding neutrino magnetic moment [82, 83], placing less stringent limits on its value. Given some basic assumptions [83, 84] this limit for solar neutrinos would correspond to a limit on muon neutrino

effective magnetic moment of  $\mu_{\nu_\mu} < 0.137 \times 10^{-10} \mu_B$ . However, the relationship between effective magnetic moments of different neutrino flavours may be non-trivial, especially in the context of possible new **BSM** physics, and studying muon neutrinos remains an important endeavour [85].

The best results for  $\nu_\mu$  and  $\bar{\nu}_\mu$  come from accelerator-based stopped pion neutrino sources [86, 87], which also do not observe any low energy excess and provide an upper limit on the effective muon neutrino magnetic moment of  $\mu_{\nu_\mu} < 6.8 \times 10^{-10} \mu_B$  at 90 % **C.L.** [86]. Stopped pion neutrino sources provide a well-understood beams made up of  $\nu_\mu$ ,  $\bar{\nu}_\mu$  and  $\nu_e$  with energies up to 52.8 MeV. Slightly looser limits come from pion decay-in-flight accelerator-based measurements (similar to **NOvA**) [88, 89], which provide a limit of  $\mu_{\nu_\mu} < 8.5 \times 10^{-10} \mu_B$  at 90 % **C.L..**

Thanks to the very intense and highly pure beam of muon neutrinos and antineutrinos, and a detector designed for the reconstruction and identification of events with electrons in the final state, **NOvA** is well-positioned to provide a highly competitive, and possibly even world-leading, measurement (or limit) of the effective muon neutrino magnetic moment. A previous analysis of **NOvA ND** data for a measurement of the effective muon neutrino magnetic moment was presented in a thesis [90], providing a (statistics-only) limit of  $\mu_{\nu_\mu} < 15.8 \times 10^{-10} \mu_B$  at 90 % **C.L..**

Additionally,  $\nu$ -on-e elastic scattering interactions are used in various other analyses in **NOvA**, specifically in efforts to constrain the neutrino beam prediction [91, 92] and in the search for Light Dark Matter (LDM) [93]. These analyses developed various tools and methods that can be utilized in the search for neutrino magnetic moment.

In this chapter, I will provide an overview of the theory of neutrino electromagnetic interactions in Sec. 2.1, focusing on the effective neutrino magnetic moment and its implications for  $\nu$ -on-e measurements and other theoretical considerations. In Sec. 2.2, I will discuss the analysis strategy, the signal and background definition, as well as the data and simulation samples and the analysis weights. Following this, Sec. 2.3 will explain the selection of events for this analysis, while Sec. 2.4 will address the relevant systematic uncertainties. I will present the results of this analysis in Sec. 2.5 and discuss their implications in Sec. 2.6. Finally, section 2.7 will summarise the findings of this analysis.

## 2.1 Theory of neutrino magnetic moment

As was described in Sec. ??, neutrinos in the [SM](#) are massless and electrically neutral particles. However, even [SM](#) neutrinos can have electromagnetic interaction through loop diagrams involving charged leptons and the W boson, covered by the neutrino charge radius [79].

In general [BSM](#) theories, considering interactions with a single photon as shown on Fig. 2.1, neutrino electromagnetic interactions can be described by an effective interaction Hamiltonian [94]

$$\mathcal{H}_{em}^{(\nu)}(x) = \sum_{k,j=1}^N \bar{\nu}_k(x) \Lambda_\mu^{kj} \nu_j(x) A^\mu(x). \quad (2.1)$$

Here  $\nu_k(x)$ ,  $k = 1, \dots, N$ , are neutrino fields in the mass basis with  $N$  neutrino mass states,  $\Lambda_\mu^{kj}$  is a general vertex function and  $A^\mu(x)$  is the electromagnetic field.

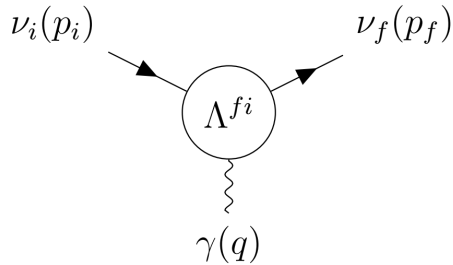


Figure 2.1: Effective coupling of neutrinos with one photon electromagnetic field.

The vertex function  $\Lambda_\mu^{fi}(q)$  is generally a matrix and, in the most general case consistent with the [SM](#) gauge invariance [95, 96], can be written in terms of linearly independent products of Dirac matrices ( $\gamma$ ) and only depends on the four momentum of the photon ( $q = p_f - p_i$ ):

$$\begin{aligned} \Lambda_\mu^{fi}(q) = & \mathbb{F}_1^{fi}(q^2) q_\mu + \mathbb{F}_2^{fi}(q^2) q_\mu \gamma_5 + \mathbb{F}_3^{fi}(q^2) \gamma_\mu + \mathbb{F}_4^{fi}(q^2) \gamma_\mu \gamma_5 + \\ & \mathbb{F}_5^{fi}(q^2) \sigma_{\mu\nu} q^\nu + \mathbb{F}_6^{fi}(q^2) \epsilon_{\mu\nu\rho\gamma} q^\nu \sigma^{\rho\gamma}, \end{aligned} \quad (2.2)$$

where  $\mathbb{F}_i^{fi}(q^2)$  are six Lorentz invariant form factors and  $\delta$  and  $\epsilon$  are the Dirac delta and the Levi-Civita symbols respectively.

Applying conditions of hermiticity  $(\mathcal{H}_{em}^{(\nu)\dagger} = \mathcal{H}_{em}^{(\nu)})$  and of the gauge invariance

of the electromagnetic field, the vertex function can be rewritten as

$$\Lambda_\mu^{fi}(q) = (\gamma_\mu - q_\mu q^2/q^2) \left[ \mathbb{F}_Q^{fi}(q^2) + \mathbb{F}_A^{fi}(q^2) q^2 \gamma_5 \right] - i\sigma_{\mu\nu} q^\nu \left[ \mathbb{F}_M^{fi}(q^2) + i\mathbb{F}_E^{fi}(q^2) \gamma_5 \right], \quad (2.3)$$

where  $\mathbb{F}_Q^{fi}$ ,  $\mathbb{F}_M^{fi}$ ,  $\mathbb{F}_E^{fi}$  and  $\mathbb{F}_A^{fi}$  are hermitian matrices representing the charge, dipole magnetic, dipole electric and anapole neutrino form factors respectively. It is clear that the vertex function only depends on the square of the four momentum of the photon  $q^2$ . In coupling with a real photon ( $q^2 = 0$ ) these form factors become the neutrino charge and magnetic, electric and anapole moments respectively. Additionally, the neutrino charge radius corresponds to the second term in the expansion of the charge form factor [94].

The above expression can be simplified [97] as

$$\Lambda_\mu^{fi}(q) = \gamma_\mu \left( Q_{\nu_{fi}} + \frac{q^2}{6} \langle r^2 \rangle_{\nu_{fi}} \right) - i\sigma_{\mu\nu} q^\nu \mu_{\nu_{fi}}, \quad (2.4)$$

where  $Q_{\nu_{fi}}$ ,  $\langle r^2 \rangle_{\nu_{fi}}$ , and  $\mu_{\nu_{fi}}$  are the neutrino charge, effective charge radius (also containing anapole moment), and an effective magnetic moment (also containing electric moment) respectively. This is possible thanks to the similar effects of the neutrino charge radius and the anapole moment, and of the neutrino magnetic and electric moments, on neutrino interactions. Therefore, these are the three neutrino electromagnetic properties (charge, effective charge radius and effective magnetic moment) measured in experiments.

The neutrino electric charge is primarily constrained through measurements of the neutrality of matter and cosmological observations, which provide much better constraints than neutrino oscillation experiments [94]. On the other hand, the neutrino charge radius would manifest as an increase in the size of the  $\nu$ -on-e elastic scattering coupling constants, allowing it to be studied in neutrino oscillation experiments such as NOvA. Additionally, the value of the neutrino charge radius in the SM is only an order of magnitude smaller than the current world-leading limits [98] and measuring it could either confirm the validity neutrino interactions in the SM, or open possibilities to non-standard contributions to neutrino scattering [94]. However, measurement of the neutrino charge radius is not part of this analysis, but may be included in the future re-analysis of the  $\nu$ -on-e interactions in the NOvA ND.

### 2.1.1 Neutrino electric and magnetic dipole moments

The size and effect of neutrino electromagnetic properties depend on the specific [BSM](#) theory applied. Evaluating one loop diagrams in the minimally extended [SM](#) with three right-handed Dirac neutrinos, as described in Sec. ??, gives the first approximation of the electric and magnetic moments, which are now  $3 \times 3$  matrices with elements:

$$\left. \begin{aligned} \mu_{kj}^D \\ i\epsilon_{kj}^D \end{aligned} \right\} \simeq \frac{3eG_F}{16\sqrt{2}\pi^2} (m_k \pm m_j) \left( \delta_{kj} - \frac{1}{2} \sum_{l=e,\mu,\tau} U_{lk}^\star U_{lj} \frac{m_l^2}{m_W^2} \right), \quad (2.5)$$

where  $m_k, m_j$  are the neutrino masses and  $m_l$  are the masses of charged leptons which appear in the loop diagrams [94]. The  $D$  superscript denotes Dirac neutrinos and  $M$  denotes Majorana neutrinos throughout this section. Also,  $e$  is the electron charge,  $G_F$  is the Fermi coupling constant, and  $U$  is the Pontecorvo-Maki-Nakagawa-Sakata (PMNS) neutrino oscillation matrix. Higher order electromagnetic corrections were neglected, but can also have a significant contribution, depending on the theory.

It can be seen that Dirac neutrinos have no diagonal electric moments ( $\epsilon_{kk}^D = 0$ ) and their diagonal magnetic moments are approximately

$$\mu_{kk}^D \simeq \frac{3eG_F m_k}{8\sqrt{2}\pi^2} \simeq 3.2 \times 10^{-19} \left( \frac{m_k}{\text{eV}} \right) \mu_B, \quad (2.6)$$

where  $\mu_B$  is the Bohr magneton which represents the value of the electron magnetic moment [94]. Neutrino magnetic moments are therefore strongly suppressed by the smallness of neutrino masses, with theoretical predictions in Eq. 2.6 several orders of magnitude below the reach of current experiments [97].

The transition magnetic moments in the minimally extended [SM](#) from Eq. 2.5 are suppressed with respect to the largest of the diagonal magnetic moments by at least a factor of  $10^{-4}$  due to the  $m_W^2$  in the denominator. The transition electric moments are even smaller due to the mass difference in Eq. 2.5. Therefore an experimental observation of a magnetic moment larger than in Eq. 2.6 would indicate physics beyond the minimally extended [SM](#) [94, 99].

The suppression of the neutrino magnetic moment by the smallness of its mass can be also expressed in a general case [99]. The ‘natural’ upper limits on the size

of the neutrino magnetic moment for any **BSM** theory that has New Physics (NP) generated at a scale  $\Lambda_{NP}$  can be expressed as [100]

$$\mu_\nu^D(\mu_B) \lesssim 3 \times 10^{-15} \frac{m_\nu^D \text{ (eV)}}{[\Lambda_{NP} \text{ (TeV)}]^2}. \quad (2.7)$$

Therefore for  $\Lambda_{NP} \simeq 1 \text{ TeV}$  and  $m_\nu^D \lesssim 1 \text{ eV}$  the limit becomes  $\mu_\nu^D \lesssim 3 \times 10^{-15} \mu_B$ , well below the current experimental capabilities. However, these upper bounds only apply if NP is generated well above the electroweak scale  $\Lambda_{EW} \sim 100 \text{ GeV}$  [94].

For Majorana neutrinos, the magnetic and electric form factors (and therefore the magnetic and electric moment matrices) are antisymmetric, thus Majorana neutrinos only have transition moments. The simplest extension of the **SM** that includes Majorana neutrinos requires either the addition of a Higgs triplet, or right-handed neutrinos together with a Higgs singlet [94]. Neglecting the Feynman diagrams which depend on the model of the scalar sector, the magnetic and electric dipole moments are

$$\left. \begin{aligned} \mu_{kj}^M \\ \epsilon_{kj}^D \end{aligned} \right\} \simeq \mp \frac{3ieG_F}{16\sqrt{2}\pi^2} (m_k \pm m_j) \sum_{l=e,\mu,\tau} \text{Im/Re} [U_{lk}^\star U_{lj}] \frac{m_l^2}{m_W^2}, \quad (2.8)$$

where Im is for  $\mu_{kj}^M$  and Re is for  $\epsilon_{kj}^D$ . These are difficult to compare to the Dirac case, due to possible presence of Majorana phases in the **PMNS** matrices, but it is clear that they have the same order of magnitude as Dirac transition dipole moments. However, the neglected model dependent contributions can enhance the transition dipole moments for Majorana neutrinos [94].

The natural upper bound on the Majorana magnetic moment is less strict compared to the Dirac neutrinos, due to the antisymmetric nature of Majorana magnetic moment, which requires an addition of additional Yukawa couplings into the **BSM** theory compared to Dirac neutrinos, which can enhance the maximal possible magnetic moment [99]. The limit for Majorana neutrinos can be expressed as

$$\mu_{\alpha\beta}^M(\mu_B) \leq 4 \times 10^{-9} \frac{[m_\nu^M]_{\alpha\beta} \text{ (eV)}}{[\Lambda_{NP} \text{ (TeV)}]^2} \frac{m_\tau^2}{|m_\alpha^2 - m_\beta^2|}, \quad \alpha, \beta \in \{e, \mu, \tau\}. \quad (2.9)$$

Here, the neutrino magnetic moment is expressed in the flavour basis instead of the mass basis, since the charged lepton masses are diagonal here. The two basis are

related by

$$\mu_{ij} = \sum_{\alpha\beta} \mu_{\alpha\beta} U_{\alpha i}^* U_{\beta j}. \quad (2.10)$$

and the effect of the neutrino magnetic moment on neutrino interactions does not depend on the choice of the basis[101].

These considerations imply, that if a magnetic moment  $\mu \gtrsim 10^{-15}\mu_B$  would be measured, neutrinos are almost certainly Majorana particles [99].

### Effective neutrino magnetic moment

As mentioned above, the neutrino magnetic moment that is measured in experiments is the so-called effective neutrino magnetic moment, which is a combination of electric and magnetic dipole moments and depends on neutrino source and oscillations. In the ultra-relativistic limit, the neutrino effective magnetic moment is

$$\mu_{\nu_l}^2(L, E_\nu) = \sum_j \left| \sum_k U_{lk}^* e^{\mp i \Delta m_{kj}^2 L / 2E_\nu} (\mu_{jk} - i\epsilon_{jk}) \right|^2, \quad (2.11)$$

where the minus sign in the exponent is for neutrinos and the plus sign for antineutrinos [94]. Therefore, the only difference between the effective neutrino and antineutrinos magnetic moment is in the phase induced by neutrino oscillations. For experiments with baselines short enough that neutrino oscillations would not have time to develop ( $\Delta m^2 L / 2E_\nu \ll \sim 1$ ), such as the NOvA ND, the effective magnetic moment is the same for neutrinos and antineutrinos and is independent of the neutrino energy.

Since the effective magnetic moment depends on the initial neutrino flavour, it is different for experiments studying neutrinos from different sources. Additionally, experiments such as solar neutrino experiments, need to include matter effects on the neutrino oscillations. Therefore the reports on the value (or upper limit) of the effective neutrino magnetic moment are not directly comparable between different types of neutrino experiments.

### 2.1.2 Measuring neutrino magnetic moment

The most sensitive method to measure neutrino magnetic moment is the low energy elastic scattering of (anti)neutrinos on electrons [94]. The diagram for this interaction is shown in Fig. 2.2 displaying the two observables, the recoil electron's kinetic energy ( $T_e = E_{e'} - m_e$ ) and the recoil angle with respect to the incoming neutrino beam ( $\theta$ ).

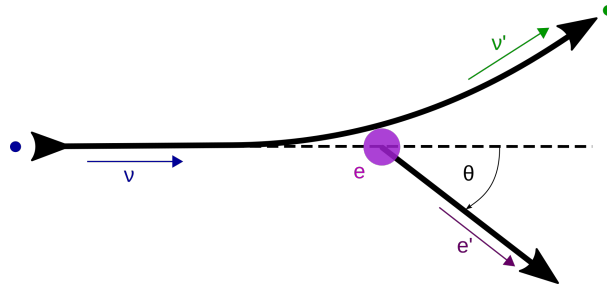


Figure 2.2: Neutrino-on-electron elastic scattering diagram

Since the  $\nu$ -on-e interaction is governed by simple  $2 \rightarrow 2$  kinematics, it is possible to get

$$(P_\nu - P_{e'})^2 = (P_{\nu'} - P_e)^2, \quad (2.12)$$

$$m_\nu^2 + m_e^2 - 2E_\nu E_{e'} + 2E_\nu p_{e'} \cos \theta = m_\nu^2 + m_e^2 - 2E_{\nu'} m_e. \quad (2.13)$$

From the energy conservation

$$E_\nu + m_e = E_{\nu'} + E_{e'} = E_{\nu'} + T_e + m_e \Rightarrow E_{\nu'} = E_\nu - T_e \quad (2.14)$$

follows

$$E_\nu p_{e'} \cos \theta = E_\nu E_{e'} - E_{\nu'} m_e = E_\nu (T_e + m_e) - (E_\nu - T_e) m_e = T_e (E_\nu + m_e), \quad (2.15)$$

$$\cos \theta = \frac{E_\nu + m_e}{E_\nu} \sqrt{\frac{T_e^2}{E_{e'}^2 - m_e^2}} = \frac{E_\nu + m_e}{E_\nu} \sqrt{\frac{T_e^2}{T_e^2 + 2T_e m_e}}. \quad (2.16)$$

And finally

$$\cos \theta = \frac{E_\nu + m_e}{E_\nu} \sqrt{\frac{T_e}{T_e + 2m_e}}. \quad (2.17)$$

Which can be rearranged to get

$$T_e = \frac{2m_e E_\nu^2 \cos^2 \theta}{(E_\nu + m_e)^2 - E_\nu^2 \cos^2 \theta}. \quad (2.18)$$

Electron's kinetic energy is therefore kinematically constrained by the energy conservation as

$$T_e \leq \frac{2E_\nu^2}{2E_\nu + m_e}, \quad (2.19)$$

which corresponds to the  $\cos \theta \rightarrow 1$  when the recoil electron goes exactly forward in the incident neutrino direction, as depicted in Fig. 2.3.

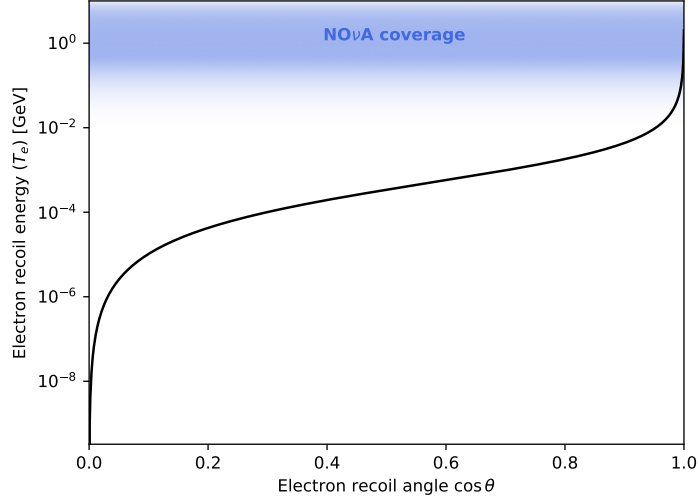


Figure 2.3: Relation between the recoil electron's kinetic energy and angle for the  $\nu$ -on-e elastic scattering. The coverage of the NOvA detectors for measuring the electron recoil energy is shown in blue. Only very forwards electron's are therefore recorded in NOvA.

Considering  $E_\nu \sim \text{GeV}$ , it is useful to approximate  $\frac{m_e^2}{E_\nu^2} \rightarrow 0$ . Additionally, considering only very small electron recoil angles, meaning  $\theta^2 \cong (1 - \cos^2 \theta)$ , applied to Eq. 2.17 results in

$$T_e \theta^2 \cong T_e \left( 1 - \left( \frac{E_\nu + m_e}{E_\nu} \right)^2 \frac{T_e}{T_e + 2m_e} \right) = T_e \left( 1 - \left( 1 + \frac{2m_e}{E_\nu} \right) \frac{T_e}{T_e + 2m_e} \right), \quad (2.20)$$

therefore

$$T_e \theta^2 \cong \frac{2m_e T_e}{T_e + 2m_e} \left( 1 - \frac{T_e}{E_\nu} \right) = 2m_e \left( \frac{1}{1 + \frac{2m_e}{T_e}} \right) \left( 1 - \frac{T_e}{E_\nu} \right), \quad (2.21)$$

and finally

$$T_e \theta^2 \cong 2m_e \left( 1 - \frac{T_e}{E_\nu} \right) < 2m_e. \quad (2.22)$$

This is a strong limit that very clearly distinguishes the  $\nu$ -on-e elastic scattering events from other similar interactions involving single electron (mainly the  $\nu_e$ CC interactions).

### Neutrino magnetic moment cross section

In the ultra-relativistic limit, the neutrino magnetic moment interaction flips the neutrino helicity, while the SM weak interaction conserves it, which means it is possible to add the two contribution to the total  $\nu$ -on-e cross section incoherently (without interference terms) [94]:

$$\frac{d\sigma_{\nu\text{-on-e}}}{dT_e} = \left( \frac{d\sigma_{\nu\text{-on-e}}}{dT_e} \right)_{\text{SM}} + \left( \frac{d\sigma_{\nu\text{-on-e}}}{dT_e} \right)_{\text{MAG}}. \quad (2.23)$$

The SM contribution can be expressed as [94, 102]:

$$\left( \frac{d\sigma_{\nu\text{-on-e}}}{dT_e} \right)_{\text{SM}} = \frac{2G_F^2 m_e}{\pi} \left\{ g_1^2 + g_2^2 \left( 1 - \frac{T_e}{E_\nu} \right)^2 - g_1 g_2 \frac{m_e T_e}{E_\nu^2} \right\}, \quad (2.24)$$

where the coupling constants  $g_1$  and  $g_2$  differ for between neutrino flavours and between neutrinos and antineutrinos. Their values are:

$$g_1^{\nu_e} = g_2^{\bar{\nu}_e} = \sin^2 \theta_W + 1/2, \quad g_2^{\nu_e} = g_1^{\bar{\nu}_e} = \sin^2 \theta_W, \quad (2.25)$$

$$g_1^{\nu_{\mu,\tau}} = g_2^{\bar{\nu}_{\mu,\tau}} = \sin^2 \theta_W - 1/2, \quad g_2^{\nu_{\mu,\tau}} = g_1^{\bar{\nu}_{\mu,\tau}} = \sin^2 \theta_W, \quad (2.26)$$

where  $\sin^2 \theta_W \cong 0.23$ .

The total SM cross section, and therefore the number of SM  $\nu$ -on-e interactions, depends on the neutrino energy and the minimum measured electron recoil energy. However, in general the cross section for for  $\nu_e$  is about 2.5 times larger than for the  $\bar{\nu}_e$ , about 6 times larger than for  $\nu_{\mu/\tau}$  and about 7 times larger than for  $\bar{\nu}_{\mu/\tau}$ .

The neutrino magnetic moment contribution is [94, 103]:

$$\left( \frac{d\sigma_{\nu\text{-on-e}}}{dT_e} \right)_{\text{MAG}} = \frac{\pi \alpha^2}{m_e^2} \left( \frac{1}{T_e} - \frac{1}{E_\nu} \right) \left( \frac{\mu_{\nu_l}}{\mu_B} \right)^2, \quad (2.27)$$

where  $\alpha$  is the fine structure constant and  $\mu_{\nu_l}$  is the effective magnetic moment of  $\nu_l$ . The total cross section now only depends on the neutrino energy and on the effective magnetic moment, but is the same for neutrinos and antineutrinos.

The comparison of the **SM** and the neutrino magnetic moment differential cross sections is shown in Fig.2.4. Whereas the **SM** cross section is approximately uniform for  $T_e \rightarrow 0$ , the neutrino magnetic moment cross section rises to infinity. However, this reach is limited by the experimental capabilities of detecting electrons with very low energies. The (possible) **NOvA** coverage is shown with a shaded blue region, with current capability reaching  $T_e = 0.5$  GeV. Future analyses might extend this reach to lower  $T_e$ , with the lowest possible detectable electron recoil energy  $T_{e,min} \approx 0.01$  GeV, as discussed in Sec. 1.2.

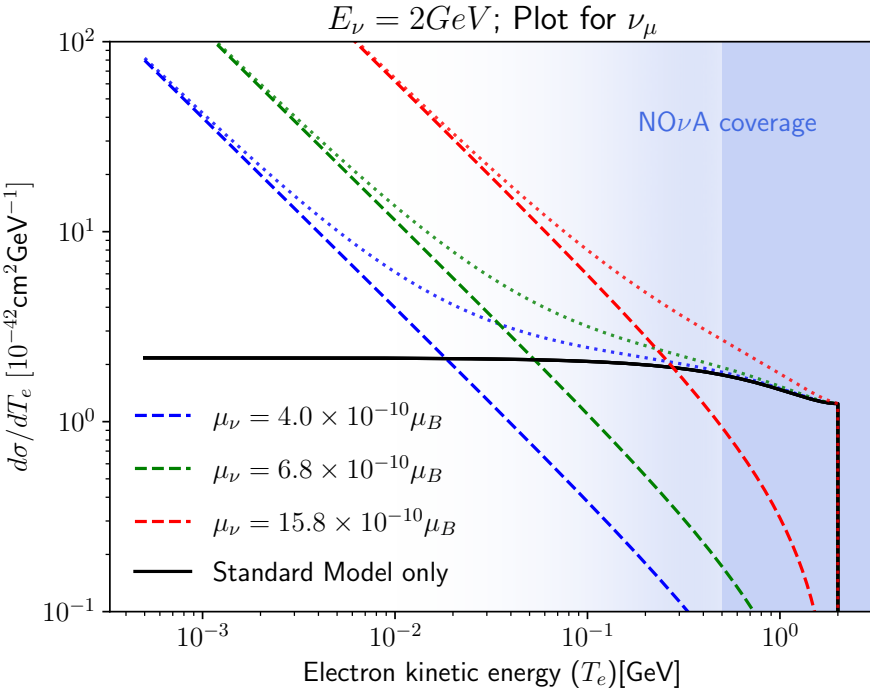


Figure 2.4: Comparison of the neutrino magnetic moment (coloured) and the **SM** (black) cross sections for the  $\nu$ -on-e elastic scattering. Different colours depict different values of the neutrino magnetic moment, with red corresponding to the previous **NOvA** measurement, green the LSND result, and blue a possible ultimate **NOvA** sensitivity, as discussed in the introduction to this chapter. Dashed lines are the individual cross sections and dotted lines are the added total cross section with the standard model contribution. **NOvA** coverage of electron recoil energies is shown in shaded blue.

Calculating the ratio of the neutrino magnetic moment and the **SM** cross sections, as shown in Fig. 2.5, can serve as a proxy to estimate the number of neutrino magnetic

moment events in relation to the predicted number of **SM** events, if the  $E_\nu$  and  $T_e$  are known. Additionally, comparing the ratio of the total cross sections can reveal the expected total number of neutrino magnetic moment events as a function of the predicted number of **SM** events. Considering  $E_\nu = 2 \text{ GeV}$ ,  $\mu_\nu = 6.8 \times 10^{-10} \mu_B$  (current best limit for  $\nu_\mu$  from LSND), and integrating differential cross sections for  $\nu_\mu$  in Eq. 2.24 and 2.27 from  $T_{e,min}$  to  $T_{e,max} \rightarrow 2 \text{ GeV}$  results in

$$\frac{\sigma_{\text{MAG}}}{\sigma_{\text{SM}}} \approx \begin{cases} 0.035 & T_{e,min} = 0.5 \text{ GeV}, \\ 0.14 & T_{e,min} = 0.01 \text{ GeV}. \end{cases} \quad (2.28)$$

Therefore, at the current **NOvA** detection capabilities, there are about 0.035 times as many neutrino magnetic moment  $\nu$ -on-e events than **SM** ones. This can be compared with the expected statistical uncertainty on the **SM** background, which in case of Poisson distributed events is the square root of the number of predicted events. Consequently, it is possible to assess the minimal number of **SM**  $\nu$ -on-e events necessary for the magnetic moment signal to be detected above the **SM** background (without considering systematic uncertainties) as

$$N_{\text{SM}} > 1/0.035^2 \approx 816. \quad (2.29)$$

However, this approximation is calculated only for one value of  $E_\nu$ , but can be used to assess the sensitivity of the experiment.

As can be seen in Fig. 2.4 and Fig. 2.5, the magnetic moment contribution exceeds the **SM** contribution for low enough  $T_e$ . This can be approximated as [94]:

$$T_e \lesssim \frac{\pi^2 \alpha^2}{G_F^2 m_e^3} \left( \frac{\mu_\nu}{\mu_B} \right)^2 \simeq 2.9 \times 10^{19} \left( \frac{\mu_\nu}{\mu_B} \right)^2 [\text{MeV}], \quad (2.30)$$

which does not depend on the neutrino energy. Therefore, experiments sensitive to lower energetic electrons are significantly more sensitive to the neutrino magnetic moment.

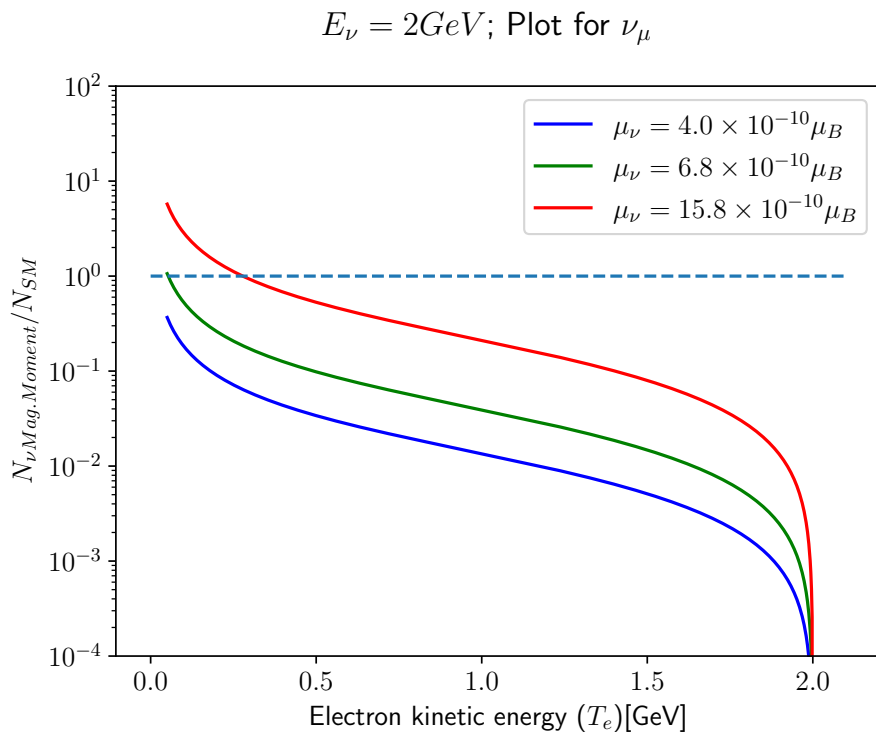


Figure 2.5: Ratio of the neutrino magnetic moment cross section to the SM cross section for the  $\nu$ -on-e elastic scattering of 2 GeV  $\nu_\mu$ . Different colours depict different effective muon neutrino magnetic moment values, with red corresponding to the previous NOvA measurement, green the LSND result, and blue a possible ultimate NOvA sensitivity, as discussed in the introduction to this chapter.

## 2.2 Analysis overview

Our analysis strategy for measuring the effective muon neutrino magnetic moment in the **NOvA ND** is based on comparing the total number of reconstructed and selected events in data with the prediction. The predicted events consist of the signal, which depends on the size of the effective muon neutrino magnetic moment, and of the background, which corresponds to the **SM**-only (null) hypothesis without any neutrino magnetic moment. We define the signal as true  $\nu$ -on-e elastic scattering interactions, created with the use of the neutrino magnetic moment cross section instead of the **SM** cross section, as described in Sec. 2.1.2. Additionally, the signal events are required to have their true interaction vertex contained within the **ND** to exclude events originating from outside of the detector.

The data used in this analysis were collected from the start of **NOvA ND** data taking on the August 22<sup>nd</sup>, 2014, until February 3<sup>rd</sup>, 2021. This is the **ND** data that were used in the latest **NOvA** neutrino oscillations result [7], with an additional year. Although more data have been collected since February 2021, they are still being processed and are not available at the time of writing this thesis. The total exposure of the data sample is approximately  $13.8 \times 10^{20}$  **POT**. This exposure is used throughout this chapter to scale the predicted distributions and number of events.

This analysis uses the standard **NOvA** simulation and reconstruction tools, as were discussed in Sec. 1.4 and 1.5. The simulation was created with approximately four times larger statistics than the data to limit statistical uncertainties from simulation. The total exposure for the simulation is approximately  $55.4 \times 10^{20}$  **POT**. For the systematic uncertainty studies only a portion of this full sample is used, specifically  $19.3 \times 10^{20}$  **POT**.

Corrections for known limitations in the simulation are applied in the form of analysis weights, which weight each event based on how it is affected by specific variations in the simulation. This includes the corrections for the neutrino beam prediction based on the external measurements used by the **PPFX** (Sec. 1.4), and, for the non- $\nu$ -on-e background only, also the internal and external measurements that constrain the neutrino interaction prediction inside **GENIE**.

The cross section corrections are not applied to the  $\nu$ -on-e events, as they are assumed to be known precisely from theory. However, the **GENIE MC** simulation only

considers tree-level SM  $\nu$ -on-e interactions [91], as described in Sec. 2.1.2, and doesn't account for any higher order terms, which are described by radiative corrections. Radiative correction can be expressed by two adjustments to the tree-level SM  $\nu$ -on-e cross section [104]. First, the values of the weak coupling constants are changed as [105]

$$g_1^{\nu_e} \rightarrow 0.7276, \quad g_1^{\nu_\mu} \rightarrow -0.2730, \quad g_2 \rightarrow 0.2334. \quad (2.31)$$

Second, there are additional terms added to the cross section equation. Considering only one-loop corrections, the full  $\nu$ -on-e cross section can be expressed as<sup>1</sup> [106]

$$\left( \frac{d\sigma_{\nu\text{-on-e}}}{dy} \right)_{\text{Rad. Corr.}} = \frac{G_F^2 s}{\pi} \left\{ g_1^2 \left( 1 + \frac{\alpha}{\pi} X_1 \right) + g_2^2 (1-y)^2 \left( 1 + \frac{\alpha}{\pi} X_2 \right) - g_1 g_2 \frac{m_e y}{E_\nu} \right\}, \quad (2.32)$$

where

$$y = \frac{T_e + E_\gamma}{E_\nu}, \quad (2.33)$$

$s = 2E_\nu m_e + m_e^2$  is the Mandelstam variable,

$$X_1 = -\frac{2}{3} \log \left( \frac{2yE_\nu}{m_e} \right) + \frac{y^2}{24} - \frac{5y}{12} - \frac{\pi^2}{6} + \frac{23}{72} \quad (2.34)$$

and

$$X_2 = -\frac{2}{3} (1-y)^2 \log \left( \frac{2yE_\nu}{m_e} \right) - \frac{y^2}{18} - \frac{\pi^2}{6} (1-y)^2 - \frac{2y}{9} + \frac{23}{72}. \quad (2.35)$$

In practice, radiative corrections can be implemented as a weight, where each true  $\nu$ -on-e event is weighted by a ratio

$$\text{weight}_{\text{Rad. Corr.}}(E_\nu, T_e) = \left( \frac{d\sigma_{\nu\text{-on-e}}}{dy} \right)_{\text{Rad. Corr.}} / \left( \frac{d\sigma_{\nu\text{-on-e}}}{dy} \right)_{\text{GENIE 3}}; \quad (2.36)$$

Analogically to the radiative correction weight, it is possible to create a neutrino magnetic moment weight as a ratio between the neutrino magnetic moment and the SM differential cross sections for the  $\nu$ -on-e interactions. This can then serve to predict the number of  $\nu$ -on-e events created by the neutrino magnetic moment interaction (which make up the signal), without the need for an additional simulation. This

---

<sup>1</sup>There is technically a third correction term  $X_3$  by the  $g_1 g_2$  term, which is however negligible for  $E_\nu \sim \text{GeV}$ .

is possible thanks to the theoretically very well understood properties of the  $\nu$ -on-e interaction, as described in Sec. 2.1.2. Therefore, the signal sample is created from the true  $\nu$ -on-e sample, with the magnetic moment weight applied. The weight has a form:

$$\text{weight}_{\nu\text{-Mag. Mom.}}(E_\nu, T_e) = \left( \frac{d\sigma_{\nu\text{-on-e}}}{dy} \right)_{\nu\text{-Mag. Mom.}} \Bigg/ \left( \frac{d\sigma_{\nu\text{-on-e}}}{dy} \right)_{\text{GENIE 3}}, \quad (2.37)$$

where

$$\left( \frac{d\sigma_{\nu\text{-on-e}}}{dy} \right)_{\nu\text{-Mag. Mom.}} = E_\nu \left( \frac{d\sigma_{\nu\text{-on-e}}}{dT_e} \right)_{\nu\text{-Mag. Mom.}}. \quad (2.38)$$

Due to the relatively low cross section of the  $\nu$ -on-e interaction, the nominal simulation sample contains very few  $\nu$ -on-e events, which could result in a significant statistical uncertainty from simulation. To avoid this, we created a  $\nu$ -on-e-enhanced simulation sample, which is mainly made up of  $\nu$ -on-e events with a total exposure of  $1.72 \times 10^{24}$  POT. There is a few non- $\nu$ -on-e background events overlaid on top of the  $\nu$ -on-e events to properly account for the possible reconstruction effects of the pileup of neutrino interactions in a single spill [91], since in the real detector, the hits from the true  $\nu$ -on-e interaction can be clustered together into another interaction, or additional hits can be clustered together into the  $\nu$ -on-e event. To save up on unnecessary disk space and processing usage, the enhanced  $\nu$ -on-e sample does not include any cross section related parameters and variables, as the  $\nu$ -on-e interaction is assumed to be known exactly from theory. Therefore, we do not apply cross section weights or account for cross section systematic uncertainties for  $\nu$ -on-e events.

The cross section tuning procedure in NOvA (Sec. 1.4) applies large weights to MEC events in some parts of the parameter space. However, after the full event selection (Sec. 2.3) only a small number of MEC events remain in the detector. This was shown to be an issue especially for the  $\nu_e$ CC MEC events [91]. Applying large tuning corrections to a small number of events results in large statistical fluctuations. To avoid this, we created another special sample with enhanced number of  $\nu_e$ CC MEC events, following the same procedure as for the  $\nu$ -on-e-enhanced sample, with an exposure of  $1.99 \times 10^{24}$  POT.

A summary of the simulation samples and analysis weights for the four different types of signal and background components is shown in Tab. 2.1. In the following

chapter, the  $\nu_e$ CC MEC background is added into the ‘Other background’ sample, even though it is created from a separate simulation.

Table 2.1: Overview of the simulation samples and analysis weight used for the different signal and background components.

Signal type	Sample	Weight
Signal	Enhanced $\nu$ -on-e	Flux & $\nu$ Mag. Moment
$\nu$ -on-e background	Enhanced $\nu$ -on-e	Flux & Rad. Corr.
$\nu_e$ CC MEC background	Enhanced $\nu_e$ CC MEC	Flux & Cross Sec.
Other background	Nominal ND	Flux & Cross Sec.

## 2.3 Event selection

We are searching for  $\nu$ -on-e elastic scattering events, characterised by a single very forward going electron shower, specifically focusing on low electron recoil energies. The main background for our analysis come from  $\nu_e$ CC interactions, which produce an electron with an additional activity, and interactions that produce  $\pi^0$ , which decays into two photons producing electromagnetic showers, where each can look similar to the  $\nu$ -on-e signal. Additionally, there are  $\nu_\mu$ CC interactions, which are generally easy to distinguish from our signal, however, their very high abundance in the NOvA ND makes them a dominant background nevertheless.

We explain the motivation behind each cut of the event selection and discuss their effect on the neutrino magnetic moment events below. We also consider possible improvements to the event selection for a future (re-)analysis.

The strategy for event selection is as follows. First, we remove events that failed reconstruction or data collection, described in Sec. 2.3.1 and 2.3.2. Then, we apply pre-selection cuts that remove obvious background (Sec. 2.3.3), while limiting the reduction of the signal efficiency to about 0.25 %. Following this, we apply the containment cuts (Sec. 2.3.4) that remove events that are either not fully contained within the detector, or events that originate from outside of the detector, such as rock muons. Afterwards, we perform a cut-based Multi Variate Analysis (MVA) on a selection of variables useful for distinguishing the signal from the background, discussed in Sec. 2.3.5, and evaluate their combined performance on the signal selection. We choose the cut

values that result in the best statistical significance, based on a chosen Figure Of Merit (FOM). Given that we are searching for a very limited number of signal events on top of a large background, we chose a simple statistics-only FOM

$$\text{FOM} = \frac{\text{Signal}}{\sqrt{\text{Background}}}. \quad (2.39)$$

The summary of the cut values for the event selection of neutrino magnetic moment signal is presented in Tab. 2.2, showing the label for the event selection variable, its description and the cut value chosen. After the full event selection, the predicted number of signal events for  $\mu_\nu = 10^{-9} \mu_B$  is 56.80 and the total number of background events under the SM hypothesis is 700.33.

### 2.3.1 Data Collection Quality

To ensure good data quality, we apply the following criteria to data (not applied to simulation) [107]. A cut on the time of each spill relative to other spills and on the exposure of each spill, where every spill is required to have at least  $2^{12}$  POT. Additionally, the current in the focusing horn is required to be within  $-202 \text{ kA} < I_{Horn} < -196.4 \text{ kA}$ , the position of the beam to be within  $\pm 2 \text{ cm}$  in both x and y axis, and that the width of the beam to be within 0.57 and 1.58 cm. Furthermore, incomplete events, or events with issues in one or more DCMs are removed as well.

### 2.3.2 Reconstruction Quality

As described in Sec. 1.5, electrons are reconstructed by slicing, then vertexing, then clustering into prongs. To identify electrons we require a valid reconstructed vertex and at least one reconstructed prong. Even though electrons only consist of a single shower, we don't reject events with more than one prong in a slice, as the reconstruction can wrongly assign noise hits as a separate prong. These false secondary prongs can be removed later in the event selection.

Figure 2.6 and Tab. 2.3 show that about 68 % of signal events do not have a valid reconstructed vertex. This is due to the concentration of signal events at very low electron recoil energies, which results in events that can consist of a small number of hits, or even a single hit. As can be seen in the bottom plot in Fig. 2.6, events

with small true electron recoil energies have much smaller vertex reconstruction efficiency than the higher energetic electrons. However, ongoing work is improving the vertex reconstruction in the [NOvA](#) detectors with a use of [ML](#) instead of the currently used Hough transform combined with Elastic Arms [108]. Improving [NOvA](#) vertex reconstruction at low energies can enhance our event selection in the future.

Additionally, we limit the number of hits per plane to  $< 6$ . This is to remove the

Table 2.2: Summary of the variables and their cut values for the event selection of neutrino magnetic moment signal. Showing the category of the event selection variable, its label, description and the cut value chosen.

	<b>Label</b>	<b>Description</b>	<b>Cut</b>
<b>Reco Qual.</b>	<b>Valid Vtx</b>	Valid reconstructed vertex	$> 0$
	<b>Nº Prongs</b>	Number of reconstructed prongs	$> 0$
	<b>Hits / Plane</b>	Number of hits per plane	$< 6$
	<b>Low <math>E_{Shower}</math></b>	Low cut on calorimetric energy of the most energetic shower	$> 0.5 \text{ GeV}$
<b>Pre-selection</b>	<b>Nº Hits Loose</b>	Preliminary cut on the total number of hits for all prongs in a slice	$< 280$
	<b>Prong Length</b>	Length of the longest prong	$< 640 \text{ cm}$
	<b><math>E\theta^2</math> Loose</b>	Preliminary cut on the product of the calorimetric energy and angle squared of the leading shower	$< 0.064 \text{ GeV} \times \text{rad}^2$
<b>Fiducial</b>	<b>Vertex</b>	x position	$> -177 \text{ cm}$
		y position	$< 177 \text{ cm}$
		z position	$> -177 \text{ cm}$ $< 177 \text{ cm}$ $> 50 \text{ cm}$ $< 1170 \text{ cm}$
	<b>Containment</b>	Minimum hit position in x Maximum hit position in x Minimum hit position in y Maximum hit position in y Minimum hit position in z Maximum hit position in z	$> -177 \text{ cm}$ $< 177 \text{ cm}$ $> -185 \text{ cm}$ $< 177 \text{ cm}$ $> 55 \text{ cm}$ $< 1270 \text{ cm}$
<b>Selection</b>	<b><math>E_{Shower}/E_{Tot}</math></b>	Fraction of energy contained in the most energetic shower	$> 0.91$
	<b>Nº Hits</b>	Total number of hits for all prongs in a slice	$< 116$
	<b>High <math>E_{Shower}</math></b>	Calorimetric energy of the most energetic shower	$< 1.4 \text{ GeV}$
	<b><math>\nu\text{-on-e ID}</math></b>	<a href="#">CVN</a> -based $\nu\text{-on-e}$ identifier	$> 0.65$
	<b><math>E\pi^0</math> ID</b>	<a href="#">CVN</a> -based $\nu\text{-on-e}$ and $\pi^0$ identifier	$> 0.63$
	<b><math>E\theta^2</math></b>	Product of the calorimetric energy and angle squared of the leading shower	$< 0.0048 \text{ GeV} \times \text{rad}^2$

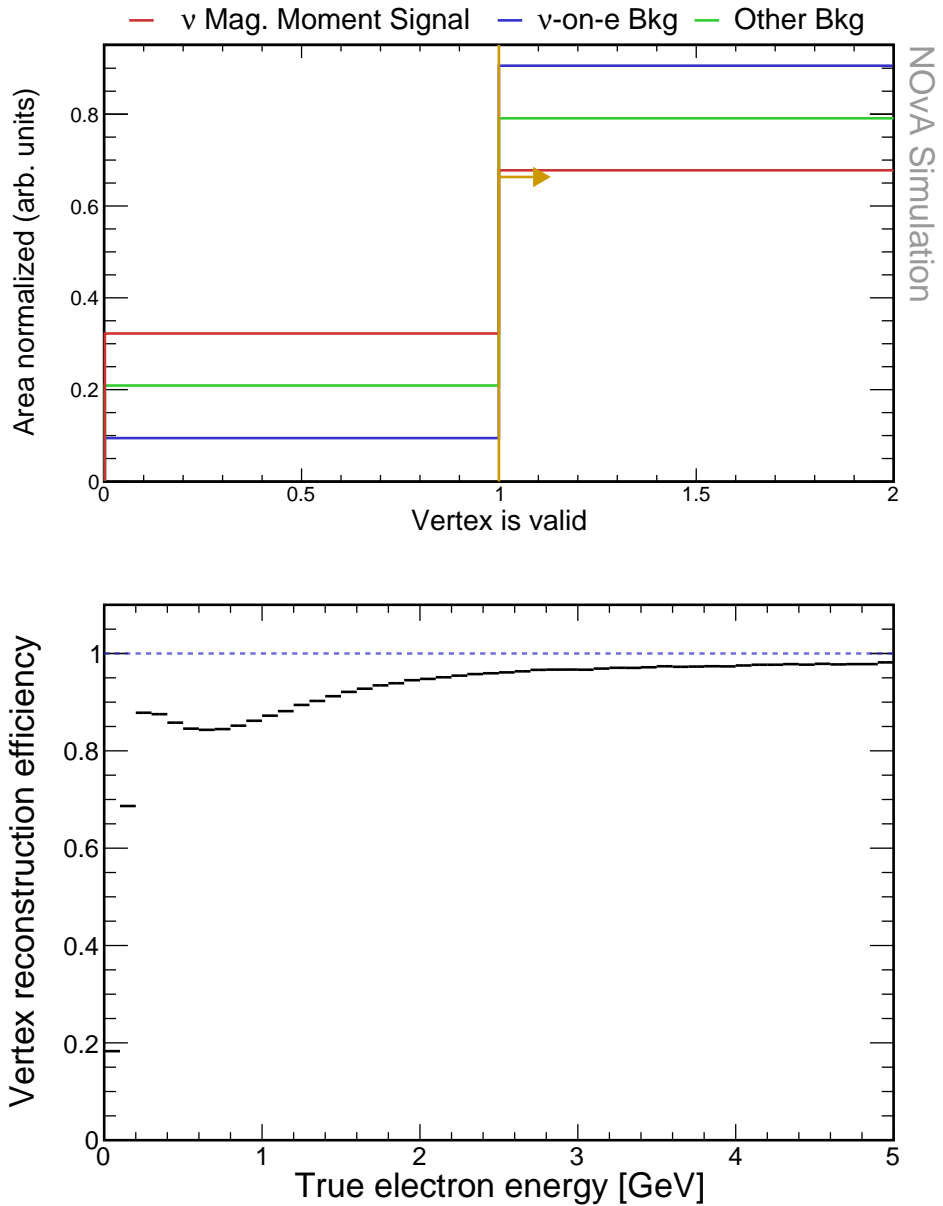


Figure 2.6: Top: Relative comparison of the signal (red),  $\nu$ -on-e background (blue), and other background (green) events for the vertex reconstruction quality selection. Each histogram is area-normalised and the first bin corresponds to events without a valid vertex and second bin to events with correctly reconstructed vertex. The yellow line indicates the chosen cut value, where all events have to have a valid reconstructed vertex. Bottom: profile histogram of the ‘vertex is valid’ variable as a function of the true electron energy for the true signal events, showing the significant drop in vertex reconstruction efficiency at low electron recoil energies. No selection was applied prior to making these plots.

so-called ‘FEB flashers’, which are caused by such a high energy deposit in one cell, that it affects all the other channels on the same **APD** [109]. The cut value was chosen so that it removes approximately 0.25 % signal events, which is the same criterion as is used for the pre-selection cuts described below. Relative comparisons between signal and background for the number of prongs and the number of hits per plane are shown in Fig. 2.7.

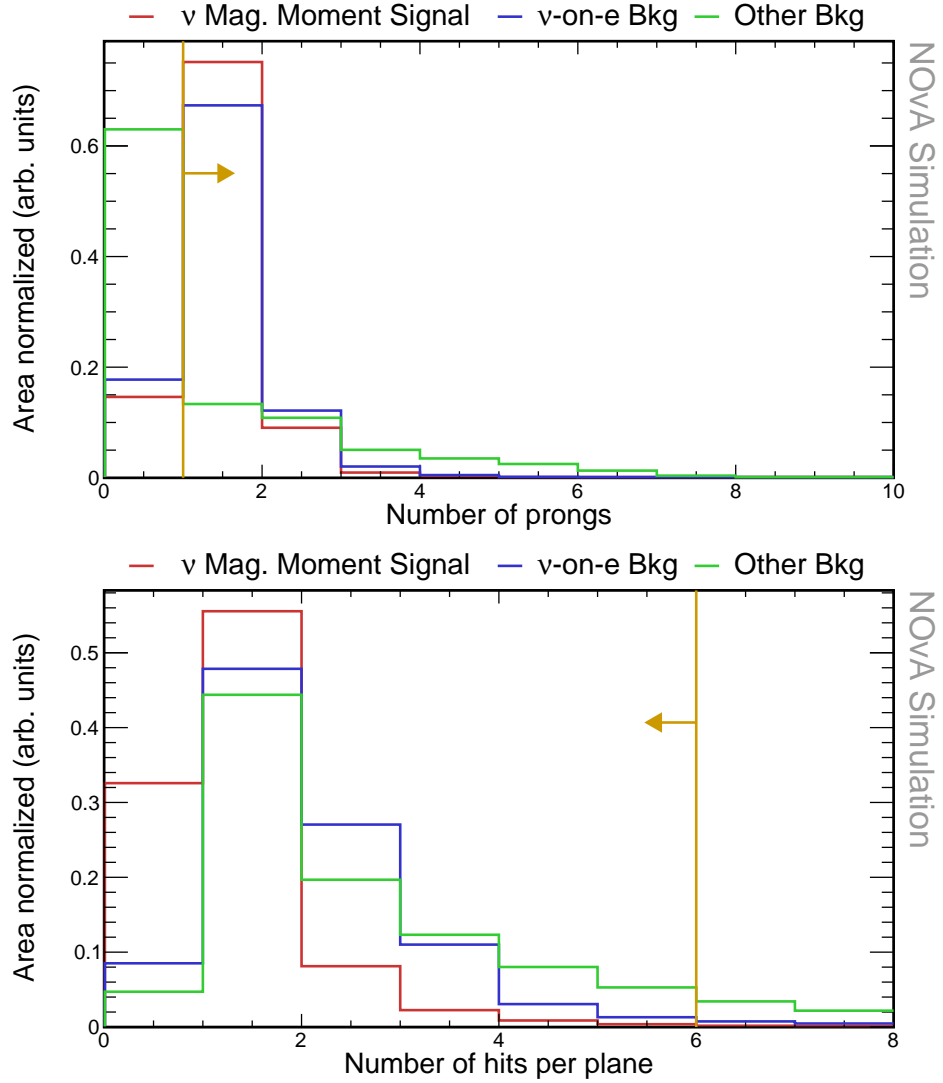


Figure 2.7: Relative comparison of signal (red),  $\nu$ -on-e background (blue), and other background (green) events in the number of prongs (top) and the number of hits per plane (bottom) distributions. Events in both plots are required to have a valid reconstructed vertex and in the bottom plot also at least one reconstructed prong. Yellow lines indicate the cut values for the shown variables, with arrows pointing towards the preserved events. All histograms are area-normalised.

Furthermore, the reconstructed calorimetric energy of the primary shower is required to be  $E_{cal} > 0.5 \text{ GeV}$  as shown in Fig. 2.8. This is due to the limitations of

the currently used **CVN**-based  $\nu$ -on-e identifiers described in Sec. 2.3.5, which were developed and validated for  $\nu$ -on-e events with energies above this limit, to avoid the large background at low energies. However, due to the nature of the neutrino magnetic moment signal, which is concentrated at low electron recoil energies, this cut also removes a majority of our signal events, specifically 66.8 %. This large reduction severely impacts the significance of our measurement. On the other hand, it also marks potentially the most impactful improvement available in a future re-analysis. There are other event identifying algorithms available in **NOvA** that could be explored for  $\nu$ -on-e events to leverage the low energy sample. Additionally, it is possible to develop a purpose-built  $\nu$ -on-e identifier focusing on low electron recoil energies.  
COMMENT: Can you please read this paragraph and tell me what you think about it?

Table 2.3: Event selection cutflow table for the reconstruction quality cuts showing the number of events and the relative efficiency of each cut for each signal sample. The relative efficiency is calculated as number of events remaining after applying the corresponding cut divided by number of event for all the previous cuts. All the cuts are listed in sequence as they are applied.

<b>Selection</b>	<b>Signal</b>		<b><math>\nu</math>-on-e bkg</b>		<b>Other bkg</b>	
	$N_{evt}$	$\epsilon_{rel}$ (%)	$N_{evt}$	$\epsilon_{rel}$ (%)	$N_{evt}$	$\epsilon_{rel}$ (%)
<b>No Cut</b>	817.34	100	$6.82 \times 10^3$	100	$2.96 \times 10^8$	100
<b>Valid Vtx</b>	553.86	67.76	$6.17 \times 10^3$	90.55	$2.34 \times 10^8$	79.10
<b>Nº Prongs</b>	472.90	85.38	$5.08 \times 10^3$	82.25	$8.66 \times 10^7$	37.00
<b>Hits / Plane</b>	471.14	99.63	$4.97 \times 10^3$	97.85	$7.32 \times 10^7$	89.56
<b>Low <math>E_{Shower}</math></b>	156.37	33.19	$3.53 \times 10^3$	71.09	$4.06 \times 10^7$	55.12

### 2.3.3 Pre-Selection

Pre-selection aims to remove obvious background events without significantly affecting the signal. The criterion we chose for the selection of these cuts is determined by the reduction of the signal efficiency by approximately 0.25 % with each cut. This results in the total pre-selection reduction of the signal efficiency by approximately 1 %.

The first two variables used for our pre-selection are the same as were used in the event selection for the  $\nu_e$  appearance **ND** constraint for the three flavour neutrino oscillation measurements [7]. As we are searching for single electron showers, we

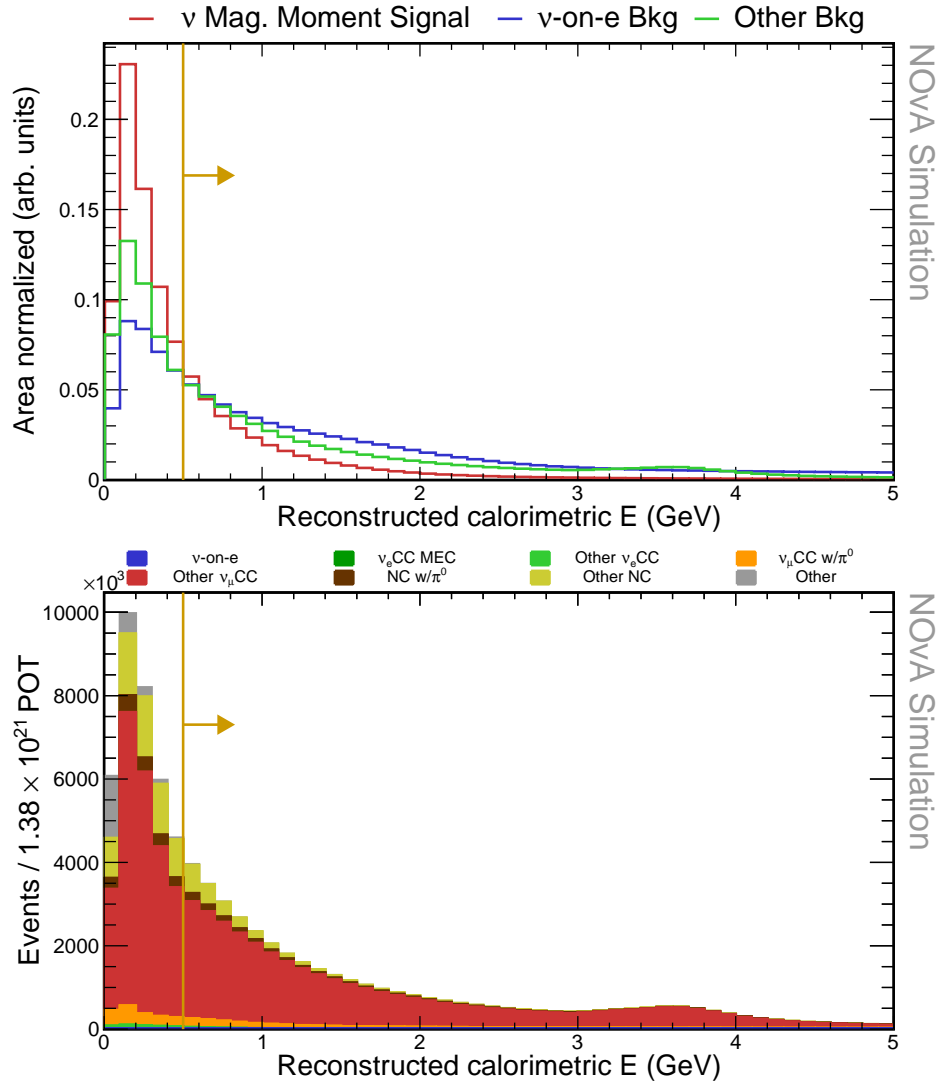


Figure 2.8: Top: Relative comparison of signal (red),  $\nu$ -on-e background (blue), and other background (green) events in the reconstructed calorimetric energy distribution. All histograms are area-normalised. Bottom: Decomposition of background into various sub-samples, normalised to the data POT exposure. Events in both plots are required to have a valid reconstructed vertex, at least one reconstructed prong and less than 6 hits per plane. Yellow lines indicate the cut value for the reconstructed calorimetric energy, with arrows pointing towards the preserved events.

can reduce backgrounds with multiple final state particles by limiting the total activity in the detector. Specifically, we require that the total number of hits assigned to all the reconstructed prongs is  $< 280$ . This is shown in Fig. 2.9. In general, the main background in NOvA consists of the  $\nu_\mu$ CC interactions, which are characterised by long muon tracks. We therefore limit the length of the longest reconstructed prong to be  $< 640$  cm, as shown in Fig. 2.10.

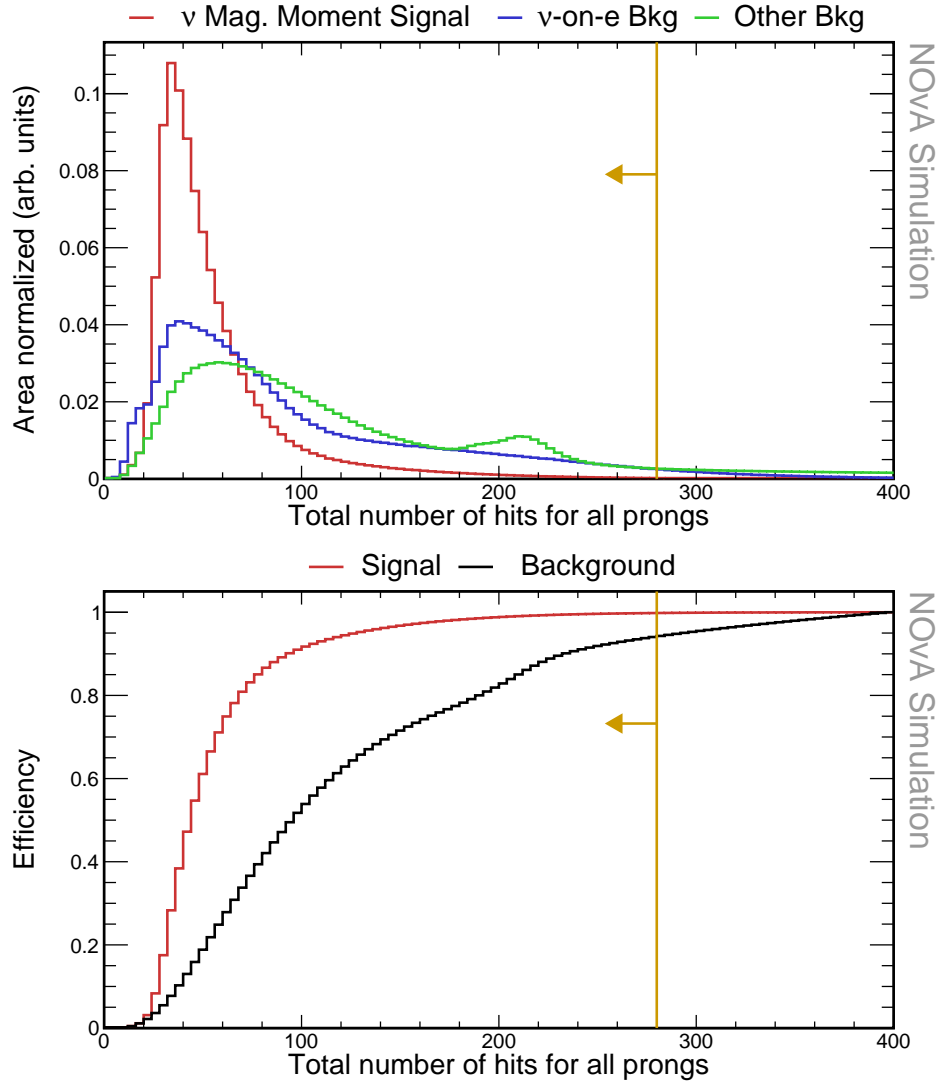


Figure 2.9: Top: Relative comparison of signal (red),  $\nu$ -on-e background (blue), and other background (green) events in the distribution of total number of hits from all reconstructed prongs in the slice. All histograms are area-normalised. Bottom: Cumulative signal (red) and background (black) efficiency calculated as number of signal/background events left of the bin divided by the total number of signal/background events. Yellow lines indicate the cut value for the maximum number of hits, with arrows pointing towards the preserved events. The reconstruction quality cuts were applied before making these plots.

Additionally, as discussed in Sec. 2.1.2, simple  $2 \rightarrow 2$  kinematics dictate that

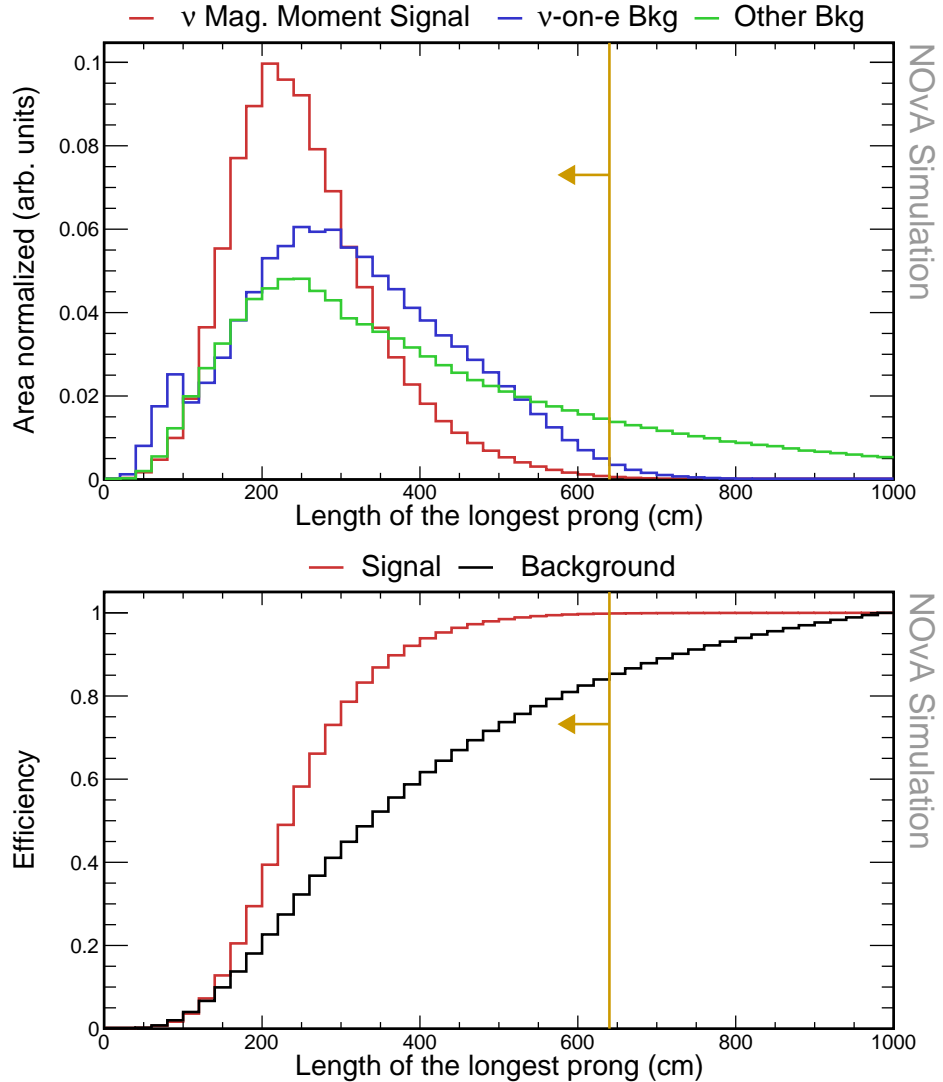


Figure 2.10: Top: Relative comparison of signal (red),  $\nu$ -on-e background (blue), and other background (green) events in the distribution of the length of the longest reconstructed prong in slice. All histograms are area-normalised. Bottom: Cumulative signal (red) and background (black) efficiency calculated as number of signal/background events left of the bin divided by the total number of signal/background events. Yellow lines indicate the cut value for the maximum length of the longest prong, with arrows pointing towards the preserved events. The reconstruction quality cuts and the number of hits cut were applied before making these plots.

the true electron recoil energy and angle for the  $\nu$ -on-e interaction are limited by  $E\theta^2 < 2m_e$ . This can be used to distinguish the  $\nu$ -on-e elastic scattering from  $\nu_e$ CC interactions, which also have an electron in the final state. However, due to unavoidable reconstruction deficiencies, the reconstructed  $E\theta^2$  does not have such a strict cut-off value, and we are placing the pre-selection cut at  $E\theta^2 < 0.064$ , as can be seen in Fig. 2.11. Furthermore, some of the signal events can be reconstructed with the opposite direction with respect to the beam, which would result in  $\theta \approx \pi$  rad. However, this reconstruction failure likely does not impact other reconstructed qualities and these events should be preserved for the final sample. For that reason, we are calculating the angle between the outgoing electron and the neutrino beam direction as  $\text{acos}(\text{abs}(\cos \theta))$ , which gives the same value whether the shower is reconstructed forward or backwards.

The effect of the pre-selection cuts on the signal and background samples are summarised in Tab. 2.4, where the first row lists the number of events after applying all the reconstruction quality cuts from Sec. 2.3.2. All three of the variables used for the pre-selection are employed again in the MVA, as described in Sec. 2.3.5.

Table 2.4: Pre-selection cutflow table showing the number of events and the relative efficiency of each cut for each signal sample. The relative efficiency is calculated as number of events remaining after applying the corresponding cut divided by number of event for all the previous cuts. All the cuts are listed in sequence as they are applied. The top row corresponds to the sample after applying the reconstruction quality cuts.

<b>Selection</b>	<b>Signal</b>		<b><math>\nu</math>-on-e bkg</b>		<b>Other bkg</b>	
	$N_{\text{evt}}$	$\epsilon_{\text{rel}} (\%)$	$N_{\text{evt}}$	$\epsilon_{\text{rel}} (\%)$	$N_{\text{evt}}$	$\epsilon_{\text{rel}} (\%)$
<b>Reco Quality</b>	156.37	100	$3.53 \times 10^3$	100	$4.28 \times 10^7$	100
<b>No Hits Loose</b>	156.05	99.79	$3.41 \times 10^3$	96.46	$3.61 \times 10^7$	84.35
<b>Prong Length</b>	155.7	99.78	$3.37 \times 10^3$	98.85	$2.61 \times 10^7$	72.36
<b><math>E\theta^2</math> Loose</b>	155.14	99.64	$3.33 \times 10^3$	98.83	$8.83 \times 10^6$	33.82

### 2.3.4 Fiducial and containment cuts

To ensure all the deposited energy of the recoil electron is contained within the detector and to remove events originating outside of the detector (such as rock muons for the ND), we constrain the position of the reconstructed vertex and all the prongs in the slice. Decision on where to place the exact cut values is made based on the maximum FOM value.

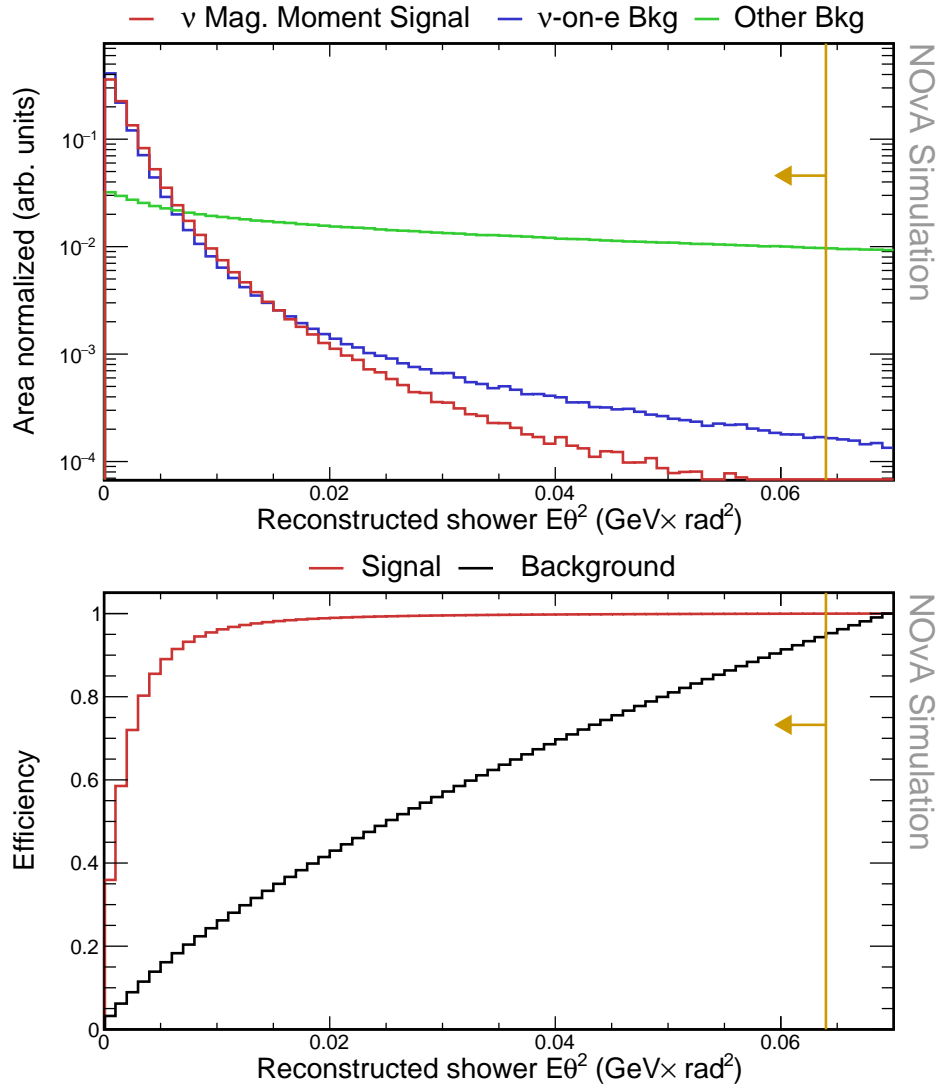


Figure 2.11: Top: Relative comparison of signal (red),  $\nu$ -on-e background (blue), and other background (green) events in the distribution of the reconstructed energy of the leading shower multiplied by its angle from the incoming neutrino beam direction squared. All histograms are area-normalised with logarithmic y axis. Bottom: Cumulative signal (red) and background (black) efficiency calculated as number of signal/background events left of the bin divided by the total number of signal/background events. Yellow lines indicate the cut value for the depicted variable, with arrows pointing towards the preserved events. The reconstruction quality cuts, the number of hits cut, and the length of the longest prong cuts were applied before making both of these plots.

The reconstructed vertex is required to be within the fiducial volume, which represents a well-understood and trusted volume of the detector. To select the fiducial volume, we investigate distributions of the reconstructed vertex in the x, y and z direction, shown in Fig. 2.12, 2.13 and 2.14 respectively. Basic reconstruction quality and pre-selection cuts are applied to make these distributions. Additionally, for the x and y position distributions, we require that the vertex is not placed inside of the Muon Catcher by requiring  $Vtx_Z < 1270$  cm, as it can significantly affect these distributions. The slanted distributions in x and y are caused by the off-axis nature of the NuMI beam and the periodic peaks are due to a combination of the detector structure and the choice of binning.

The reconstructed vertex is required to be contained within the following volume:

$$-175 \text{ cm} < Vtx_X < 175 \text{ cm}, \quad (2.40)$$

$$-175 \text{ cm} < Vtx_Y < 175 \text{ cm}, \quad (2.41)$$

$$95 \text{ cm} < Vtx_Z < 1170 \text{ cm}. \quad (2.42)$$

Furthermore, we constrain the extreme positions (minimum and maximum) of all the hits within the most energetic prong, which is assumed to represent the electron shower for the signal events. We apply the reconstruction quality, pre-selection and fiducial (vertex position) cuts to their distributions, shown in Fig. 2.15-2.20 **COMMENT: Is it enough to reference these figures like this?**. The extreme hit positions are required to be within the following volume:

$$-175 \text{ cm} < \min_X, \max_X < 175 \text{ cm}, \quad (2.43)$$

$$-175 \text{ cm} < \min_Y, \max_Y < 175 \text{ cm}, \quad (2.44)$$

$$105 \text{ cm} < \min_Z, \max_Z < 1270 \text{ cm}. \quad (2.45)$$

### 2.3.5 Multivariate Analysis

Following the removal of obvious backgrounds and events not contained within the detector, we aim to optimise the event selection to achieve the highest significance for measuring the effective muon neutrino magnetic moment. This goal is equivalent

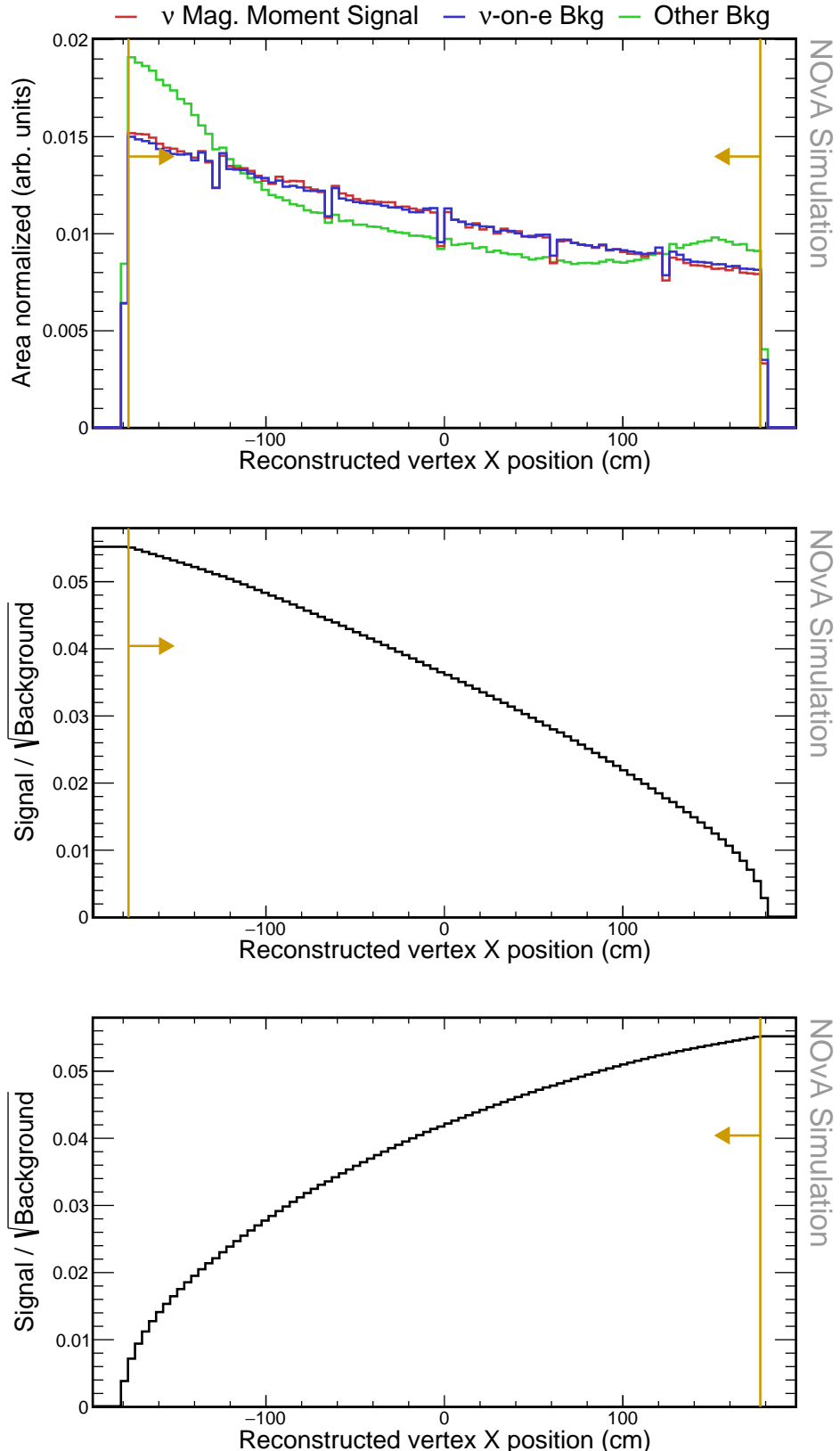


Figure 2.12: Top: Relative comparison of signal (red),  $\nu$ -on-e background (blue), and other background (green) events in the distribution of the x position of the reconstructed vertex. All histograms are area-normalized. Middle and bottom: Cumulative FOM calculated as the number of signal events, divided by the number of background events from that bin until the end of the plot in the direction of the yellow arrow. The reconstruction quality and pre-selection cuts were applied prior to making these plots. Additionally, vertex is required to be within the active region of the detector ( $Vtx_Z < 1270$  cm). Yellow lines show the cut values that create the fiducial volume, with arrows pointing towards the preserved events.

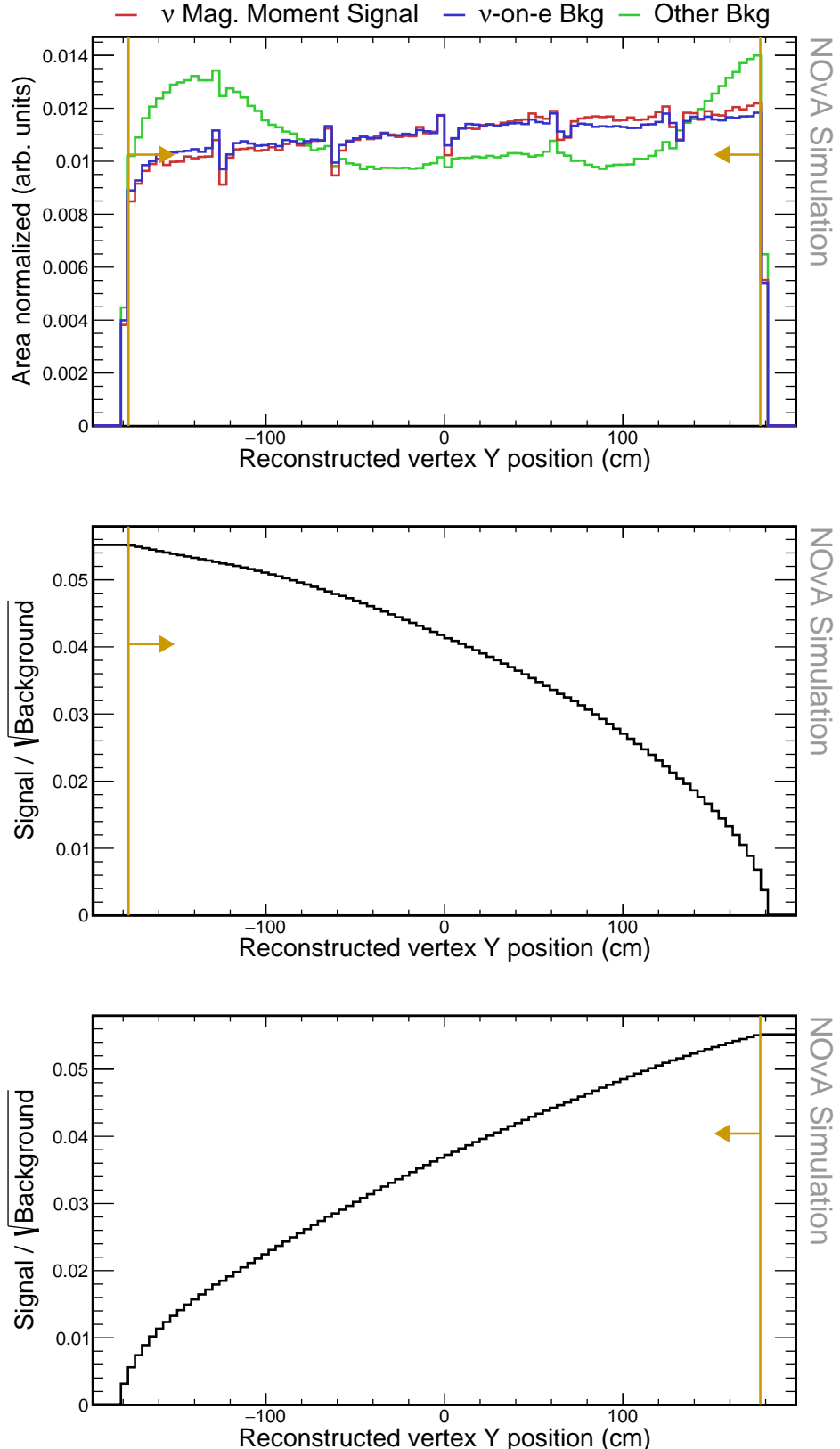


Figure 2.13: Top: Relative comparison of signal (red),  $\nu$ -on-e background (blue), and other background (green) events in the distribution of the y position of the reconstructed vertex. All histograms are area-normalized. Middle and bottom: Cumulative FOM calculated as the number of signal events, divided by the number of background events from that bin until the end of the plot in the direction of the yellow arrow. The reconstruction quality and pre-selection cuts were applied prior to making these plots. Additionally, vertex is required to be within the active region of the detector ( $Vtx_Z < 1270$  cm). Yellow lines show the cut values that create the fiducial volume, with arrows pointing towards the preserved events.

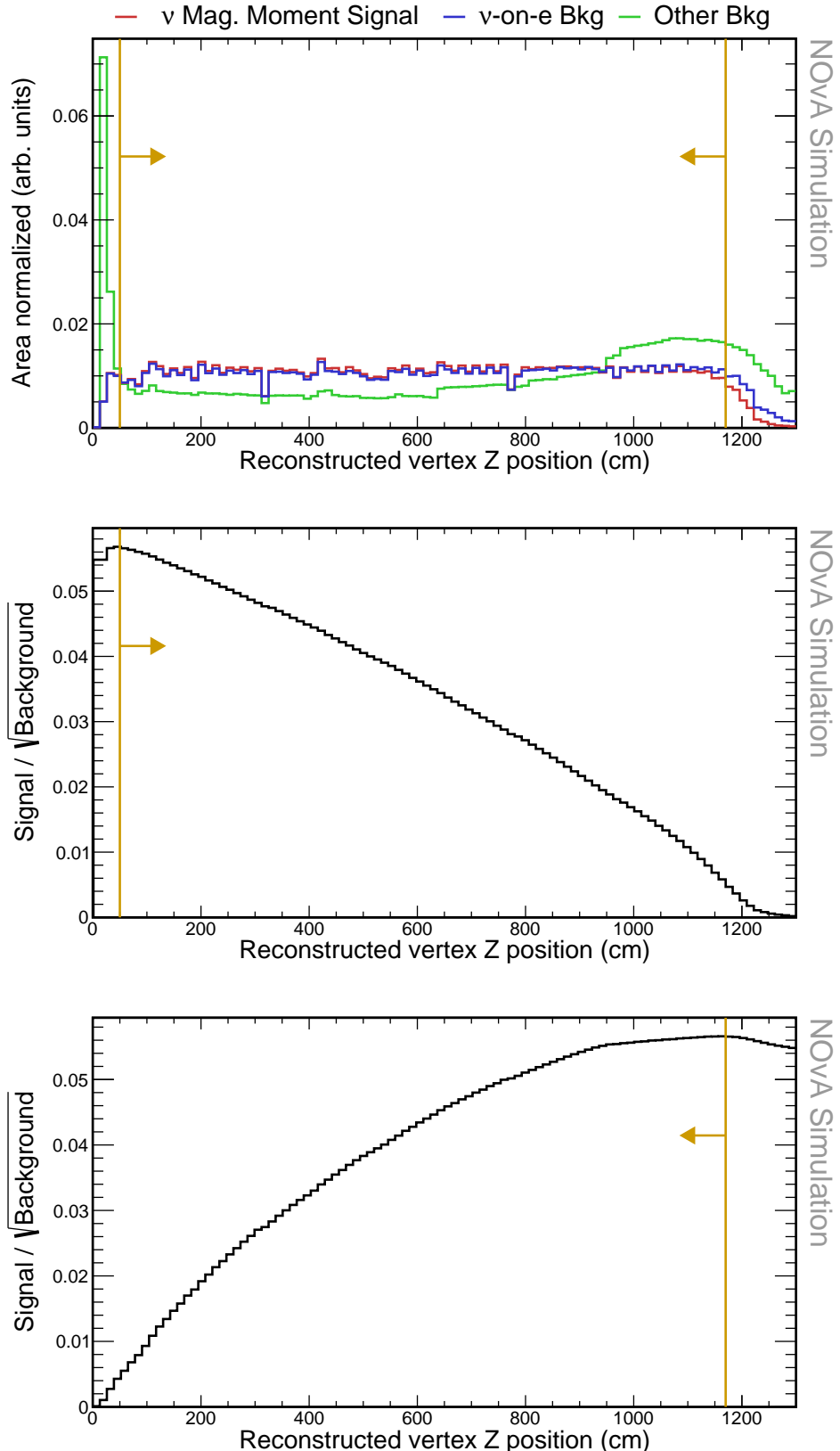


Figure 2.14: Top: Relative comparison of signal (red),  $\nu$ -on-e background (blue), and other background (green) events in the distribution of the z position of the reconstructed vertex. All histograms are area-normalized. Middle and bottom: Cumulative FOM calculated as the number of signal events, divided by the number of background events from that bin until the end of the plot in the direction of the yellow arrow. The reconstruction quality and pre-selection cuts were applied prior to making these plots. Yellow lines show the cut values that create the fiducial volume, with arrows pointing towards the preserved events.

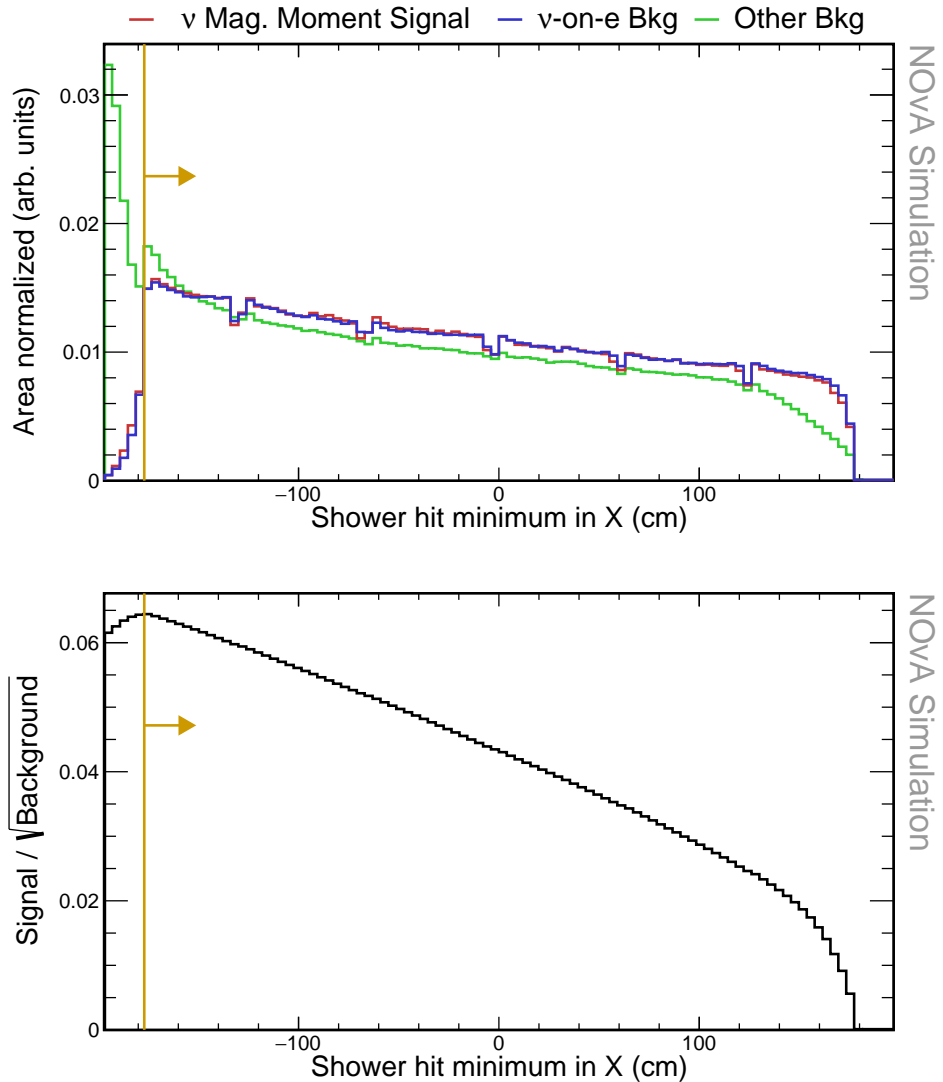


Figure 2.15: Top: Relative comparison of signal (red),  $\nu$ -on-e background (blue), and other background (green) events in the distribution of the minimum hit position of the most energetic prong along the x axis. All histograms are area-normalized. Bottom: Cumulative FOM calculated as the number of signal events, divided by the number of background events from that bin until the end of the plot in the direction of the yellow arrow. The reconstruction quality, pre-selection and fiducial cuts were applied prior to making these plots. Yellow lines show the cut values that create the containment volume, with arrows pointing towards the preserved events.

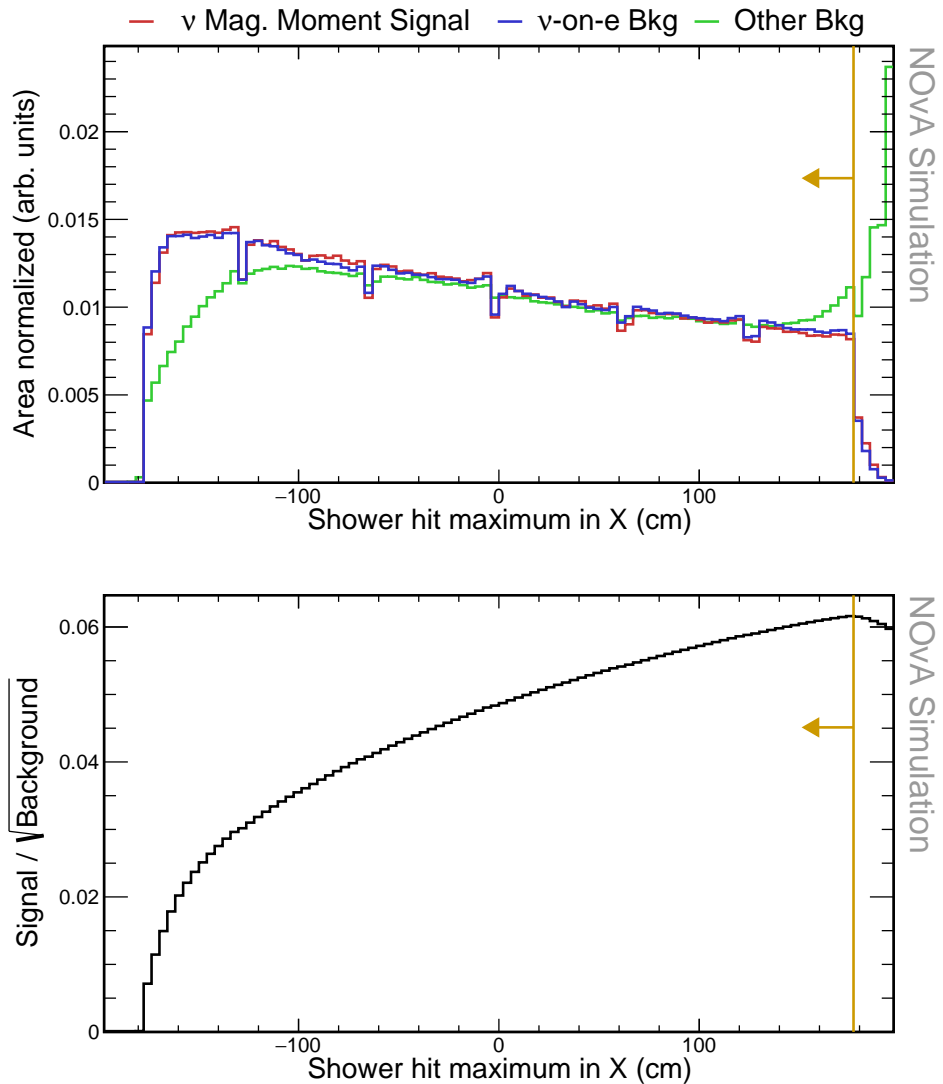


Figure 2.16: Top: Relative comparison of signal (red),  $\nu$ -on-e background (blue), and other background (green) events in the distribution of the maximum hit position of the most energetic prong along the x axis. All histograms are area-normalized. Bottom: Cumulative FOM calculated as the number of signal events, divided by the number of background events from that bin until the end of the plot in the direction of the yellow arrow. The reconstruction quality, pre-selection and fiducial cuts were applied prior to making these plots. Yellow lines show the cut values that create the containment volume, with arrows pointing towards the preserved events.

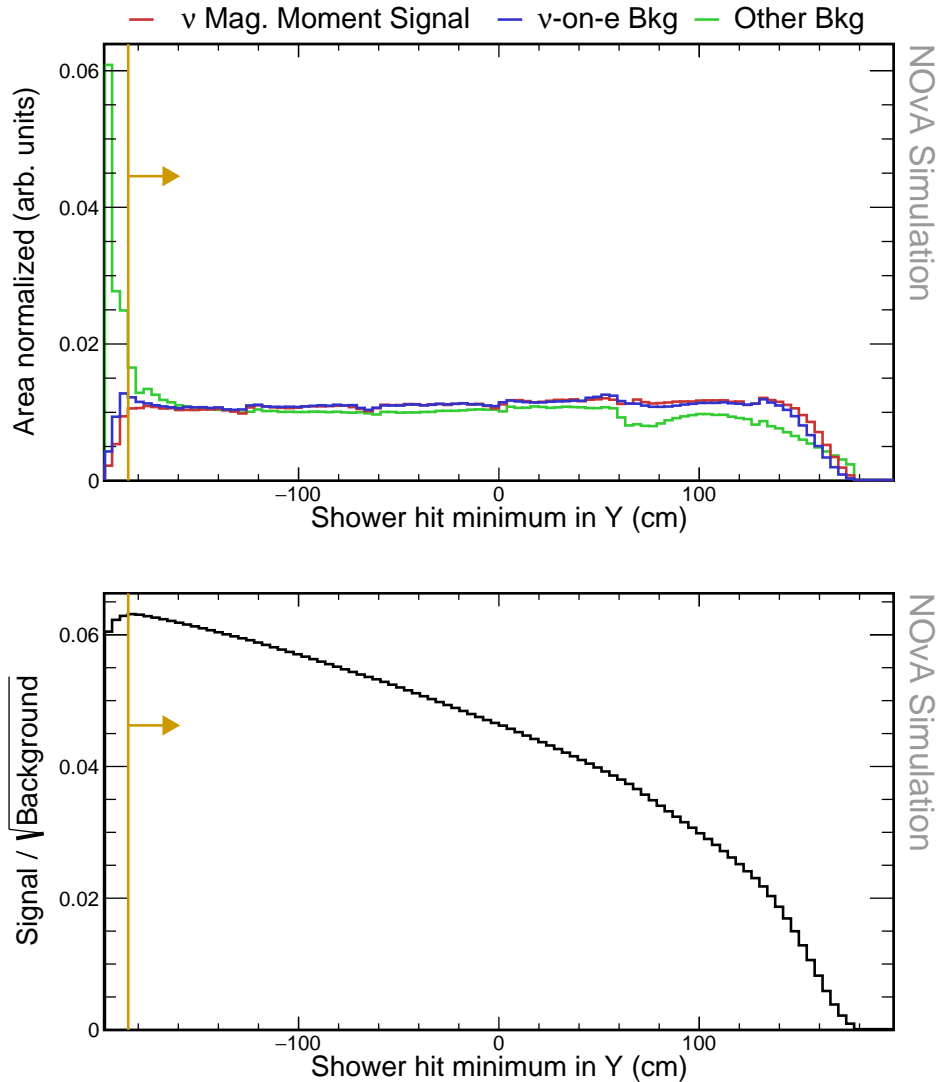


Figure 2.17: Top: Relative comparison of signal (red),  $\nu$ -on-e background (blue), and other background (green) events in the distribution of the minimum hit position of the most energetic prong along the y axis. All histograms are area-normalized. Bottom: Cumulative FOM calculated as the number of signal events, divided by the number of background events from that bin until the end of the plot in the direction of the yellow arrow. The reconstruction quality, pre-selection and fiducial cuts were applied prior to making these plots. Yellow lines show the cut values that create the containment volume, with arrows pointing towards the preserved events.

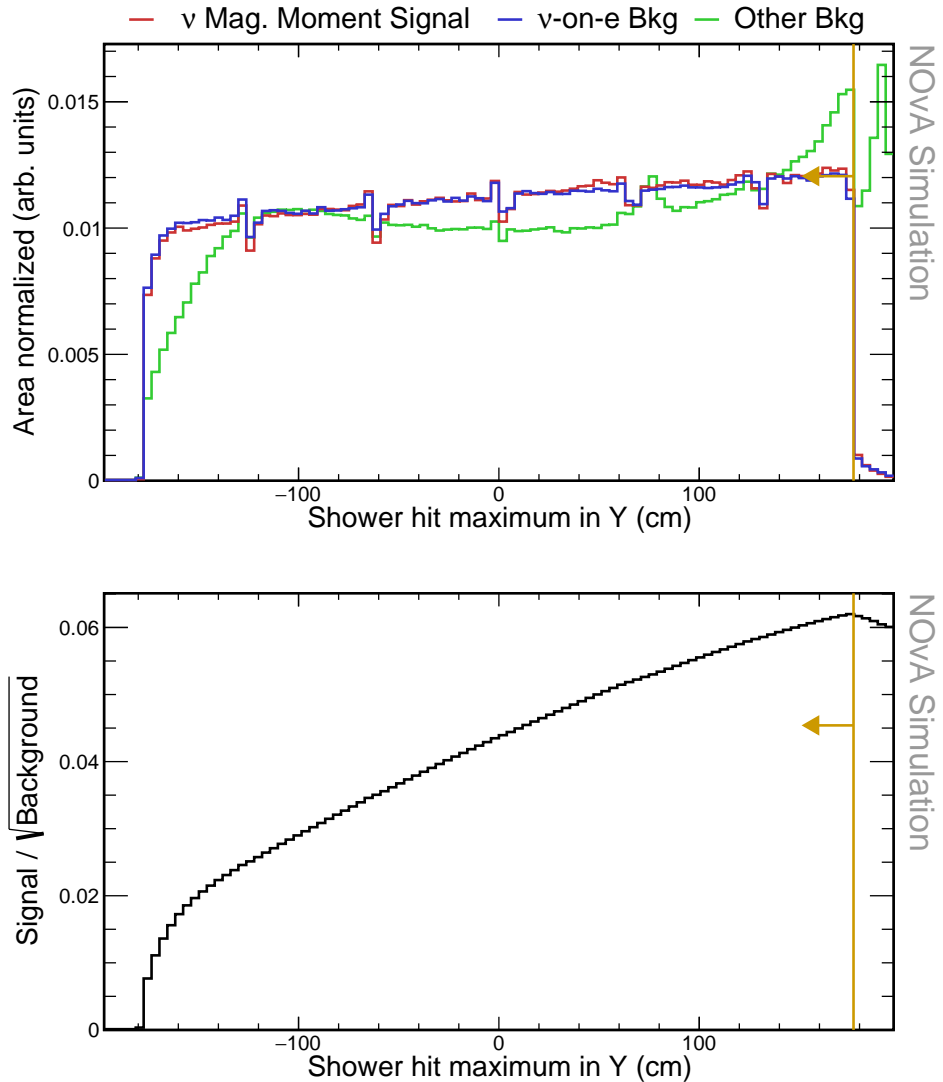


Figure 2.18: Top: Relative comparison of signal (red),  $\nu$ -on-e background (blue), and other background (green) events in the distribution of the maximum hit position of the most energetic prong along the y axis. All histograms are area-normalized. Bottom: Cumulative FOM calculated as the number of signal events, divided by the number of background events from that bin until the end of the plot in the direction of the yellow arrow. The reconstruction quality, pre-selection and fiducial cuts were applied prior to making these plots. Yellow lines show the cut values that create the containment volume, with arrows pointing towards the preserved events.

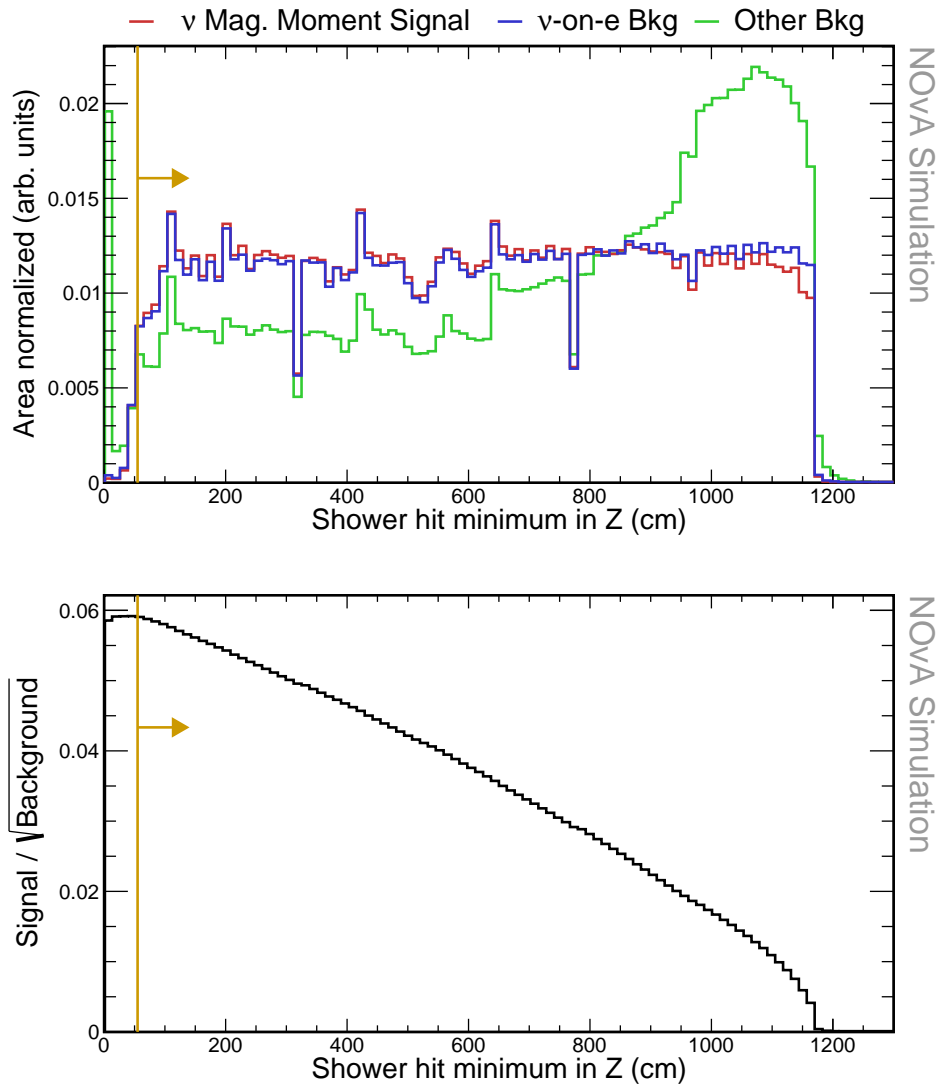


Figure 2.19: Top: Relative comparison of signal (red),  $\nu$ -on-e background (blue), and other background (green) events in the distribution of the minimum hit position of the most energetic prong along the z axis. All histograms are area-normalized. Bottom: Cumulative FOM calculated as the number of signal events, divided by the number of background events from that bin until the end of the plot in the direction of the yellow arrow. The reconstruction quality, pre-selection and fiducial cuts were applied prior to making these plots. Yellow lines show the cut values that create the containment volume, with arrows pointing towards the preserved events.

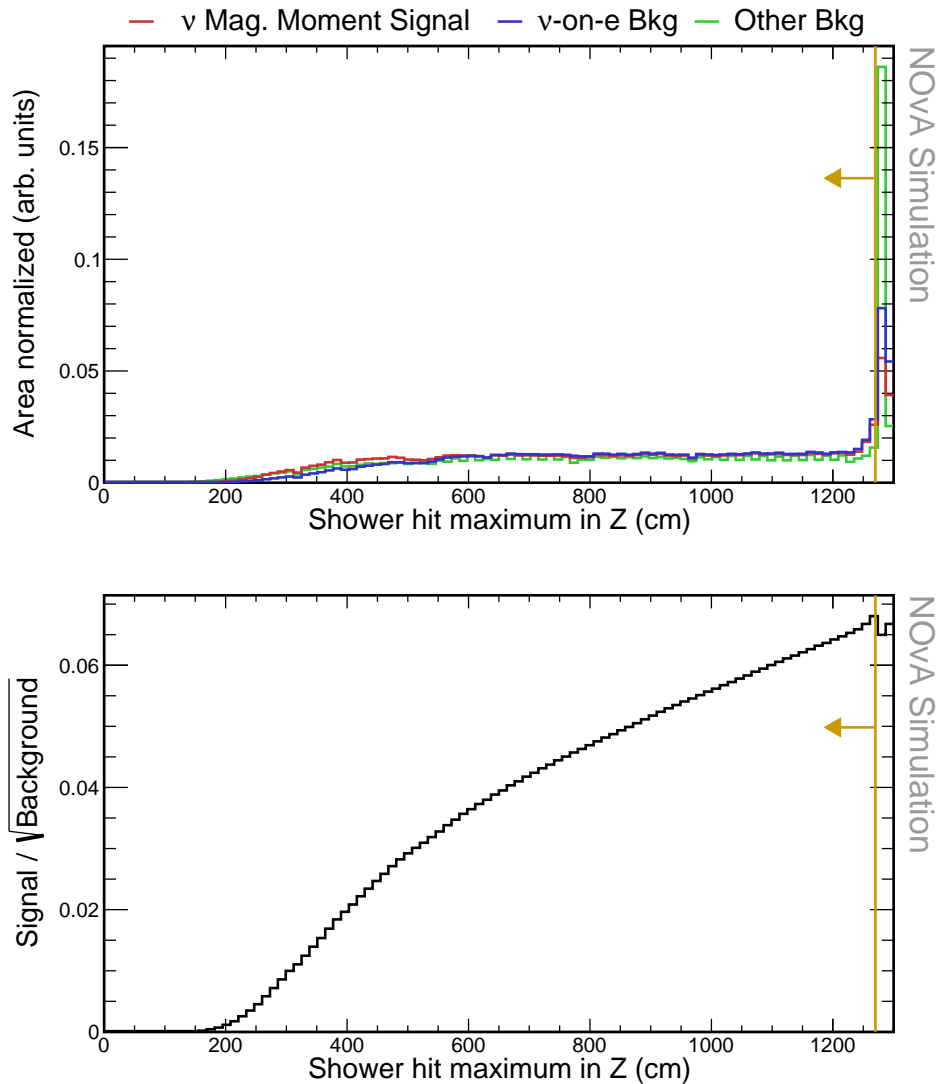


Figure 2.20: Top: Relative comparison of signal (red),  $\nu$ -on-e background (blue), and other background (green) events in the distribution of the maximum hit position of the most energetic prong along the z axis. All histograms are area-normalized. Bottom: Cumulative FOM calculated as the number of signal events, divided by the number of background events from that bin until the end of the plot in the direction of the yellow arrow. The reconstruction quality, pre-selection and fiducial cuts were applied prior to making these plots. Yellow lines show the cut values that create the containment volume, with arrows pointing towards the preserved events.

to maximising our FOM from Eq. 2.39.

For this purpose, we utilise ROOT’s [110] Tool for MVA (TMVA) [111]. Specifically, we employ the rectangular cut optimisation method, which uses multivariate parameter fitters to maximise background rejection across the full range of signal efficiencies. We use the MC sampling fitting method, assuming that for each input variable, there is a single cut value (maximum or minimum) that optimally discriminates between signal and background.

TMVA generally performs better with a limited number of input variables that have strong discriminating power. Therefore, we investigated several input variables and selected only those that achieved significant background rejection. There are additional variables not mentioned here that might achieve better final results, providing opportunities for future re-analyses. Additionally, we do not apply any transformations to the input variables prior to optimisation, which might also improve the final result after dedicated study.

The variables considered include those already used in the pre-selection: the total number of hits for all prongs in slice, the length of the longest prong, and  $E\theta^2$ , as discussed in Sec. 2.3.3. During the TMVA optimisation, we found that the length of the longest prong did not significantly enhance discriminating power and thus removed it from the set of input variables. Additionally, we included the reconstructed energy of the most energetic shower, as used for reconstruction quality selection in Sec. 2.3.2, intending to restrict events with higher energies, since our signal is concentrated at low electron recoil energies.

Additionally, we considered all the variables used for the NOvA  $\nu$ -on-e analysis

Table 2.5: Event selection cutflow table for the containment cuts showing the number of events and the relative efficiency of each cut for each signal sample. The relative efficiency is calculated as number of events remaining after applying the corresponding cut divided by number of event for all the previous cuts. All the cuts are listed in sequence as they are applied. The top row corresponds to the sample after applying the reconstruction quality and pre-selection cuts.

<b>Selection</b>	<b>Signal</b>		<b><math>\nu</math>-on-e bkg</b>		<b>Other bkg</b>	
	$N_{evt}$	$\epsilon_{rel} (\%)$	$N_{evt}$	$\epsilon_{rel} (\%)$	$N_{evt}$	$\epsilon_{rel} (\%)$
<b>Pre-selection</b>	155.14	100	$3.33 \times 10^3$	100	$8.83 \times 10^6$	100
<b>Fiducial</b>	143.02	92.19	$2.88 \times 10^3$	85.60	$5.96 \times 10^6$	67.57
<b>Containment</b>	117.41	82.09	$2.08 \times 10^3$	72.12	$1.10 \times 10^6$	18.38

for the neutrino flux constraint [91]. The first is the fraction of the reconstructed energy of the most energetic shower ( $E_{Shower}$ ) to the total energy of all the reconstructed prongs in the entire slice ( $E_{Tot}$ ). This variable distinguished our signal events, which only have a single shower, from events with multiple showers or additional activity. The second is the gap between the vertex and the most energetic shower, which can distinguish between electron and  $\pi^0$  events, as the latter should have a characteristic gap several cells long. Additionally, we examined the amount of energy contained within  $\pm 8$  planes away from the vertex, besides the energy associated with the most energetic prong, which should distinguish the purely leptonic signal from backgrounds with significant hadronic activity. However, the gap and the vertex energy variables underperformed compared to others and were ultimately not used within the TMVA.

We also utilise two CNN-based event classifiers developed for the NOvA  $\nu$ -on-e analysis for the neutrino flux constraint [91, 92]. These classifiers are specifically designed to identify  $\nu$ -on-e interactions. The first, named  $\nu$ -on-e ID, is trained to select  $\nu$ -on-e events from the primary  $\nu_\mu$ CC background, while the second, named  $E\pi^0$  ID, is trained on events passing the  $\nu$ -on-e ID selection to reject the remaining background with a  $\pi^0$ . These classifiers use a pixel map of the entire slice as input and are designed with the same CNN architecture as ProngCVN and EventCVN described in Sec. 1.5. **COMMENT:** *Do I need to describe these more? - pre-selection cuts and so on? Should I mention here that they were evaluated for events above 0.5GeV, or is it enough that I mentioned it in the beginning?*

The result of the TMVA is a set of cuts on each of the input variables that maximises the FOM. The input variables the cuts that were selected for them are shown in Fig. 2.21, 2.22, and 2.23. The effect of these cuts is summarised in Tab. 2.6. Applying the TMVA cuts reduces the signal by 51.62 %, the  $\nu$ -on-e background by 75.03 % and other background by 99.98 %. The specific values of the cuts resulting from the

TMVA are

$$E_{Shower}/E_{Tot} > 0.91, \quad (2.46)$$

$$\text{Total } N^o \text{ hits for all prongs} < 116, \quad (2.47)$$

$$E_{Shower} < 1.4 \text{ GeV}, \quad (2.48)$$

$$E\theta^2 < 0.0048 \text{ GeV} \times \text{rad}^2, \quad (2.49)$$

$$\nu - on - eID > 0.65, \quad (2.50)$$

$$E\pi^0 ID > 0.63. \quad (2.51)$$

Table 2.6: Event selection cutflow table for the results of the cut-based Multivariate analysis, showing the number of events and the relative efficiency of each cut for each signal sample. The relative efficiency is calculated as number of events remaining after applying the corresponding cut divided by number of event for all the previous cuts. All the cuts are listed in sequence as they are applied. The top row corresponds to the sample after applying the reconstruction quality, pre-selection, fiducial and containment cuts.

<b>Selection</b>	<b>Signal</b>		<b><math>\nu</math>-on-e bkg</b>		<b>Other bkg</b>	
	$N_{evt}$	$\epsilon_{rel} (\%)$	$N_{evt}$	$\epsilon_{rel} (\%)$	$N_{evt}$	$\epsilon_{rel} (\%)$
<b>Contained</b>	117.41	100	$2.08 \times 10^3$	100	$1.10 \times 10^6$	100
$E_{Shower}/E_{Tot}$	113.03	96.28	$2.02 \times 10^3$	97.32	$4.53 \times 10^5$	41.30
<b>N<sup>o</sup> Hits</b>	106.48	94.20	$1.45 \times 10^3$	71.53	$4.02 \times 10^5$	88.78
<b>High <math>E_{Shower}</math></b>	85.51	80.31	777.91	53.76	$3.01 \times 10^5$	74.84
<b><math>\nu</math>-on-e ID</b>	72.23	84.47	652.32	83.86	$4.40 \times 10^3$	1.46
<b><math>E\pi^0</math> ID</b>	67.35	93.24	608.19	93.23	$2.83 \times 10^3$	64.34
<b><math>E\theta^2</math></b>	56.80	84.33	519.09	85.35	181.24	6.40

After the full event selection, the predicted number of signal events for  $\mu_\nu = 10^{-9}\mu_B$  is 56.80, and the total number of background events under the SM hypothesis is 700.33. This results in

$$\text{Signal Purity} = \frac{\text{Signal}}{\text{Signal+Background}} = 7.50 \%, \quad (2.52)$$

$$\text{Signal Efficiency} = \frac{\text{Signal}}{\text{Signal}_{\text{No Cut}}} = 6.95 \%. \quad (2.53)$$

Also,

$$\frac{\text{Signal}}{\sqrt{\text{Background}}} = 2.15 \quad (2.54)$$

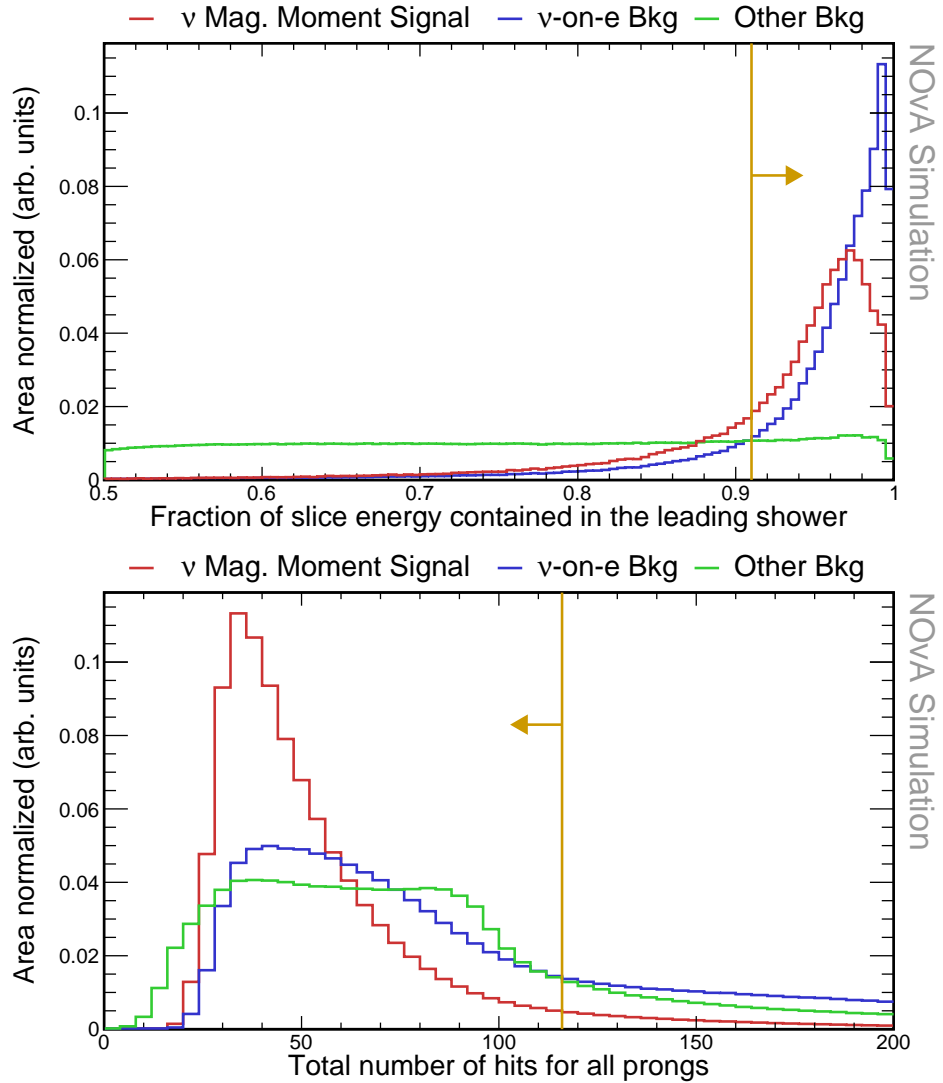


Figure 2.21: Relative comparison of signal (red),  $\nu$ -on-e background (blue), and other background (green) events in the distribution of the fraction of the total energy contained in the primary shower (top) and of the total number of hits in the slice (bottom). All histograms are area-normalized. The reconstruction quality, pre-selection, fiducial and containment cuts were applied prior to making these plots. Yellow lines show the cut values on the depicted variables, with arrows pointing towards the preserved events.

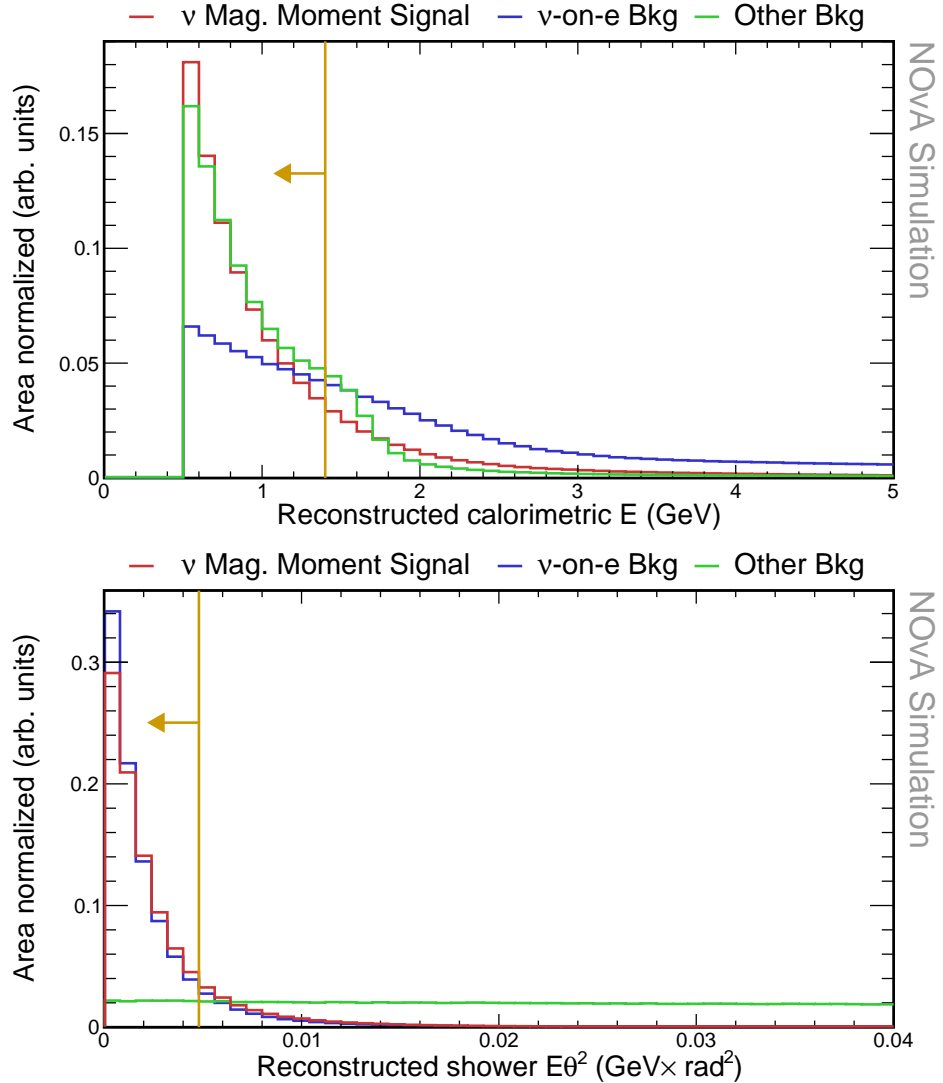


Figure 2.22: Relative comparison of signal (red),  $\nu$ -on-e background (blue), and other background (green) events in the distribution of the reconstructed energy of the primary shower (top) and of the reconstructed energy multiplied by the angle from the incoming neutrino beam direction squared.(bottom). All histograms are area-normalized. The reconstruction quality, pre-selection, fiducial and containment cuts were applied prior to making these plots. Yellow lines show the cut values on the depicted variables, with arrows pointing towards the preserved events.

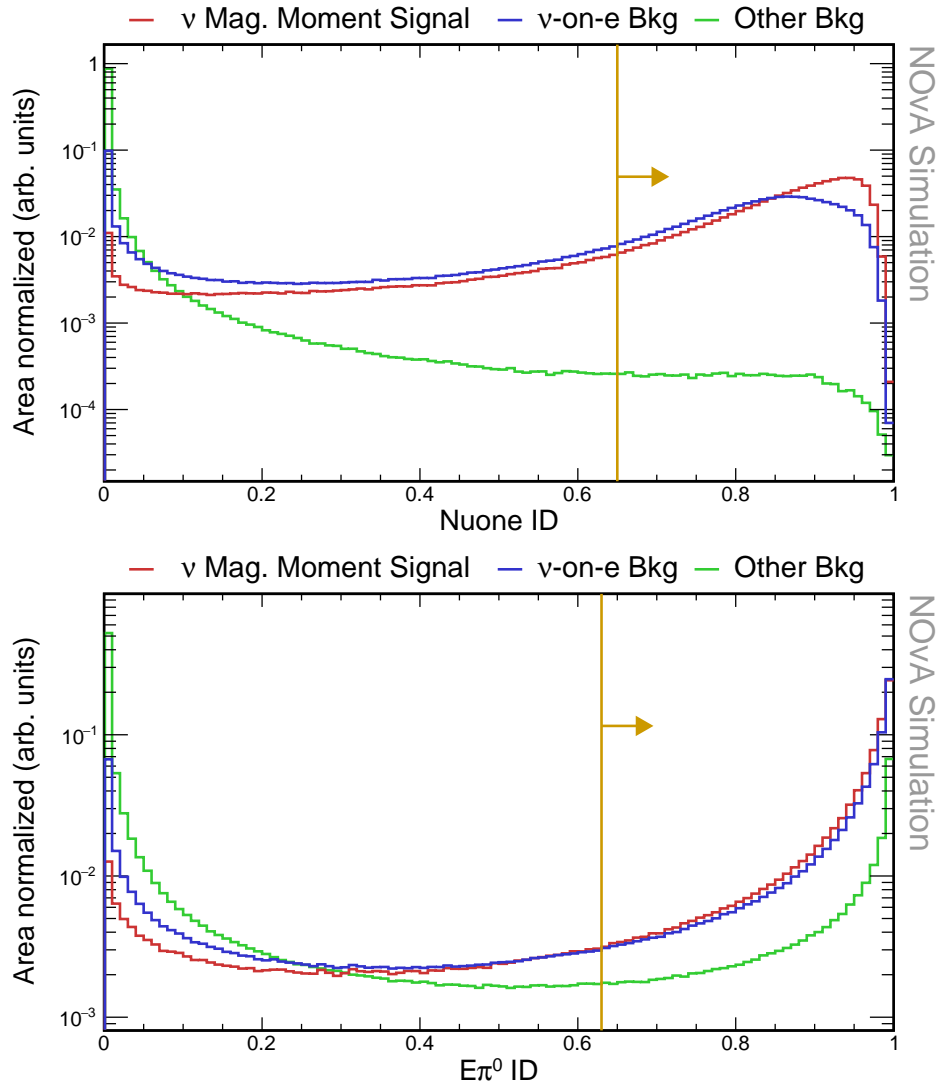


Figure 2.23: Relative comparison of signal (red),  $\nu$ -on-e background (blue), and other background (green) events in the distribution of the NuoneID (top) and EPi0ID (bottom) event identifiers. All histograms are area-normalized and logarithmic in the y axis. The reconstruction quality, pre-selection, fiducial and containment cuts were applied prior to making these plots. Yellow lines show the cut values on the depicted variables, with arrows pointing towards the preserved events.

and

$$\text{FOM} = \frac{\text{Signal}}{\sqrt{\text{Signal+Background}}} = 2.06. \quad (2.55)$$

## 2.4 Systematic uncertainties

### 2.5 Results

Show the money plot - full prediction in the binned energy distribution, including the full statistical and systematic uncertainties

Write out the total number of measured events and their corresponding uncertainties

Explain what are the results of the fit and the limits, discuss the statistical significance of the result

We are basically doing two separate things:

1. Testing a hypothesis that there is no magnetic moment present in the signal.  
Can we reject the null hypothesis given our data?
2. If we can reject the null hypothesis we want to estimate the best fit of the parameter. Additionally, we want to put a limit (set a confidence interval) on the magnetic moment parameter.

What should be included here:

- Fit methodology: Detail the fitting techniques used to extract the muon neutrino magnetic moment from the data.
- Fit validation: Describe how the fit is validated, including any statistical tests used.
- Fake data studies: Explain the use of fake data or Monte Carlo simulations to test the robustness of the analysis.

## 2.6 Discussion

What should be included here:

- Interpretation: Interpret the results in the context of the current understanding of neutrino physics.
- Implications: Explain the broader implications of your findings for the field of particle physics.
- Future work: Suggest directions for future research based on your results.
  - Improvements in NOvA, more FHC data, including RHC data, better reconstruction, better simulation and calibration, better event selection, including sideband samples, more systematics studies, better fitting techniques...
  - Future beyond NOvA - DUNE
    - \* What are the possibilities for DUNE?

## 2.7 Summary

Summarize the results and compare them to the introduction, including comparisons to other experiments and theory. Restate the significant of the measurement

Closing remarks



# Acronyms

**$\nu$ -on-e** neutrino-on-electron. 25, 26, 28, 32–41, 43–51, 53–67

**2p2h** two particle - two hole. 10

**ADC** Analog-to-Digital Converter. 7, 14, 17, 18

**APD** Avalanche Photodiode. 5–7, 10, 17, 18, 45

**ASIC** Application-Specific Integrated Circuit. 7

**BDT** Boosted Decision Tree. 14

**BPF** Break Point Fitter. 12

**BSM** Beyond Standard Model. 25–27, 29, 30

**C.L.** Confidence Level. 25, 26

**CC** Charged Current. 9–11, 34, 40, 41, 48, 50, 63

**CMC** Comprehensive Model Configuration. 10

**CNN** Convolutional Neural Network. 13, 63

**COH $\pi$**  Coherent  $\pi$  (production). 10

**CP** Charge conjugation - Parity (symmetry). 1

**CRY** Cosmic-Ray Shower Generator. 10, 14

**CVN** Convolutional Visual Network. 13, 43, 46

**DAQ** Data Acquisition. 7, 11, 16

**DCM** Data Concentration Module. 7, 8, 42

**DIS** Deep Inelastic Scattering. 10

**DUNE** Deep Underground Neutrino Experiment. 1, 9

**FB** Fibre Brightness. 17, 18

**FD** Far Detector. 3–7, 10, 11, 17–19, 22

**FEB** Front End Board. 6–8, 17, 45

**Fermilab** Fermi National Accelerator Laboratory. 1, 3, 9

**FHC** Forward Horn Current (neutrino mode). 2, 3

**FOM** Figure Of Merit. 42, 50, 53–63, 68

**FPGA** Field Programmable Gate Array. 7

**FSI** Final State Interaction. 10

**LDM** Light Dark Matter. 26

**LOWESS** Locally Weighted Scatter plot Smoothing. 19, 20

**MC** Monte Carlo. 8–10, 14, 38, 62

**MEC** Meson Exchange Current. 10, 40, 41

**MEU** Muon Energy Unit. 21

**MI** Main Injector. 1, 2, 9

**MIP** Minimum Ionising Particle. 14, 18, 21

**MIPP** Main Injector Particle Production (experiment). 9

**ML** Machine Learning. 13, 14, 43

**MVA** Multi Variate Analysis. 41, 50, 62, 73

**NC** Neutral Current. 11, 14

**ND** Near Detector. 1, 3–5, 7, 11, 12, 22, 24–26, 28, 31, 38, 41, 46, 50

**NDOS** Near Detector on the Surface. 3

**NOvA** NuMI Off-axis  $\nu_e$  Appearance (experiment). 1, 3–14, 16–22, 24–26, 28, 31, 33, 35–38, 40, 41, 43, 46, 48, 62, 63

**NP** New Physics. 30

**NuMI** Neutrinos from the Main Injector. 1–3, 8, 9, 11, 52

**PE** Photo Electron. 6, 7, 15, 17–19

**PECorr** Corrected Photo Electrons. 19, 21

**PID** Particle Identification. 13

**PMNS** Pontecorvo-Maki-Nakagawa-Sakata. 29, 30

**POT** Protons On Target. 2, 38, 40, 42, 47

**PPFX** Package to Predict the Flux. 9, 23, 38

**PVC** Polyvinyl chloride. 4–6, 22

**QE** Quasi Elastic (interaction). 9, 10

**ReMId** Reconstructed Muon Identifier. 14

**Res** Resonant baryon production. 9, 10

**RHC** Reverse Horn Current (antineutrino mode). 2, 3

**SM** Standard Model. 25, 27–30, 34–39, 42, 64

**TMVA** Tool for MVA. 62–64

**WLS** Wavelength Shifting (fibre). 5, 6, 10, 14, 16, 18, 21

# Bibliography

- [1] Nova experiments official website. URL <https://novaexperiment.fnal.gov>. Cited February 2024.
- [2] Fermi national accelerator laboratory official website. URL <https://fnal.gov>. Cited February 2024.
- [3] Gary Feldman for the NOvA Collaboration. Physics of the nova experiment. White paper, 2012. URL <https://nova-docdb.fnal.gov/cgi-bin>ShowDocument?docid=7733>. Public NOvA document: NOVA-doc-7733-v1, cited on 05.2020.
- [4] R.B. Patterson. The NOvA Experiment: Status and Outlook. *Nucl. Phys. B Proc. Suppl.*, 235-236:151–157, 2013. doi:[10.1016/j.nuclphysbps.2013.04.005](https://doi.org/10.1016/j.nuclphysbps.2013.04.005).
- [5] P. Adamson et al. First measurement of muon-neutrino disappearance in NOvA. *Phys. Rev. D*, 93(5):051104, 2016. doi:[10.1103/PhysRevD.93.051104](https://doi.org/10.1103/PhysRevD.93.051104).
- [6] M.A. Acero et al. First Measurement of Neutrino Oscillation Parameters using Neutrinos and Antineutrinos by NOvA. *Phys. Rev. Lett.*, 123(15):151803, 2019. doi:[10.1103/PhysRevLett.123.151803](https://doi.org/10.1103/PhysRevLett.123.151803).
- [7] M. A. Acero et al. Improved measurement of neutrino oscillation parameters by the NOvA experiment. *Phys. Rev. D*, 106(3):032004, 2022. doi:[10.1103/PhysRevD.106.032004](https://doi.org/10.1103/PhysRevD.106.032004).
- [8] M. A. Acero et al. Measurement of neutrino-induced neutral-current coherent  $\pi^0$  production in the NOvA near detector. *Phys. Rev. D*, 102(1):012004, 2020. doi:[10.1103/PhysRevD.102.012004](https://doi.org/10.1103/PhysRevD.102.012004).
- [9] M. A. Acero et al. Measurement of the double-differential muon-neutrino charged-current inclusive cross section in the NOvA near detector. *Phys. Rev. D*, 107(5):052011, 2023. doi:[10.1103/PhysRevD.107.052011](https://doi.org/10.1103/PhysRevD.107.052011).
- [10] M. A. Acero et al. Measurement of the  $\nu_e$ –Nucleus Charged-Current Double-Differential Cross Section at  $\langle E_\nu \rangle = 2.4$  GeV using NOvA. *Phys. Rev. Lett.*, 130(5):051802, 2023. doi:[10.1103/PhysRevLett.130.051802](https://doi.org/10.1103/PhysRevLett.130.051802).

- [11] M. A. Acero et al. Measurement of  $\nu_\mu$  charged-current inclusive  $\pi^0$  production in the NOvA near detector. *Phys. Rev. D*, 107(11):112008, 2023. doi:[10.1103/PhysRevD.107.112008](https://doi.org/10.1103/PhysRevD.107.112008).
- [12] P. Adamson et al. Search for active-sterile neutrino mixing using neutral-current interactions in NOvA. *Phys. Rev. D*, 96(7):072006, 2017. doi:[10.1103/PhysRevD.96.072006](https://doi.org/10.1103/PhysRevD.96.072006).
- [13] M. A. Acero et al. Search for Active-Sterile Antineutrino Mixing Using Neutral-Current Interactions with the NOvA Experiment. *Phys. Rev. Lett.*, 127(20):201801, 2021. doi:[10.1103/PhysRevLett.127.201801](https://doi.org/10.1103/PhysRevLett.127.201801).
- [14] M. A. Acero et al. Supernova neutrino detection in NOvA. *JCAP*, 10:014, 2020. doi:[10.1088/1475-7516/2020/10/014](https://doi.org/10.1088/1475-7516/2020/10/014).
- [15] M. A. Acero et al. Extended search for supernovalike neutrinos in NOvA coincident with LIGO/Virgo detections. *Phys. Rev. D*, 104(6):063024, 2021. doi:[10.1103/PhysRevD.104.063024](https://doi.org/10.1103/PhysRevD.104.063024).
- [16] M. A. Acero et al. Search for slow magnetic monopoles with the NOvA detector on the surface. *Phys. Rev. D*, 103(1):012007, 2021. doi:[10.1103/PhysRevD.103.012007](https://doi.org/10.1103/PhysRevD.103.012007).
- [17] Peter N. Shanahan and Patricia LaVern Vahle. Physics with NOvA: a half-time review. *Eur. Phys. J. ST*, 230(24):4259–4273, 2021. doi:[10.1140/epjs/s11734-021-00285-9](https://doi.org/10.1140/epjs/s11734-021-00285-9).
- [18] Peter Shanahan and Patricia Vahle. The NOvA Physics Program through 2025. Snowmass 2021 Letters of Interest NF, 135. URL [https://www.snowmass21.org/docs/files/summaries/NF/SNOWMASS21-NF1\\_NF3\\_Patricia\\_Vahle-145.pdf](https://www.snowmass21.org/docs/files/summaries/NF/SNOWMASS21-NF1_NF3_Patricia_Vahle-145.pdf).
- [19] P. Adamson et al. The NuMI Neutrino Beam. *Nucl. Instrum. Meth. A*, 806:279–306, 2016. doi:[10.1016/j.nima.2015.08.063](https://doi.org/10.1016/j.nima.2015.08.063).
- [20] Records. URL <https://operations.fnal.gov/records/>. Performance records achieved by the Fermilab accelerators. Cited May 2024.

- [21] Katsuya Yonehara. Megawatt upgrade of numi target system. 1 2022. URL <https://www.osti.gov/biblio/1844332>.
- [22] Leonidas Aliaga Soplin. *Neutrino Flux Prediction for the NuMI Beamline*. PhD thesis, William-Mary Coll., 2016.
- [23] Leonidas Aliaga Soplin. 2017-2018 Beam Plots. NOVA Document 20843. URL <https://nova-docdb.fnal.gov/cgi-bin/sso>ShowDocument?docid=20843>. NOvA internal document.
- [24] D. S. Ayres et al. The nova technical design report. *NOvA Collaboration*, 2007. doi:[10.2172/935497](https://doi.org/10.2172/935497).
- [25] Yury Kudenko. Neutrino detectors for oscillation experiments. *JINST*, 12(06):C06003, 2017. doi:[10.1088/1748-0221/12/06/C06003](https://doi.org/10.1088/1748-0221/12/06/C06003).
- [26] S. Mufson et al. Liquid scintillator production for the NOvA experiment. *Nucl. Instrum. Meth. A*, 799:1–9, 2015. doi:[10.1016/j.nima.2015.07.026](https://doi.org/10.1016/j.nima.2015.07.026).
- [27] Alex Sousa. Density of NOvA Liquid Scintillator at 69° F. NOVA Document 11886. URL <https://nova-docdb.fnal.gov/cgi-bin/sso>ShowDocument?docid=11886>. NOvA internal document.
- [28] M.J. Berger, J.S. Coursey, M.A. Zucker, and J. Chang. ESTAR, PSTAR, and ASTAR: Computer Programs for Calculating Stopping-Power and Range Tables for Electrons, Protons, and Helium Ions (version 1.2.3). URL <http://physics.nist.gov/Star>.
- [29] Luke Vinton. Calorimetric Energy Scale Calibration of the NOvA Detectors. NOVA Document 13579, document FA\_Calorimetric\_energy\_scale.pdf. URL <https://nova-docdb.fnal.gov/cgi-bin/sso>ShowDocument?docid=13579>. NOvA Technical Note.
- [30] Xinchun Tian. NOvA Data Acquisition Software System. In *Meeting of the APS Division of Particles and Fields*, 9 2011.
- [31] Joao Coelho, Barnali Chowdhury, and Ryan Murphy. Tech note: Good data selection. NOVA Document 13546. URL <https://nova-docdb.fnal.gov/cgi-bin/sso>ShowDocument?docid=13546>. NOvA technical note.

- [32] Jonathan M. Paley. BadChannels Technical Note. NOVA Document 12771. URL <https://nova-docdb.fnal.gov/cgi-bin/sso>ShowDocument?docid=12771>. NOvA technical note.
- [33] A. Aurisano, C. Backhouse, R. Hatcher, N. Mayer, J. Musser, R. Patterson, R. Schroeter, and A. Sousa. The NOvA simulation chain. *J. Phys. Conf. Ser.*, 664(7):072002, 2015. doi:[10.1088/1742-6596/664/7/072002](https://doi.org/10.1088/1742-6596/664/7/072002).
- [34] S. Agostinelli et al. GEANT4—a simulation toolkit. *Nucl. Instrum. Meth. A*, 506: 250–303, 2003. doi:[10.1016/S0168-9002\(03\)01368-8](https://doi.org/10.1016/S0168-9002(03)01368-8).
- [35] Zarko Pavlovic. *Observation of Disappearance of Muon Neutrinos in the NuMI Beam*. PhD thesis, Texas U., 2008.
- [36] L. Aliaga et al. Neutrino Flux Predictions for the NuMI Beam. *Phys. Rev. D*, 94(9):092005, 2016. doi:[10.1103/PhysRevD.94.092005](https://doi.org/10.1103/PhysRevD.94.092005). [Addendum: *Phys. Rev. D* 95, 039903 (2017)].
- [37] C. Alt et al. Inclusive production of charged pions in p+C collisions at 158-GeV/c beam momentum. *Eur. Phys. J. C*, 49:897–917, 2007. doi:[10.1140/epjc/s10052-006-0165-7](https://doi.org/10.1140/epjc/s10052-006-0165-7).
- [38] Gemma Maria Tinti. *Sterile neutrino oscillations in MINOS and hadron production in pC collisions*. PhD thesis, 2010.
- [39] B Baatar, G Barr, J Bartke, L Betev, O Chvala, J Dolejsi, V Eckardt, HG Fischer, Z Fodor, A Karev, et al. Inclusive production of protons, anti-protons, neutrons, deuterons and tritons in p+ c collisions at 158 gev/c beam momentum. *The European Physical Journal C*, 73:1–66, 2013. doi:[10.1140/epjc/s10052-013-2364-3](https://doi.org/10.1140/epjc/s10052-013-2364-3).
- [40] D. S. Barton et al. Experimental study of the  $a$  dependence of inclusive hadron fragmentation. *Phys. Rev. D*, 27:2580–2599, Jun 1983. doi:[10.1103/PhysRevD.27.2580](https://doi.org/10.1103/PhysRevD.27.2580).
- [41] Andrey V. Lebedev. *Ratio of Pion Kaon Production in Proton Carbon Interactions*. PhD thesis, 2007.

- [42] T.T. Böhlen, F. Cerutti, M.P.W. Chin, A. Fassò, A. Ferrari, P.G. Ortega, A. Mairani, P.R. Sala, G. Smirnov, and V. Vlachoudis. The fluka code: Developments and challenges for high energy and medical applications. *Nuclear Data Sheets*, 120:211–214. ISSN 0090-3752. doi:[10.1016/j.nds.2014.07.049](https://doi.org/10.1016/j.nds.2014.07.049).
- [43] Alfredo Ferrari, Paola R. Sala, Alberto Fasso, and Johannes Ranft. FLUKA: A multi-particle transport code (Program version 2005). 10 2005. doi:[10.2172/877507](https://doi.org/10.2172/877507).
- [44] A. Aduszkiewicz et al. Measurements of production and inelastic cross sections for p+C , p+Be , and p+Al at 60 GeV/c and p+C and p+Be at 120 GeV/c. *Phys. Rev. D*, 100(11):112001, 2019. doi:[10.1103/PhysRevD.100.112001](https://doi.org/10.1103/PhysRevD.100.112001).
- [45] H. Adhikary et al. Measurements of  $\pi^+$ ,  $\pi^-$ ,  $p$ ,  $\bar{p}$ ,  $K^+$  and  $K^-$  production in 120 GeV/c p + C interactions. *Phys. Rev. D*, 108:072013, 2023. doi:[10.1103/PhysRevD.108.072013](https://doi.org/10.1103/PhysRevD.108.072013).
- [46] H. Adhikary et al. Measurements of KS0,  $\Lambda$ , and  $\Lambda^-$  production in 120 GeV/c p+C interactions. *Phys. Rev. D*, 107(7):072004, 2023. doi:[10.1103/PhysRevD.107.072004](https://doi.org/10.1103/PhysRevD.107.072004).
- [47] A. Aduszkiewicz et al. Measurements of hadron production in  $\pi^+ + C$  and  $\pi^+ + Be$  interactions at 60 GeV/c. *Phys. Rev. D*, 100(11):112004, 2019. doi:[10.1103/PhysRevD.100.112004](https://doi.org/10.1103/PhysRevD.100.112004).
- [48] Matej Pavin. Hadron production measurements for neutrino experiments, 2020. URL [https://indico.fnal.gov/event/43209/contributions/187869/attachments/130502/159028/HadronProduction\\_neutrino2020.pdf](https://indico.fnal.gov/event/43209/contributions/187869/attachments/130502/159028/HadronProduction_neutrino2020.pdf). Presented on Neutrino 2020 conference.
- [49] T. Akaishi et al. EMPHATIC: A Proposed Experiment to Measure Hadron Scattering and Production Cross Sections for Improved Neutrino Flux Predictions. 12 2019.
- [50] C. Andreopoulos et al. The GENIE Neutrino Monte Carlo Generator. *Nucl. Instrum. Meth. A*, 614:87–104, 2010. doi:[10.1016/j.nima.2009.12.009](https://doi.org/10.1016/j.nima.2009.12.009).

- [51] J. Nieves, J. E. Amaro, and M. Valverde. Inclusive quasielastic charged-current neutrino-nucleus reactions. *Phys. Rev. C*, 70:055503, Nov 2004. doi:[10.1103/PhysRevC.70.055503](https://doi.org/10.1103/PhysRevC.70.055503).
- [52] Aaron S. Meyer, Minerba Betancourt, Richard Gran, and Richard J. Hill. Deuterium target data for precision neutrino-nucleus cross sections. *Phys. Rev. D*, 93:113015, Jun 2016. doi:[10.1103/PhysRevD.93.113015](https://doi.org/10.1103/PhysRevD.93.113015).
- [53] J. Nieves, I. Ruiz Simo, and M. J. Vicente Vacas. Inclusive charged-current neutrino-nucleus reactions. *Phys. Rev. C*, 83:045501, Apr 2011. doi:[10.1103/PhysRevC.83.045501](https://doi.org/10.1103/PhysRevC.83.045501).
- [54] R. Gran, J. Nieves, F. Sanchez, and M. J. Vicente Vacas. Neutrino-nucleus quasielastic and 2p2h interactions up to 10 gev. *Phys. Rev. D*, 88:113007, Dec 2013. doi:[10.1103/PhysRevD.88.113007](https://doi.org/10.1103/PhysRevD.88.113007).
- [55] Ch. Berger and L. M. Sehgal. Lepton mass effects in single pion production by neutrinos. *Phys. Rev. D*, 76:113004, Dec 2007. doi:[10.1103/PhysRevD.76.113004](https://doi.org/10.1103/PhysRevD.76.113004).
- [56] Ch. Berger and L. M. Sehgal. Partially conserved axial vector current and coherent pion production by low energy neutrinos. *Phys. Rev. D*, 79:053003, Mar 2009. doi:[10.1103/PhysRevD.79.053003](https://doi.org/10.1103/PhysRevD.79.053003).
- [57] A Bodek and U. K. Yang. Higher twist, xi(omega) scaling, and effective LO PDFs for lepton scattering in the few GeV region. *J. Phys. G*, 29:1899–1906, 2003. doi:[10.1088/0954-3899/29/8/369](https://doi.org/10.1088/0954-3899/29/8/369).
- [58] T. Yang, C. Andreopoulos, H. Gallagher, K. Hoffmann, and P. Kehayias. A Hadronization Model for Few-GeV Neutrino Interactions. *Eur. Phys. J. C*, 63: 1–10, 2009. doi:[10.1140/epjc/s10052-009-1094-z](https://doi.org/10.1140/epjc/s10052-009-1094-z).
- [59] L.L. Salcedo, E. Oset, M.J. Vicente-Vacas, and C. Garcia-Recio. Computer simulation of inclusive pion nuclear reactions. *Nuclear Physics A*, 484(3):557–592. ISSN 0375-9474. doi:[10.1016/0375-9474\(88\)90310-7](https://doi.org/10.1016/0375-9474(88)90310-7).
- [60] Chris Hagmann, David Lange, and Douglas Wright. Cosmic-ray shower generator (cry) for monte carlo transport codes. volume 2, pages 1143 – 1146. ISBN 978-1-4244-0922-8. doi:[10.1109/NSSMIC.2007.4437209](https://doi.org/10.1109/NSSMIC.2007.4437209).

- [61] C. N. Chou. The nature of the saturation effect of fluorescent scintillators. *Phys. Rev.*, 87:904–905, Sep 1952. doi:[10.1103/PhysRev.87.904](https://doi.org/10.1103/PhysRev.87.904).
- [62] M. Baird, J. Bian, M. Messier, E. Niner, D. Rocco, and K. Sachdev. Event Reconstruction Techniques in NOvA. *J. Phys. Conf. Ser.*, 664(7):072035, 2015. doi:[10.1088/1742-6596/664/7/072035](https://doi.org/10.1088/1742-6596/664/7/072035).
- [63] Martin Ester, Hans-Peter Kriegel, Jörg Sander, and Xiaowei Xu. A density-based algorithm for discovering clusters in large spatial databases with noise. In *Proceedings of the Second International Conference on Knowledge Discovery and Data Mining*, KDD’96, page 226–231. AAAI Press, 1996. doi:[10.5555/3001460.3001507](https://doi.org/10.5555/3001460.3001507).
- [64] Leandro A. F. Fernandes and Manuel Menezes de Oliveira Neto. Real-time line detection through an improved hough transform voting scheme. *Pattern Recognit.*, 41:299–314, 2008. doi:[10.1016/j.patcog.2007.04.003](https://doi.org/10.1016/j.patcog.2007.04.003). URL <https://api.semanticscholar.org/CorpusID:5996185>.
- [65] Mattias Ohlsson, Carsten Peterson, and Alan L. Yuille. Track finding with deformable templates – the elastic arms approach. *Computer Physics Communications*, 71(1):77–98. ISSN 0010-4655. doi:[10.1016/0010-4655\(92\)90074-9](https://doi.org/10.1016/0010-4655(92)90074-9). URL <https://www.sciencedirect.com/science/article/pii/0010465592900749>.
- [66] R. Krishnapuram and J.M. Keller. A possibilistic approach to clustering. *IEEE Transactions on Fuzzy Systems*, 1(2):98–110, 1993. doi:[10.1109/91.227387](https://doi.org/10.1109/91.227387).
- [67] Miin-Shen Yang and Kuo-Lung Wu. Unsupervised possibilistic clustering. *Pattern Recognition*, 39(1):5–21. ISSN 0031-3203. doi:<https://doi.org/10.1016/j.patcog.2005.07.005>. URL <https://www.sciencedirect.com/science/article/pii/S0031320305002943>.
- [68] Jianming Bian, Hongyue Duyang, and Alexander Radovic. Blessing package for Neutrino-Electron Scattering and Coherent Pi0. NOVA Document 13862. URL <https://nova-docdb.fnal.gov/cgi-bin/sso>ShowDocument?docid=13862>. NOvA internal document.

- [69] Nicholas Jacob Raddatz. *Measurement of Muon Neutrino Disappearance with Non-Fiducial Interactions in the NO<sub>v</sub>A Experiment*. PhD thesis, Minnesota U., 2016.
- [70] Michael David Baird. *An Analysis of Muon Neutrino Disappearance from the NuMI Beam Using an Optimal Track Fitter*. PhD thesis, Indiana U., 2015.
- [71] G. Lutz. Optimum track fitting in the presence of multiple scattering. *Nuclear Instruments and Methods in Physics Research Section A: Accelerators, Spectrometers, Detectors and Associated Equipment*, 273(1):349–361. ISSN 0168-9002. doi:[https://doi.org/10.1016/0168-9002\(88\)90836-4](https://doi.org/10.1016/0168-9002(88)90836-4). URL <https://www.sciencedirect.com/science/article/pii/0168900288908364>.
- [72] Brian Rebel. Window tracking algorithm for cosmic ray muons. NOVA Document 15977-v1. URL <https://nova-docdb.fnal.gov/cgi-bin/sso>ShowDocument?docid=15977>. NOvA internal document.
- [73] Christian Szegedy, Wei Liu, Yangqing Jia, Pierre Sermanet, Scott Reed, Dragomir Anguelov, Dumitru Erhan, Vincent Vanhoucke, and Andrew Rabinovich. Going Deeper with Convolutions. *arXiv e-prints*, art. arXiv:1409.4842. doi:[10.48550/arXiv.1409.4842](https://doi.org/10.48550/arXiv.1409.4842).
- [74] A. Aurisano, A. Radovic, D. Rocco, A. Himmel, M.D. Messier, E. Niner, G. Pawloski, F. Psihas, A. Sousa, and P. Vahle. A Convolutional Neural Network Neutrino Event Classifier. *JINST*, 11(09):P09001, 2016. doi:[10.1088/1748-0221/11/09/P09001](https://doi.org/10.1088/1748-0221/11/09/P09001).
- [75] Fernanda Psihas. Measurement of long baseline neutrino oscillations and improvements from deep learning. 1 2018. doi:[10.2172/1437288](https://doi.org/10.2172/1437288). URL <https://www.osti.gov/biblio/1437288>.
- [76] Prabhjot Singh. *Extraction of Neutrino Oscillation Parameters using a Simultaneous Fit of  $\nu_\mu$  Disappearance and  $\nu_e$  Appearance data with the NO<sub>v</sub>A Experiment*. PhD thesis, University of Delhi, Dept. of Physics and Astrophysics, India, Delhi U., 9 2019.

- [77] Ryan J. Nichol. Fibre brightness from cosmic muon data. NOVA Document 34909. URL <https://nova-docdb.fnal.gov/cgi-bin/sso>ShowDocument?docid=34909>. NOvA technical note.
- [78] Prabhjot Singh. Attenuation Calibration of the NOvA Detectors. In *The 38th International Conference on High Energy Physics (ICHEP 2016)*, 2024. URL <https://nova-docdb.fnal.gov/cgi-bin/sso>ShowDocument?docid=15840>. (cited on 03.2024).
- [79] Patrick Huber et al. Snowmass Neutrino Frontier Report. In *Snowmass 2021*, 11 2022.
- [80] E. Aprile et al. Excess electronic recoil events in XENON1T. *Phys. Rev. D*, 102: 072004, . doi:[10.1103/PhysRevD.102.072004](https://doi.org/10.1103/PhysRevD.102.072004).
- [81] E. Aprile et al. Search for New Physics in Electronic Recoil Data from XENONnT. *Phys. Rev. Lett.*, 129:161805, . doi:[10.1103/PhysRevLett.129.161805](https://doi.org/10.1103/PhysRevLett.129.161805).
- [82] M. Atzori Corona, W. M. Bonivento, M. Cadeddu, N. Cargioli, and F. Dordei. New constraint on neutrino magnetic moment and neutrino millicharge from LUX-ZEPLIN dark matter search results. *Phys. Rev. D*, 107:053001. doi:[10.1103/PhysRevD.107.053001](https://doi.org/10.1103/PhysRevD.107.053001).
- [83] M. Agostini et al. Limiting neutrino magnetic moments with Borexino Phase-II solar neutrino data. *Phys. Rev. D*, 96:091103. doi:[10.1103/PhysRevD.96.091103](https://doi.org/10.1103/PhysRevD.96.091103).
- [84] Amir N. Khan. Light new physics and neutrino electromagnetic interactions in XENONnT. *Physics Letters B*, 837:137650. ISSN 0370-2693. doi:[10.1016/j.physletb.2022.137650](https://doi.org/10.1016/j.physletb.2022.137650). URL <https://www.sciencedirect.com/science/article/pii/S0370269322007845>.
- [85] K. S. Babu, Sudip Jana, and Manfred Lindner. Large Neutrino Magnetic Moments in the Light of Recent Experiments. *JHEP*, 10:040. doi:[10.1007/JHEP10\(2020\)040](https://doi.org/10.1007/JHEP10(2020)040).
- [86] L. B. Auerbach et al. Measurement of electron-neutrino electron elastic scattering. *Phys. Rev. D*, 63:112001. doi:[10.1103/PhysRevD.63.112001](https://doi.org/10.1103/PhysRevD.63.112001).

- [87] D. A. Krakauer et al. Limits on the neutrino magnetic moment from a measurement of neutrino - electron elastic scattering. *252*:177–180. doi:[10.1016/0370-2693\(90\)91100-P](https://doi.org/10.1016/0370-2693(90)91100-P).
- [88] L. A. Ahrens et al. Determination of electroweak parameters from the elastic scattering of muon neutrinos and antineutrinos on electrons. *Phys. Rev. D*, **41**: 3297–3316, Jun 1990. doi:[10.1103/PhysRevD.41.3297](https://doi.org/10.1103/PhysRevD.41.3297).
- [89] P. Vilain et al. Experimental study of electromagnetic properties of the muon-neutrino in neutrino - electron scattering. *Phys. Lett. B*, **345**:115–118, 1995. doi:[10.1016/0370-2693\(94\)01678-6](https://doi.org/10.1016/0370-2693(94)01678-6).
- [90] Biao Wang. *Muon-Neutrino Electron Elastic Scattering and a Search for the Muon-Neutrino Magnetic Moment in the NOvA Near Detector*. PhD thesis. URL [https://scholar.smu.edu/hum\\_sci\\_physics\\_etds/1](https://scholar.smu.edu/hum_sci_physics_etds/1).
- [91] Wenjie Wu and Yiwen Xiao. Constraint of the Integrated Neutrino Flux from Neutrino-Electron Elastic Scattering in the NOvA Near Detector. NOVA Document 56383. URL <https://nova-docdb.fnal.gov/cgi-bin/sso>ShowDocument?docid=56383>. NOvA technical note.
- [92] Athula Wickremasinghe, Wenjie Wu, and Yiwen Xiao. Status of the Measurement of Neutrino-Electron Elastic Scattering in the NOvA Near Detector. In *Neutrino 2022*. URL <https://indico.kps.or.kr/event/30/contributions/738/>.
- [93] Barnali Brahma, Tyler Horoho, and Mu Wei. TechNote: Light Dark Matter Search with NOvA Near Detector. NOVA Document 59439. URL <https://nova-docdb.fnal.gov/cgi-bin/sso>ShowDocument?docid=59439>. NOvA technical note.
- [94] Carlo Giunti and Alexander Studenikin. Neutrino electromagnetic interactions: A window to new physics. *Rev. Mod. Phys.*, **87**:531–591, Jun 2015. doi:[10.1103/RevModPhys.87.531](https://doi.org/10.1103/RevModPhys.87.531).
- [95] Boris Kayser. Majorana neutrinos and their electromagnetic properties. *Phys. Rev. D*, **26**:1662–1670, Oct 1982. doi:[10.1103/PhysRevD.26.1662](https://doi.org/10.1103/PhysRevD.26.1662).

- [96] José F. Nieves. Electromagnetic properties of majorana neutrinos. *Phys. Rev. D*, 26:3152–3158, Dec 1982. doi:[10.1103/PhysRevD.26.3152](https://doi.org/10.1103/PhysRevD.26.3152).
- [97] Carlo Giunti, Julieta Gruszko, Benjamin Jones, Lisa Kaufman, Diana Parno, and Andrea Pocar. Report of the Topical Group on Neutrino Properties for Snowmass 2021. 9 2022.
- [98] R. L. Workman and Others. Review of Particle Physics. *PTEP*, 2022:083C01, 2022. doi:[10.1093/ptep/ptac097](https://doi.org/10.1093/ptep/ptac097).
- [99] Nicole F. Bell, Mikhail Gorchtein, Michael J. Ramsey-Musolf, Petr Vogel, and Peng Wang. Model independent bounds on magnetic moments of Majorana neutrinos. *Phys. Lett. B*, 642:377–383, 2006. doi:[10.1016/j.physletb.2006.09.055](https://doi.org/10.1016/j.physletb.2006.09.055).
- [100] Nicole F. Bell, Vincenzo Cirigliano, Michael J. Ramsey-Musolf, Petr Vogel, and Mark B. Wise. How magnetic is the Dirac neutrino? *Phys. Rev. Lett.*, 95:151802, 2005. doi:[10.1103/PhysRevLett.95.151802](https://doi.org/10.1103/PhysRevLett.95.151802).
- [101] M.C. Gonzalez-Garcia and Michele Maltoni. Phenomenology with Massive Neutrinos. *Phys. Rept.*, 460:1–129, 2008. doi:[10.1016/j.physrep.2007.12.004](https://doi.org/10.1016/j.physrep.2007.12.004).
- [102] Carlo Giunti and Chung W. Kim. *Fundamentals of Neutrino Physics and Astrophysics*. 2007. ISBN 978-0-19-850871-7.
- [103] P. Vogel and J. Engel. Neutrino electromagnetic form factors. *Phys. Rev. D*, 39: 3378–3383, Jun 1989. doi:[10.1103/PhysRevD.39.3378](https://doi.org/10.1103/PhysRevD.39.3378).
- [104] E. Valencia et al. Constraint of the MINER $\nu$ a medium energy neutrino flux using neutrino-electron elastic scattering. *Phys. Rev. D*, 100:092001, Nov 2019. doi:[10.1103/PhysRevD.100.092001](https://doi.org/10.1103/PhysRevD.100.092001).
- [105] Jens Erler and Shufang Su. The weak neutral current. 71:119–149. ISSN 0146-6410. doi:<https://doi.org/10.1016/j.ppnp.2013.03.004>. URL <https://www.sciencedirect.com/science/article/pii/S0146641013000239>. Fundamental Symmetries in the Era of the LHC.
- [106] D.Yu Bardin and V.A. Dokuchaeva. On one-loop electroweak corrections to neutrino-electron elastic scattering. 246(2):221–230. ISSN 0550-

3213. doi:[https://doi.org/10.1016/0550-3213\(84\)90293-1](https://doi.org/10.1016/0550-3213(84)90293-1). URL <https://www.sciencedirect.com/science/article/pii/0550321384902931>.
- [107] Teresa Lackey. Data Quality Technical Note Prod5.1/2023. NOVA Document 59876. URL <https://nova-docdb.fnal.gov/cgi-bin/sso>ShowDocument?docid=59876>. NOvA technical note.
- [108] Erin Ewart. Primary and Secondary Vertexing Update for February 2024 Collaboration Meeting. NOVA Document 61190, February 2024. URL <https://nova-docdb.fnal.gov/cgi-bin/sso>ShowDocument?docid=61190>. NOvA internal document.
- [109] Leonidas Aliaga, Derek Doyle, Matthew Judah, Norm Buchanan, Linda Cremonesi, Mat Muether, and Jon Paley. Measurement of the Double-Differential Inclusive Electron-Neutrino Charged-Current Cross Section in the NOvA Near Detector. NOVA Document 37668, 04 2020. URL <https://nova-docdb.fnal.gov/cgi-bin/sso>ShowDocument?docid=37668>. NOvA technical note.
- [110] Rene Brun et al. root-project/root: v6.22/08. URL <https://doi.org/10.5281/zenodo.3895860>.
- [111] Andreas Hoecker, Peter Speckmayer, Joerg Stelzer, Jan Therhaag, Eckhard von Toerne, and Helge Voss. TMVA: Toolkit for Multivariate Data Analysis. *PoS*, ACAT:040, 2007.

## APPENDIX A

# Test Beam Calibration Validation Plots

### A.1 Distributions for Stopping Muons

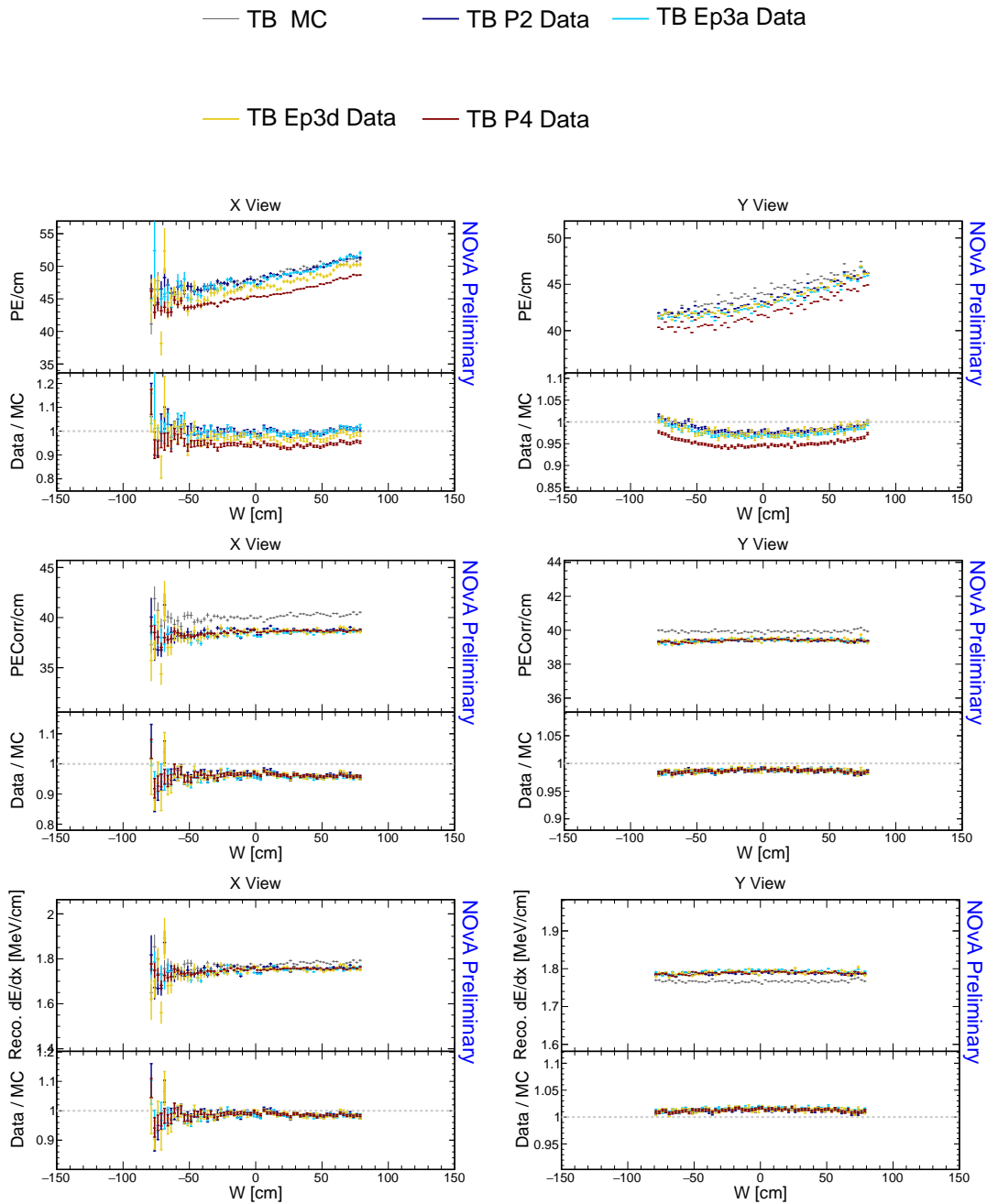


Figure A.1: Distributions of stopping muons within a 1-2 m track window from the end of their tracks across the position within a cell.

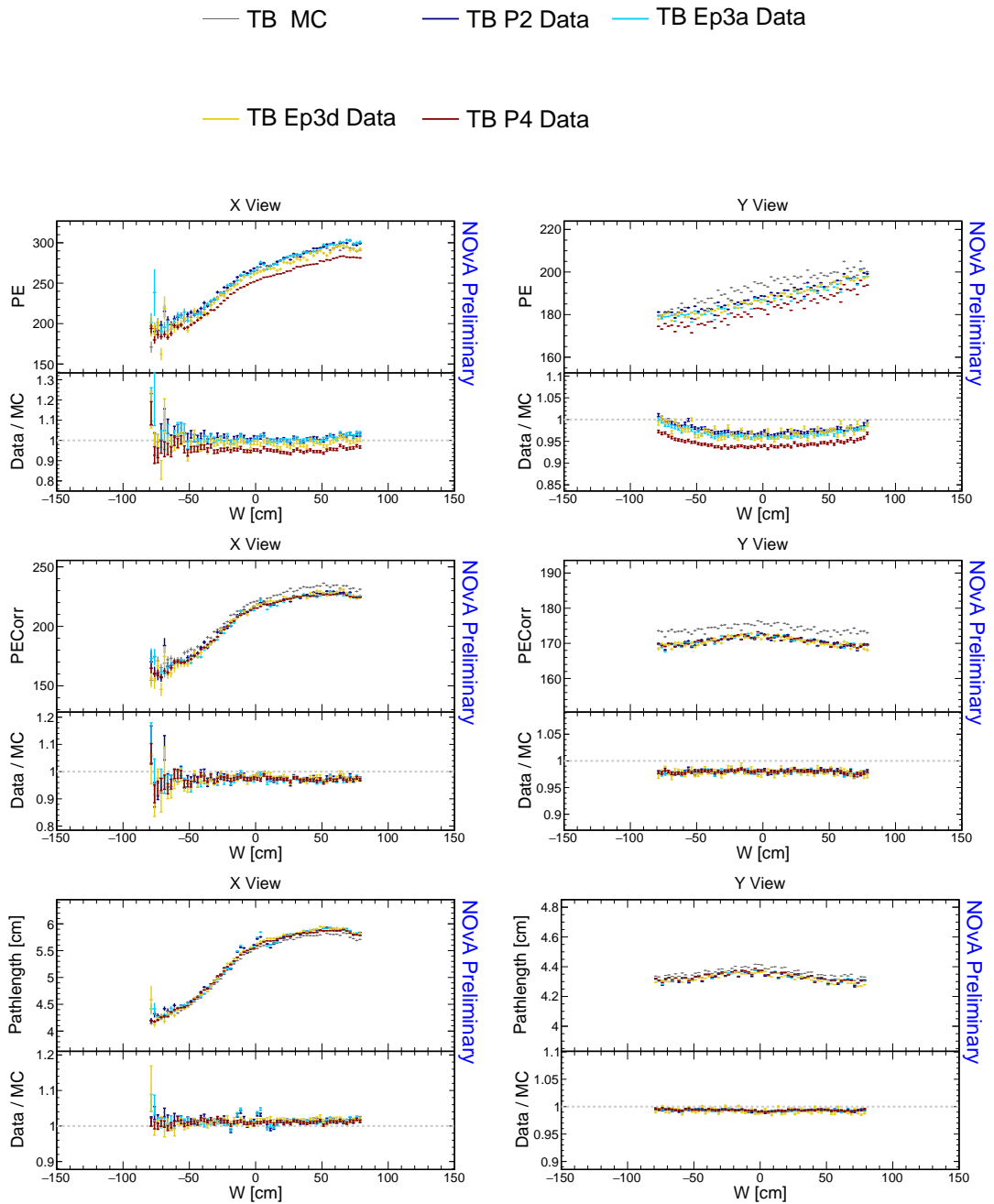


Figure A.2: Distributions of stopping muons within a 1-2 m track window from the end of their tracks across the position within a cell.

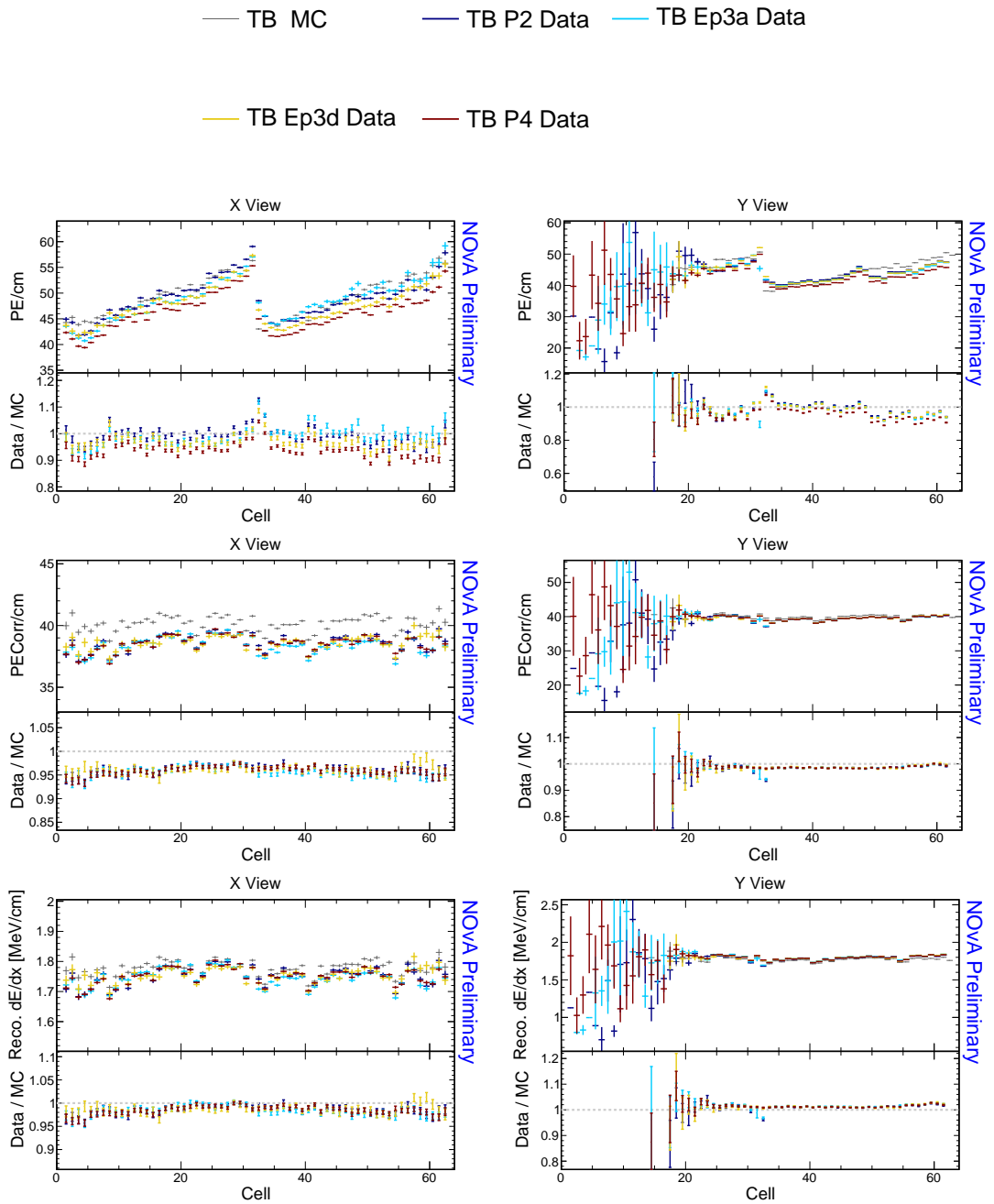


Figure A.3: Distributions of stopping muons within a 1-2 m track window from the end of their tracks across the cells of the detector.

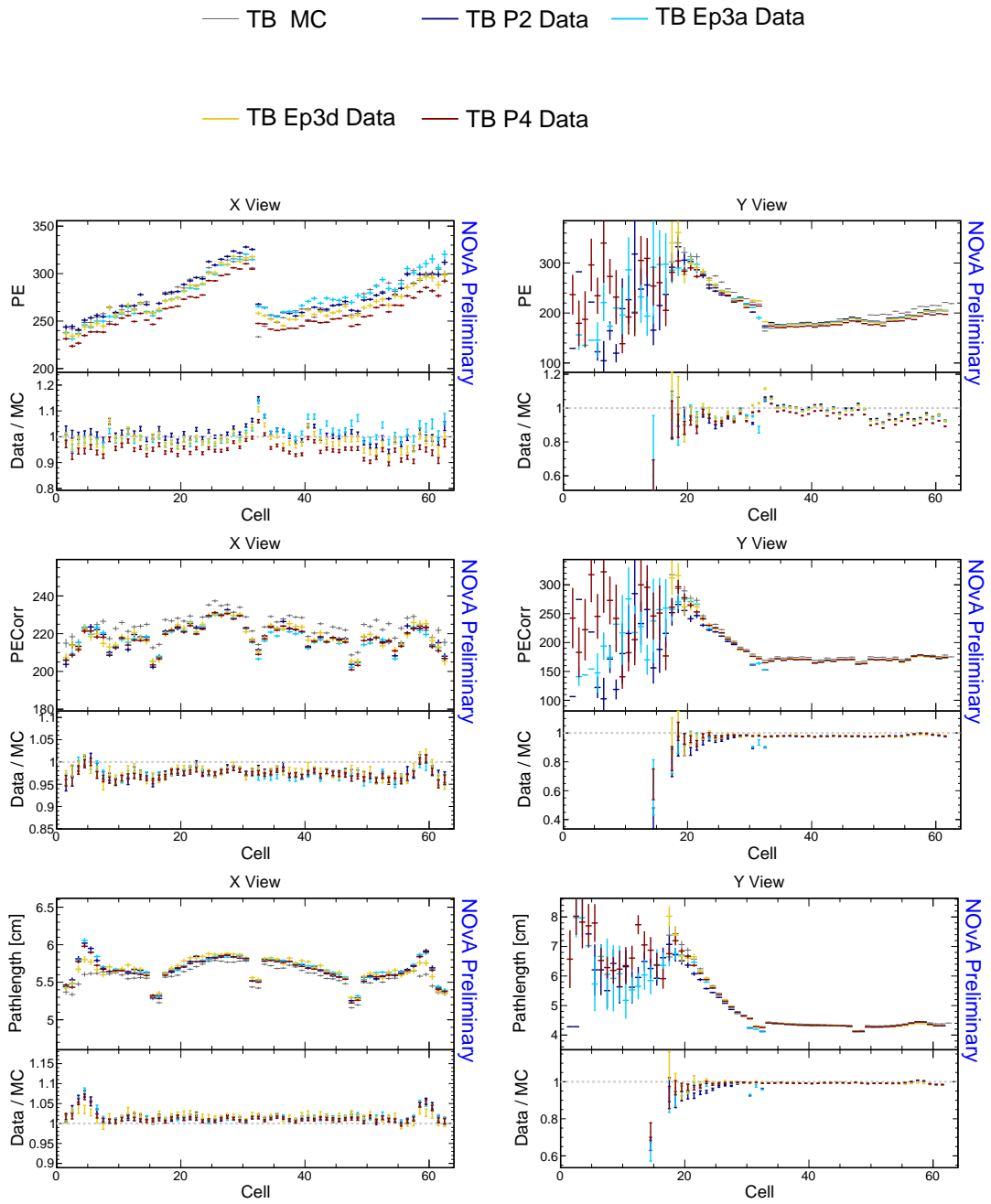


Figure A.4: Distributions of stopping muons within a 1-2 m track window from the end of their tracks across the cells of the detector.

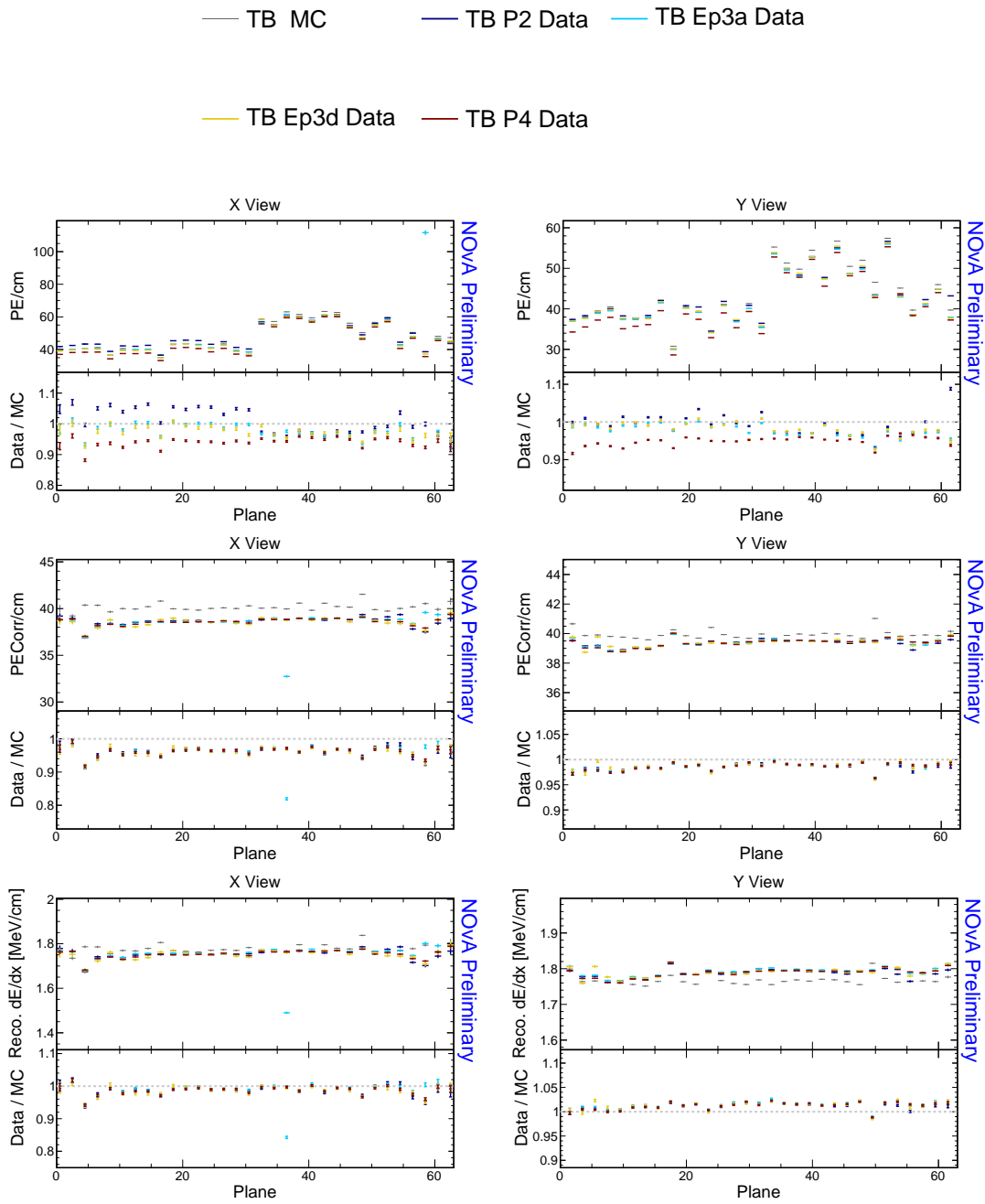


Figure A.5: Distributions of stopping muons within a 1-2 m track window from the end of their tracks across the planes of the detector.

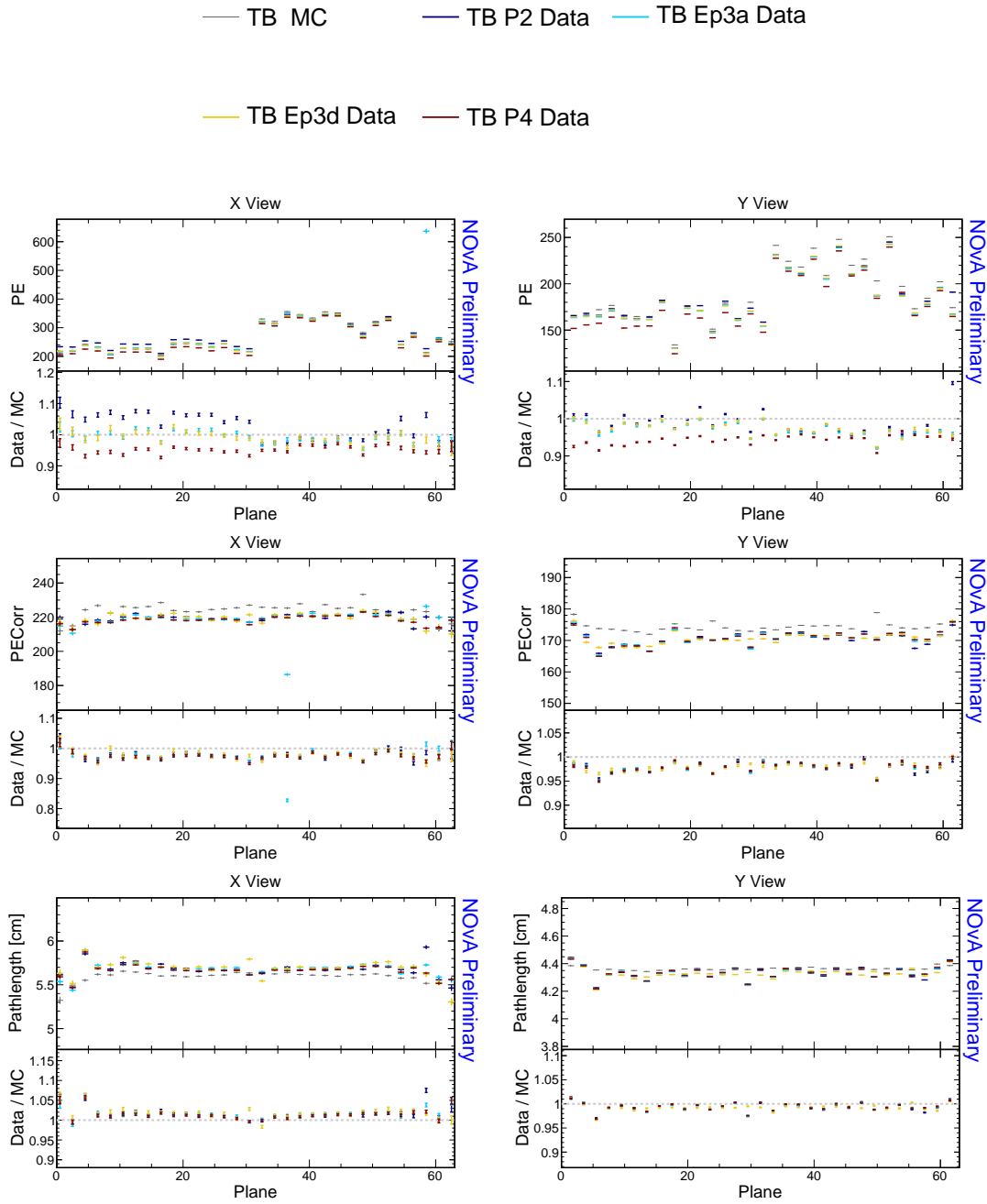


Figure A.6: Distributions of stopping muons within a 1-2 m track window from the end of their tracks across the planes of the detector.

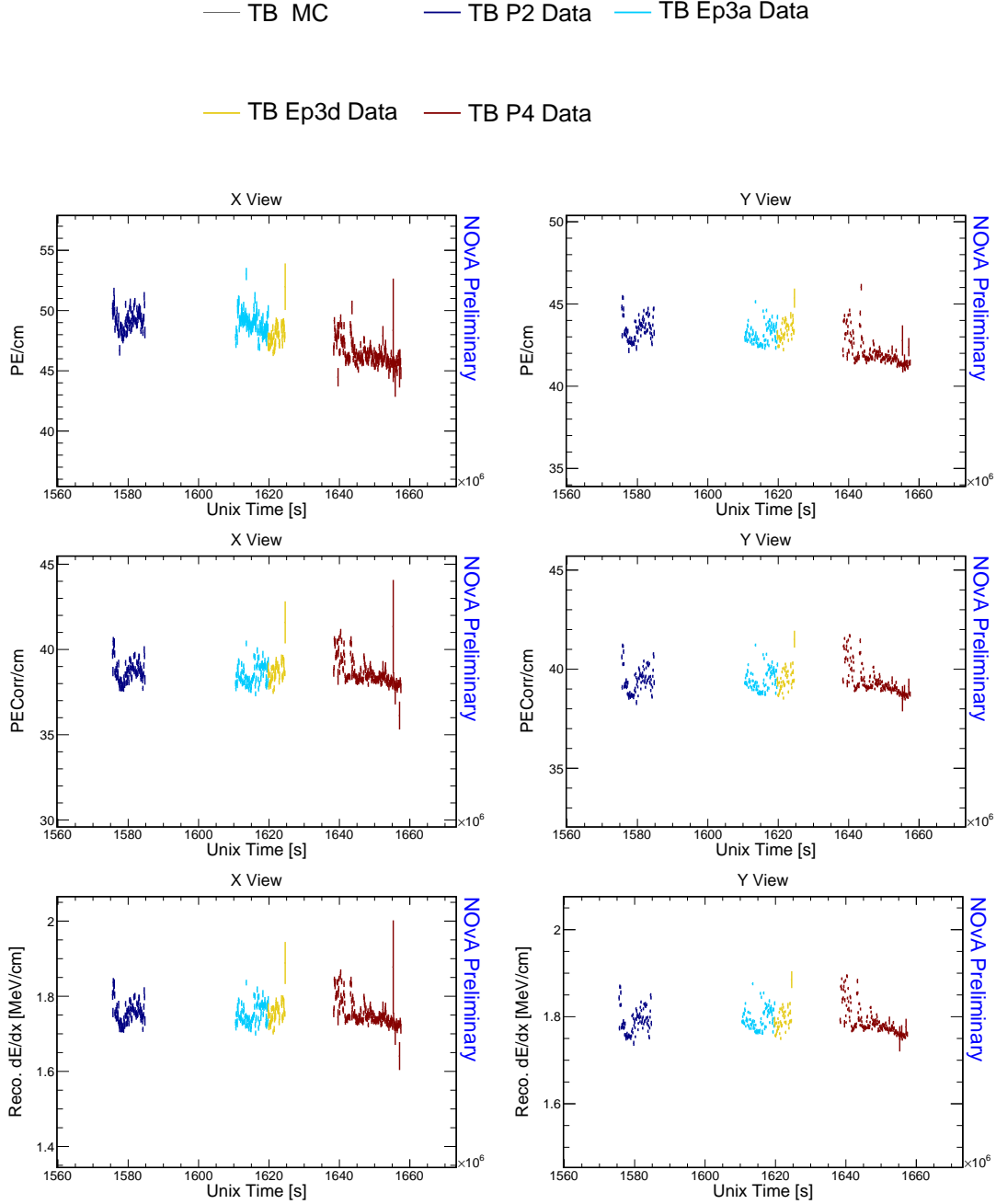


Figure A.7: Distributions of stopping muons within a 1-2 m track window from the end of their tracks across the event UNIX time.

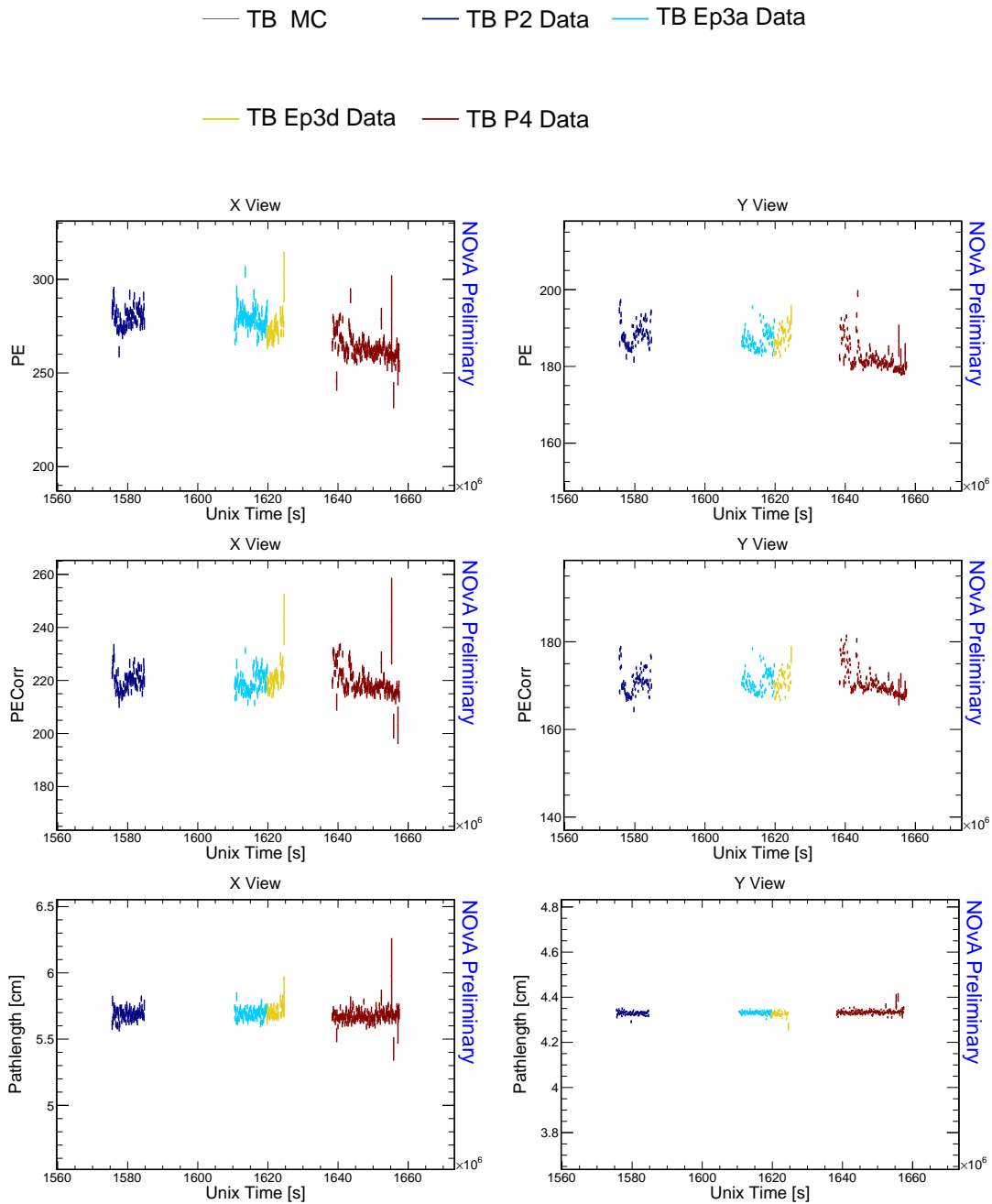


Figure A.8: Distributions of stopping muons within a 1-2 m track window from the end of their tracks across the event UNIX time.

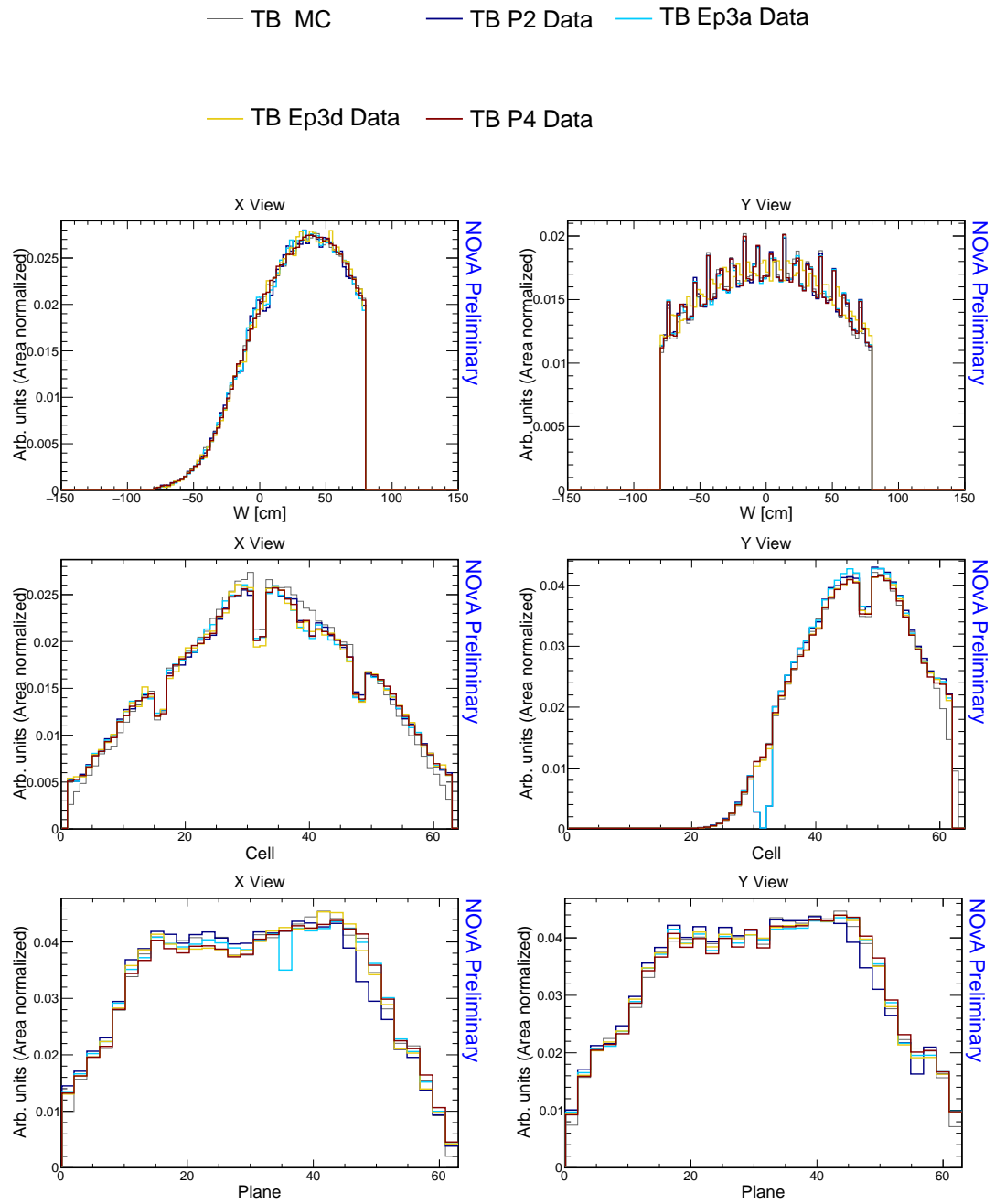


Figure A.9: Distributions of stopping muons within a 1-2 m track window from the end of their tracks.

## A.2 Distributions for Through-going Muons

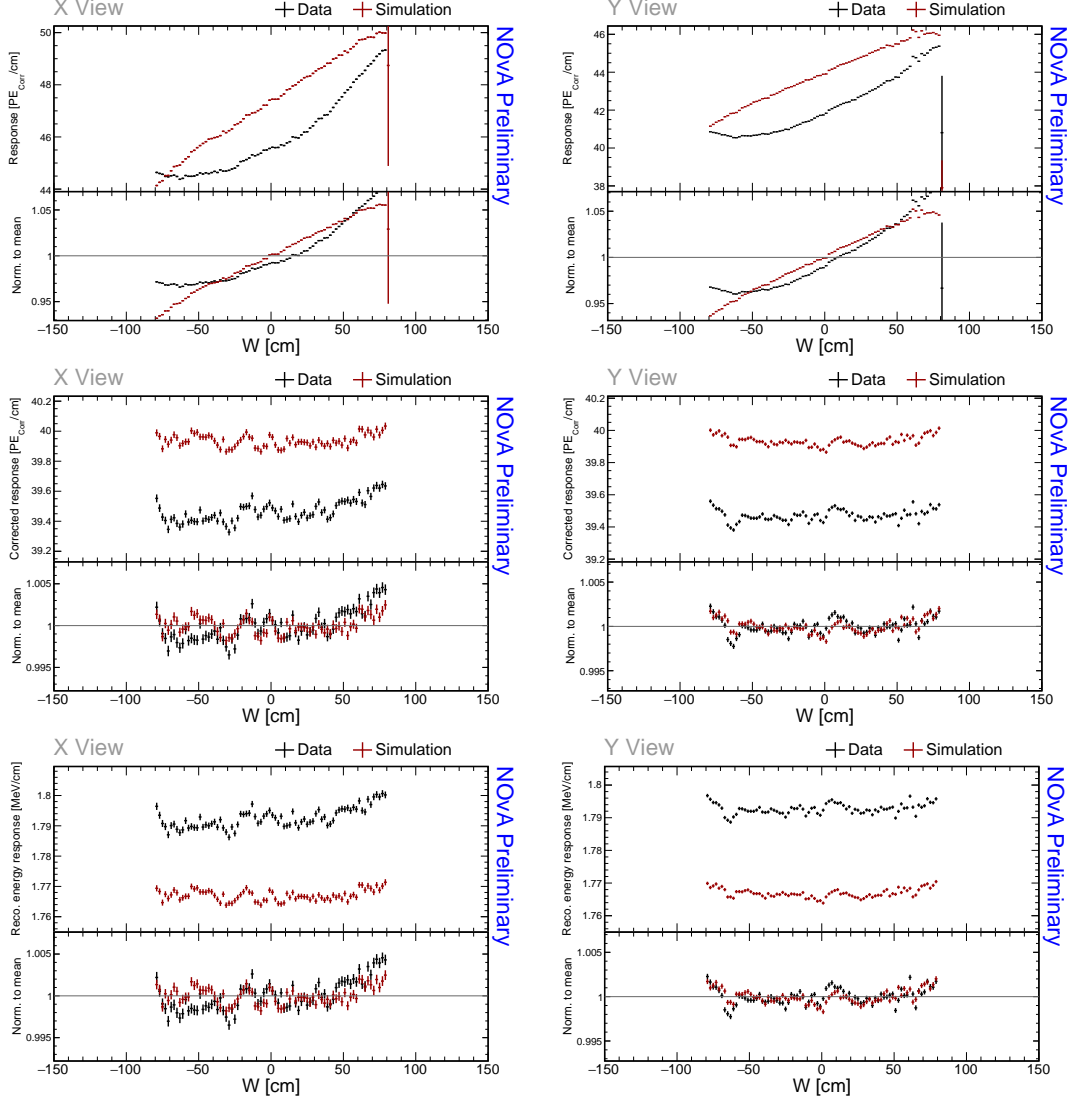


Figure A.10: Distributions of through-going cosmic muons with  $w \in (-80, 80)$  cm as a function of  $w$  for stable runs in the Test Beam period 4 data (black) and data-based simulation (red). Bottom panel of each plot shows the ratio of each bin and the mean y axis, separately for data and simulation. Discrepancy in the right-most bin is solely due to binning.

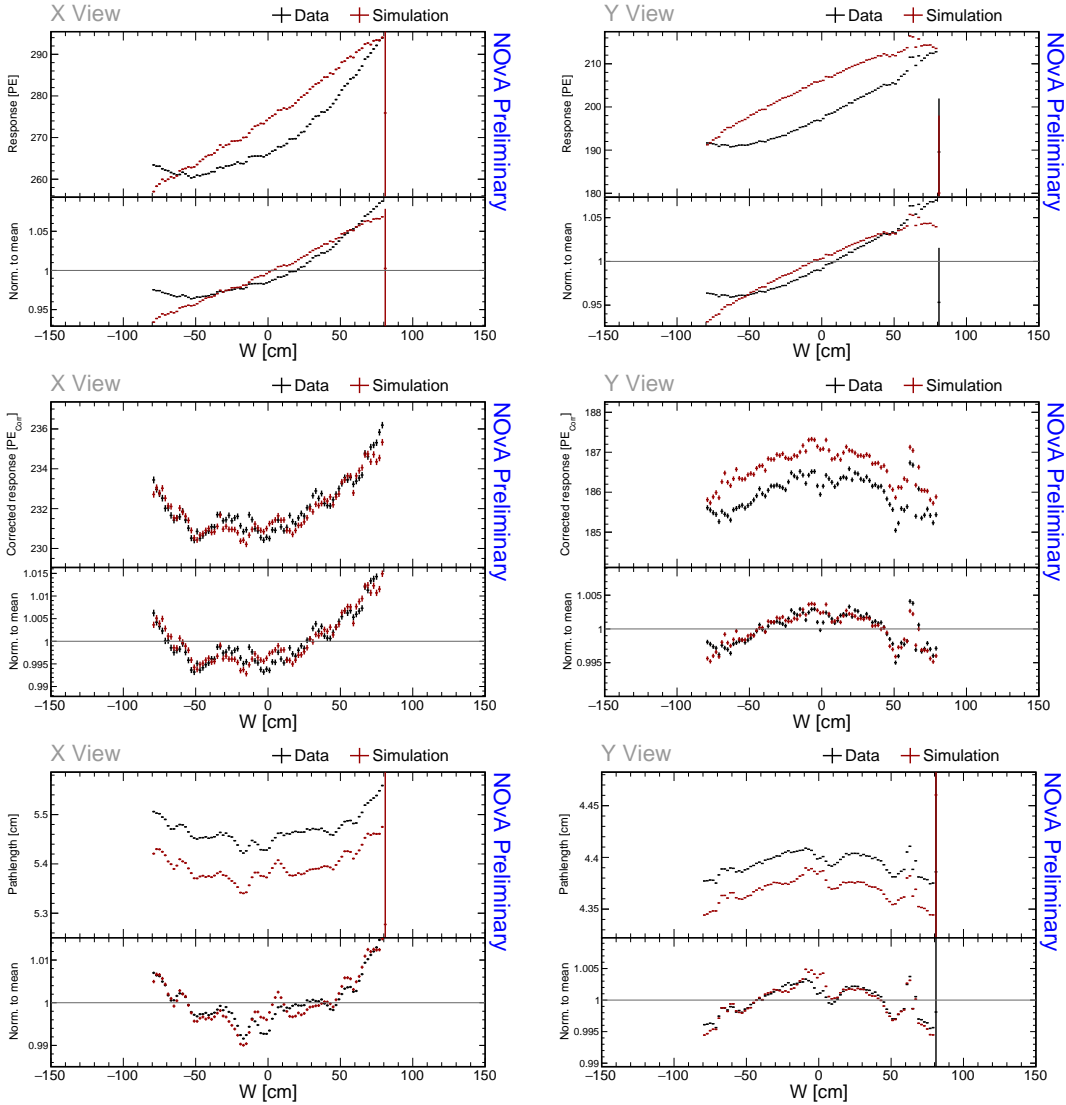


Figure A.11: Distributions of through-going cosmic muons with  $w \in (-80, 80)$  cm as a function of  $w$  for stable runs in the Test Beam period 4 data (black) and data-based simulation (red). Bottom panel of each plot shows the ratio of each bin and the mean y axis, separately for data and simulation. Discrepancy in the right-most bin is solely due to binning.

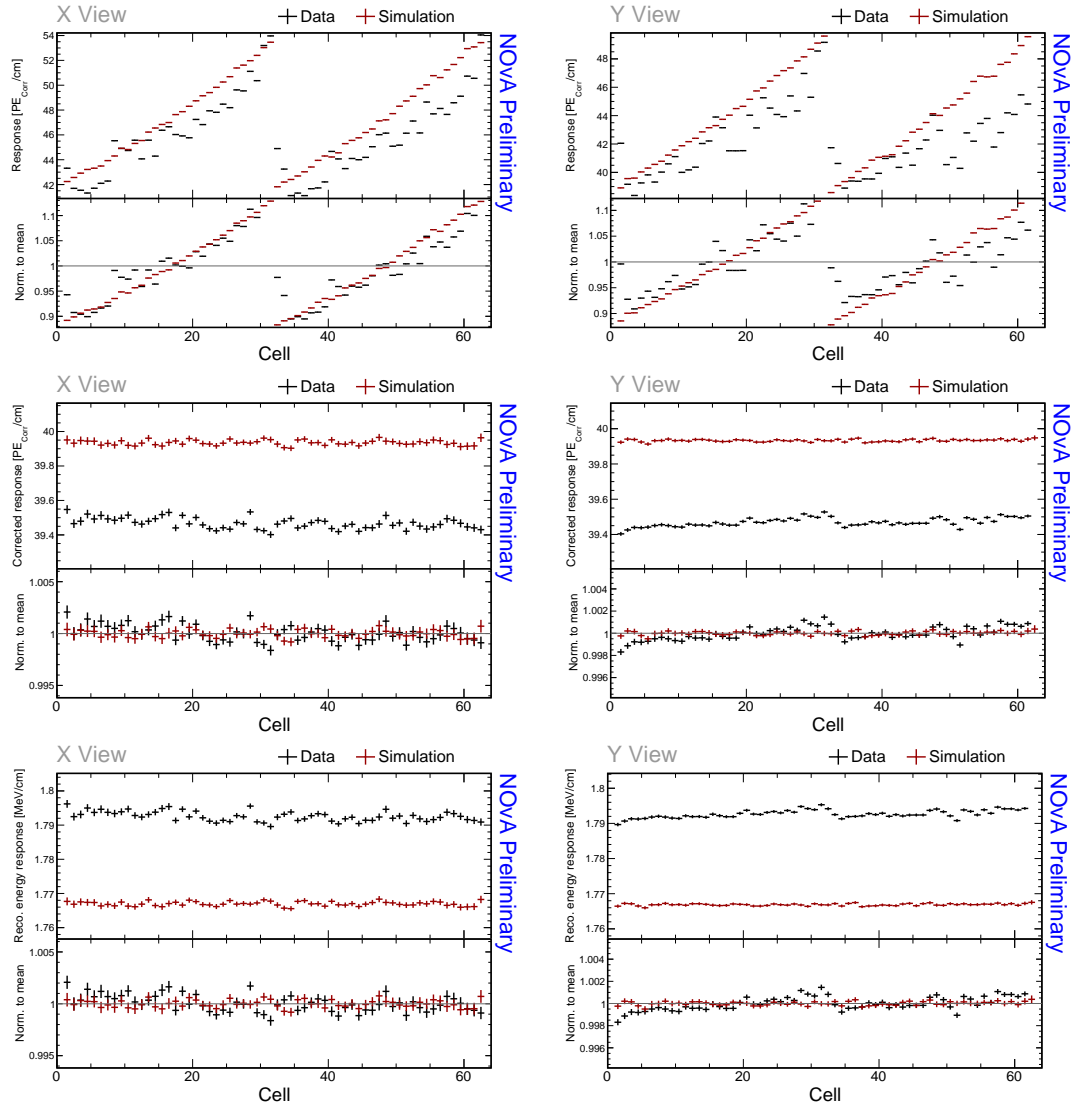


Figure A.12: Distributions of through-going cosmic muons with  $w \in (-80, 80)$  cm as a function of cell number for stable runs in the Test Beam period 4 data (black) and data-based simulation (red). Bottom panel of each plot shows the ratio of each bin and the mean y axis, separately for data and simulation.

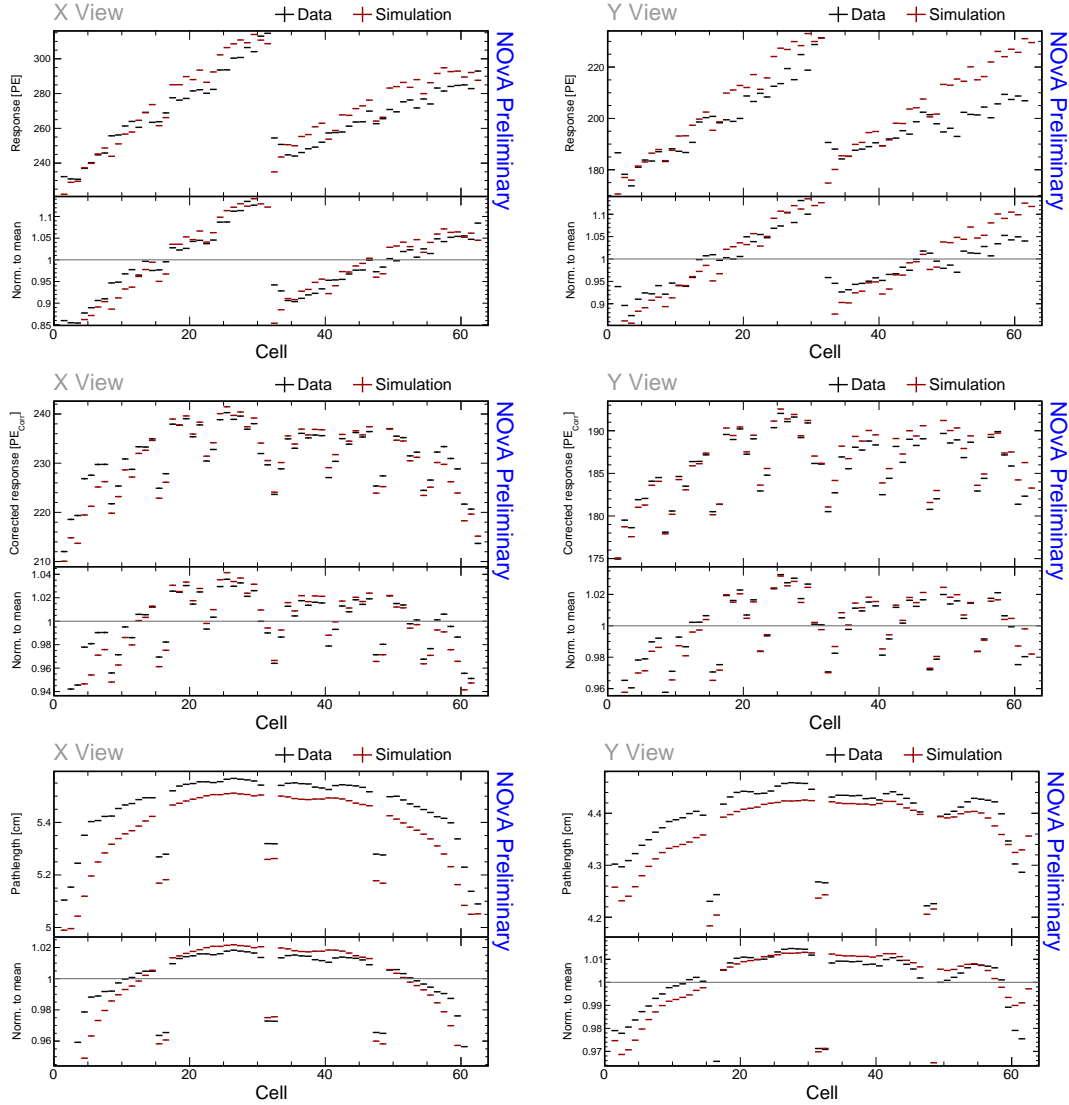


Figure A.13: Distributions of through-going cosmic muons with  $w \in (-80, 80)$  cm as a function of cell number for stable runs in the Test Beam period 4 data (black) and data-based simulation (red). Bottom panel of each plot shows the ratio of each bin and the mean y axis, separately for data and simulation.

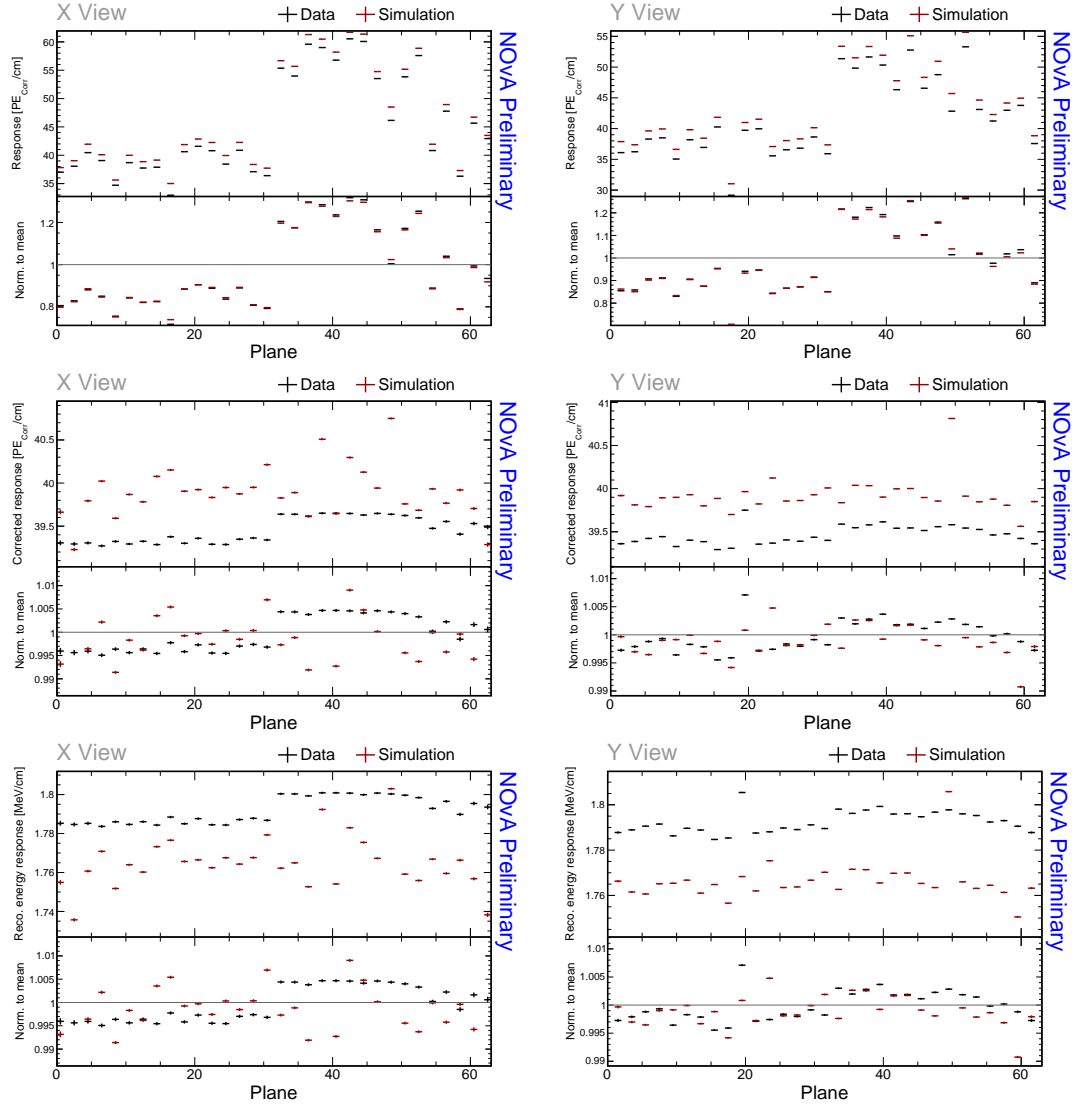


Figure A.14: Distributions of through-going cosmic muons with  $w \in (-80, 80)$  cm as a function of plane number for stable runs in the Test Beam period 4 data (black) and data-based simulation (red). Bottom panel of each plot shows the ratio of each bin and the mean y axis, separately for data and simulation.

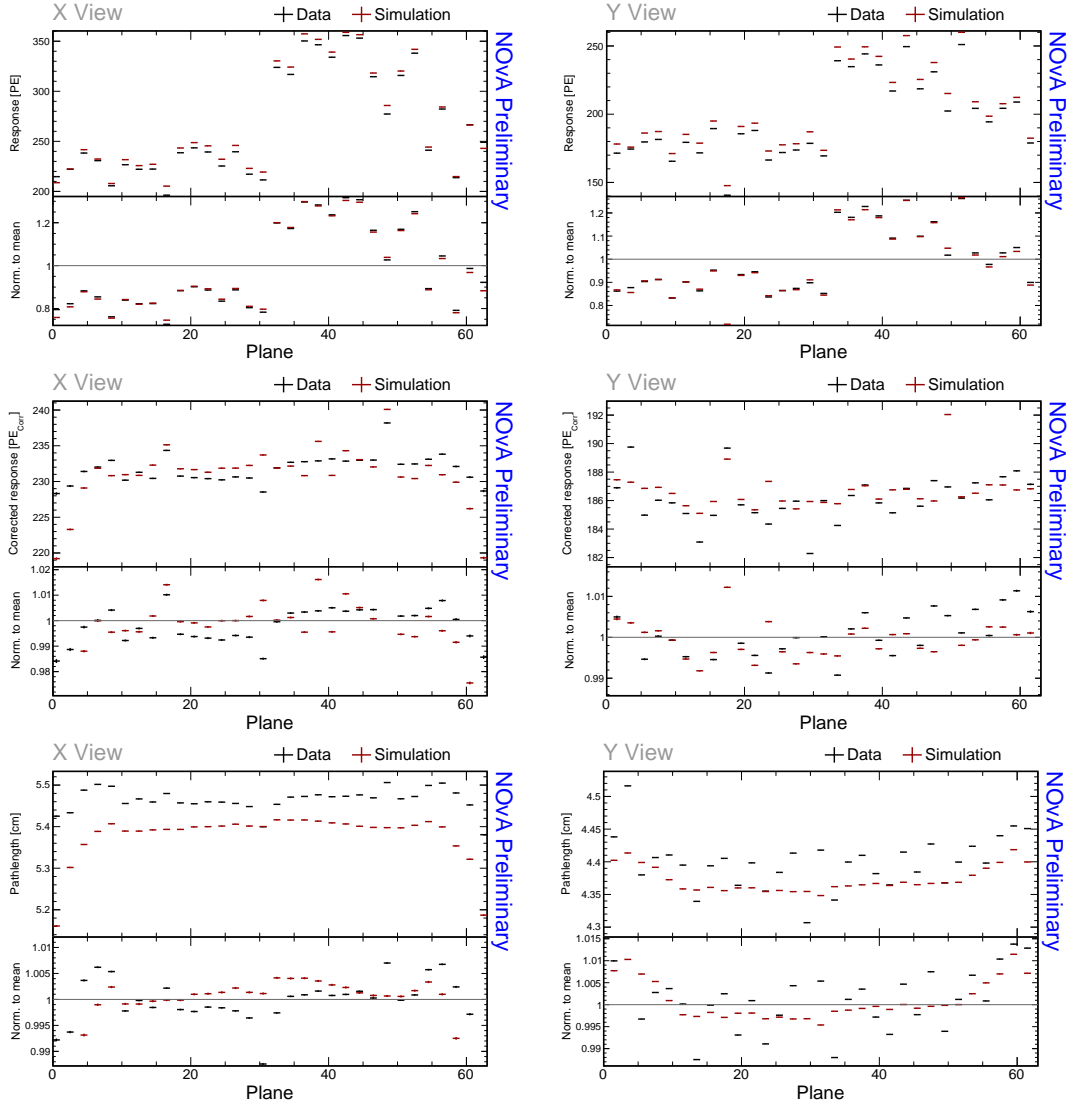


Figure A.15: Distributions of through-going cosmic muons with  $w \in (-80, 80)$  cm as a function of plane number for stable runs in the Test Beam period 4 data (black) and data-based simulation (red). Bottom panel of each plot shows the ratio of each bin and the mean y axis, separately for data and simulation.

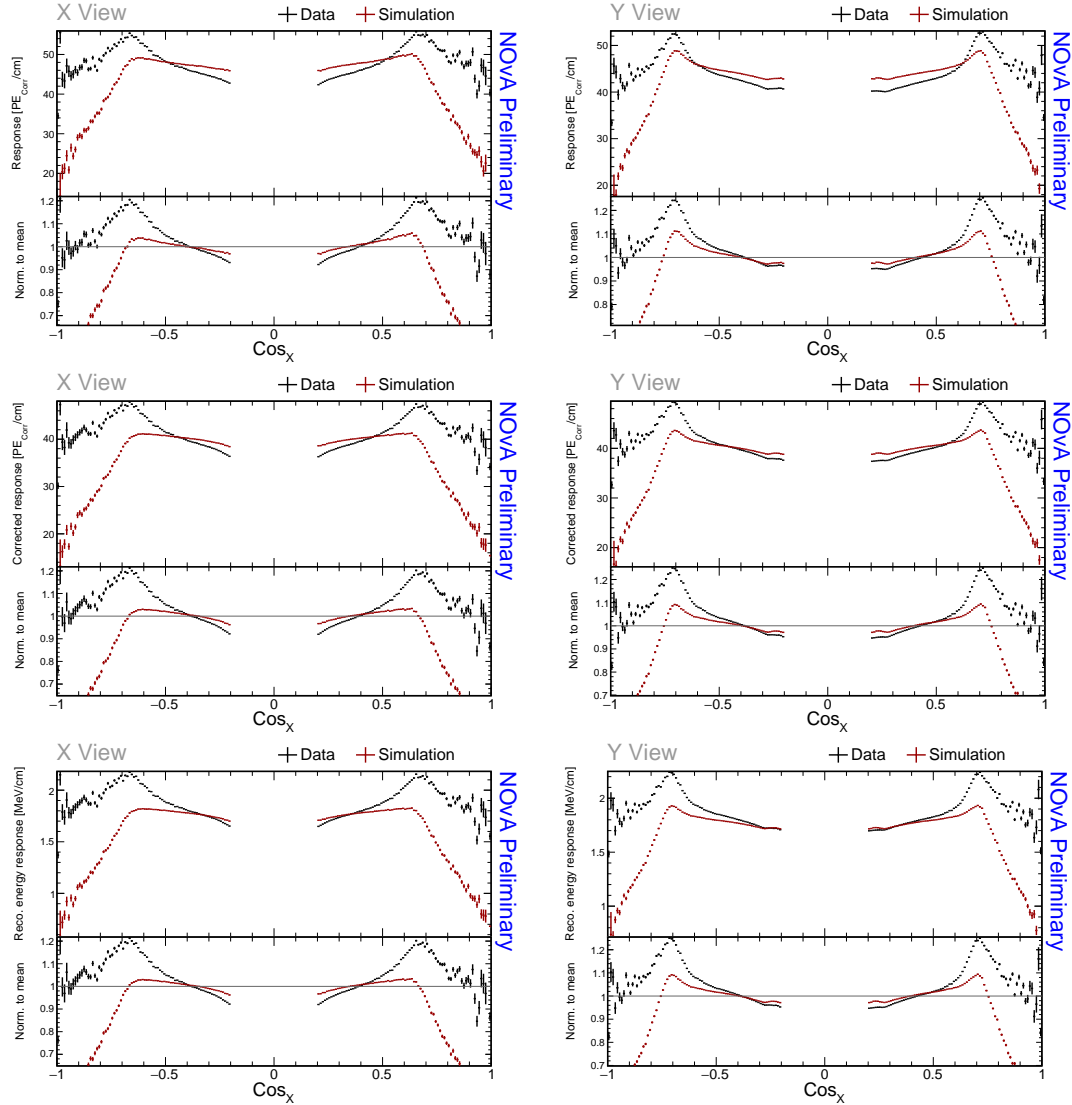


Figure A.16: Distributions of through-going cosmic muons with  $w \in (-80, 80)$  cm as a function of the cosine of the angle from the x axis for stable runs in the Test Beam period 4 data (black) and data-based simulation (red). Bottom panel of each plot shows the ratio of each bin and the mean y axis, separately for data and simulation.

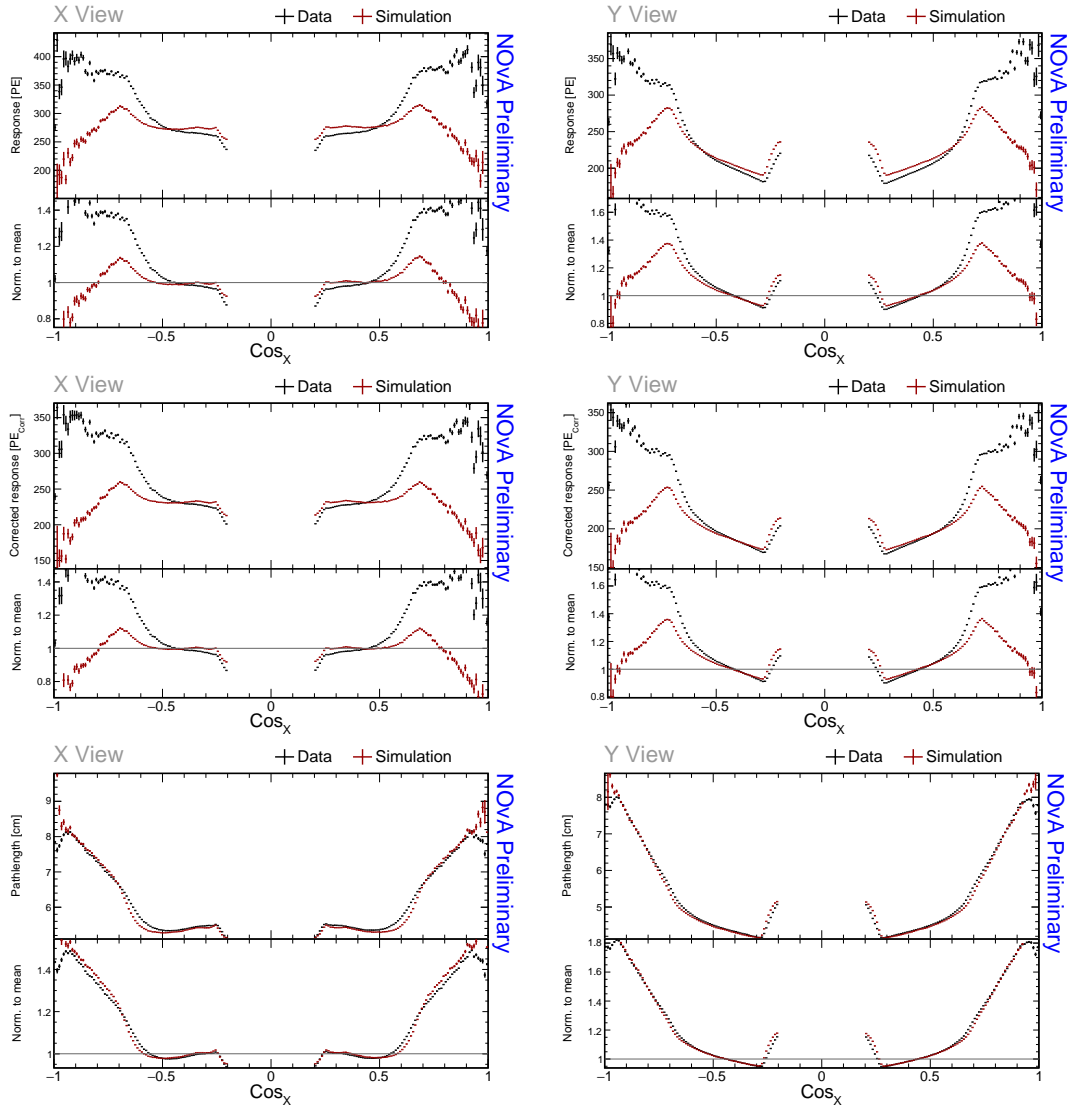


Figure A.17: Distributions of through-going cosmic muons with  $w \in (-80, 80)$  cm as a function of the cosine of the angle from the x axis for stable runs in the Test Beam period 4 data (black) and data-based simulation (red). Bottom panel of each plot shows the ratio of each bin and the mean y axis, separately for data and simulation.

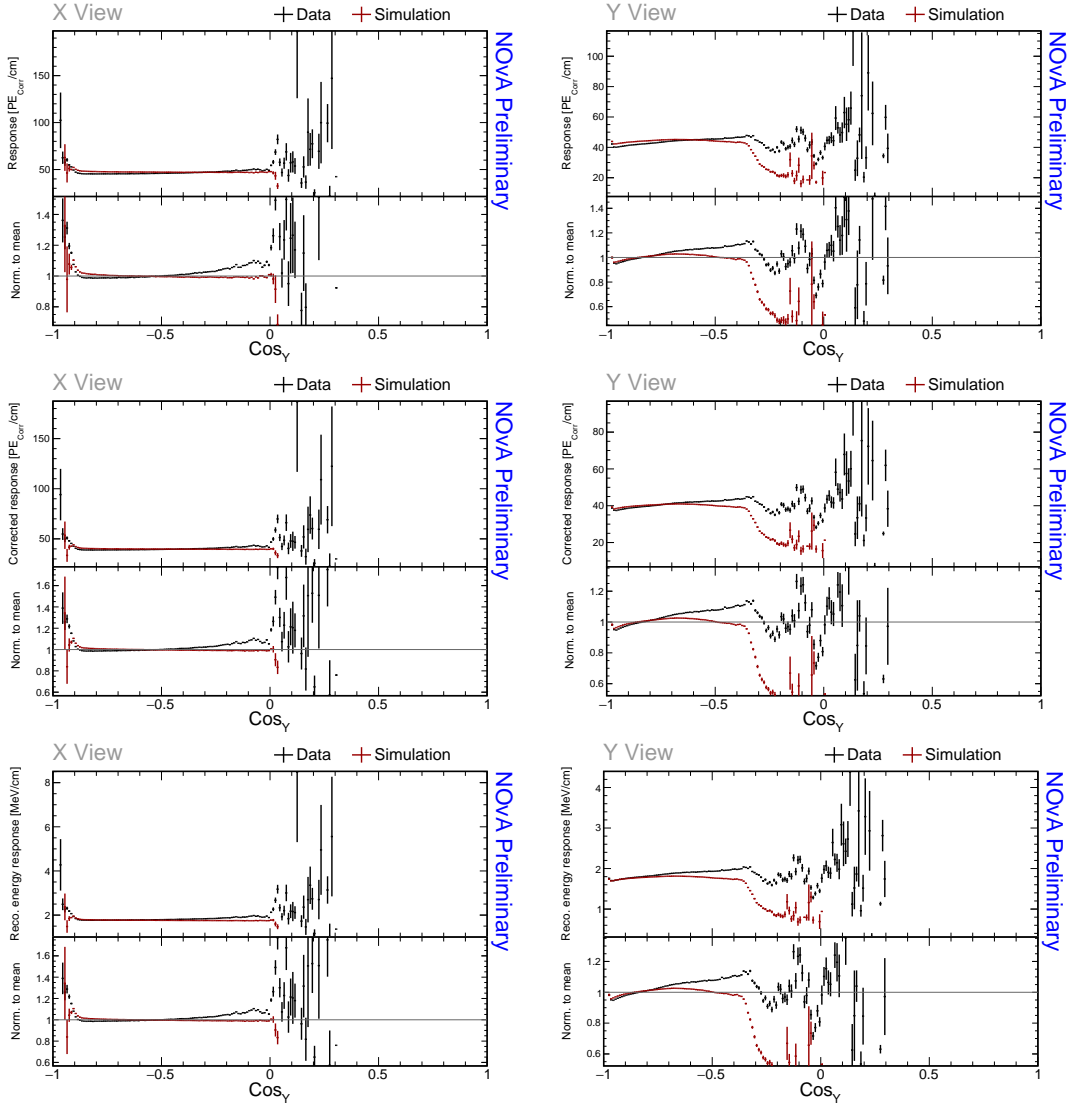


Figure A.18: Distributions of through-going cosmic muons with  $w \in (-80, 80)$  cm as a function of the cosine of the angle from the y axis for stable runs in the Test Beam period 4 data (black) and data-based simulation (red). Bottom panel of each plot shows the ratio of each bin and the mean y axis, separately for data and simulation.

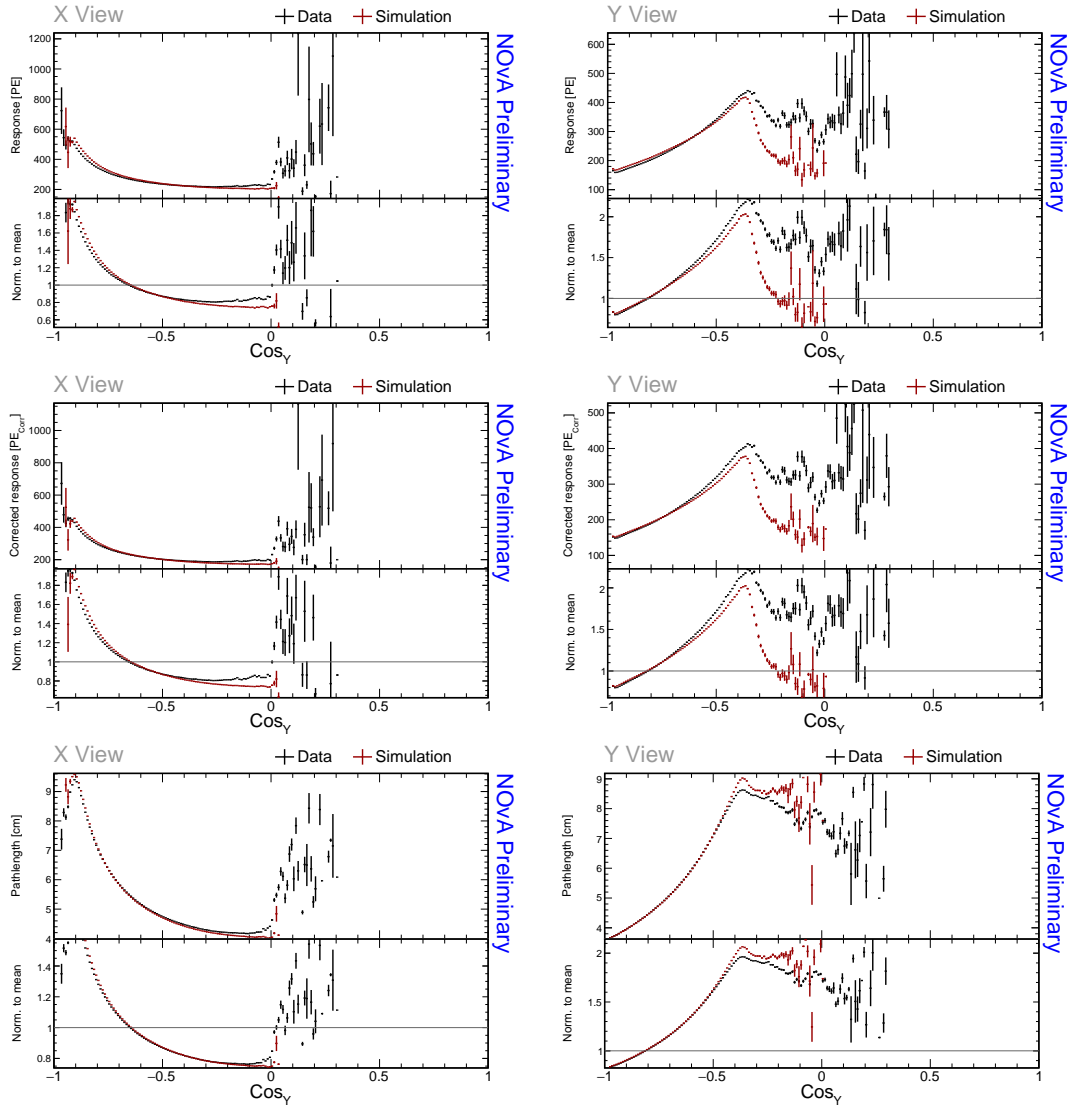


Figure A.19: Distributions of through-going cosmic muons with  $w \in (-80, 80)$  cm as a function of the cosine of the angle from the y axis for stable runs in the Test Beam period 4 data (black) and data-based simulation (red). Bottom panel of each plot shows the ratio of each bin and the mean y axis, separately for data and simulation.

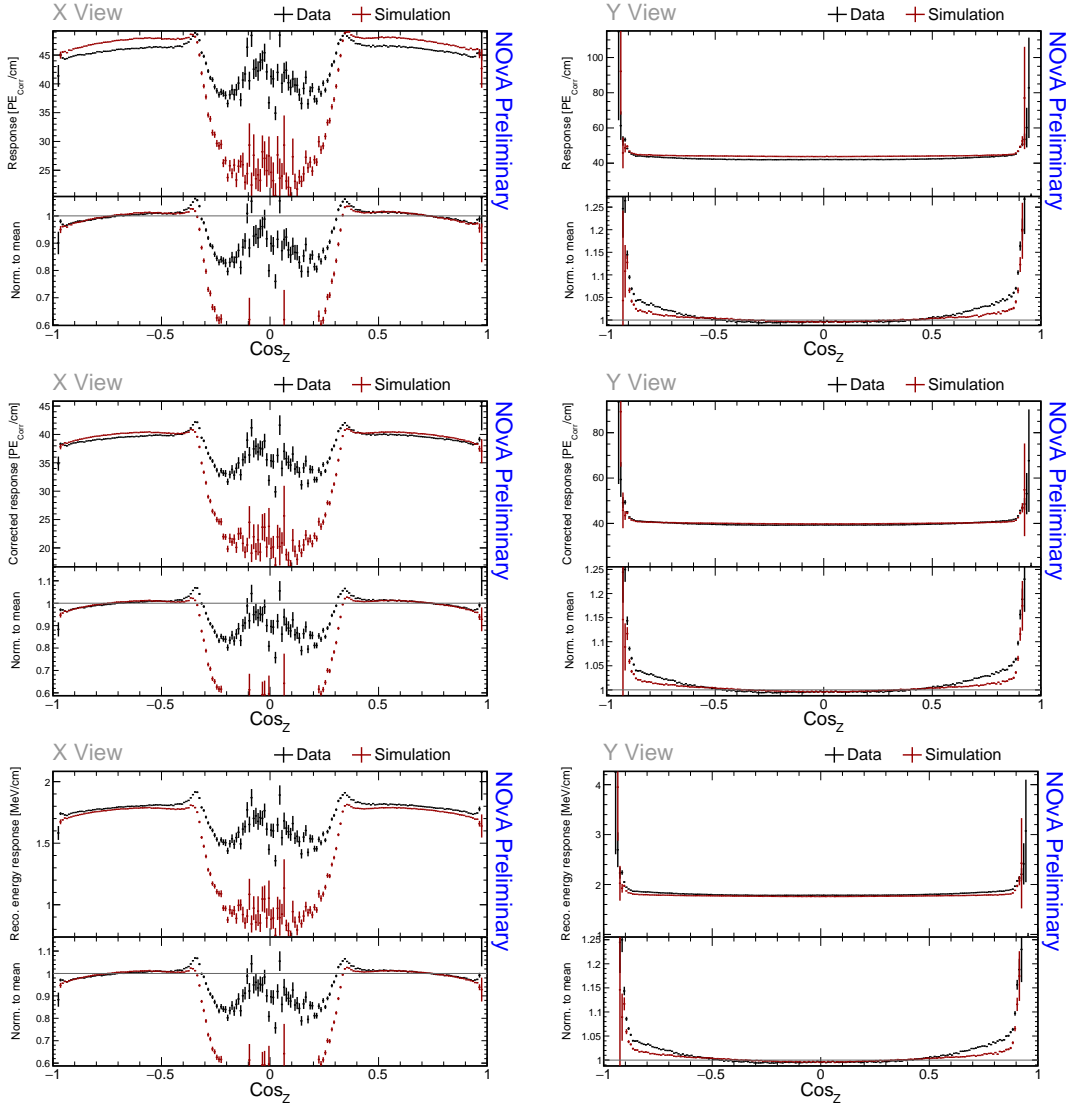


Figure A.20: Distributions of through-going cosmic muons with  $w \in (-80, 80)$  cm as a function of the cosine of the angle from the z axis for stable runs in the Test Beam period 4 data (black) and data-based simulation (red). Bottom panel of each plot shows the ratio of each bin and the mean y axis, separately for data and simulation.

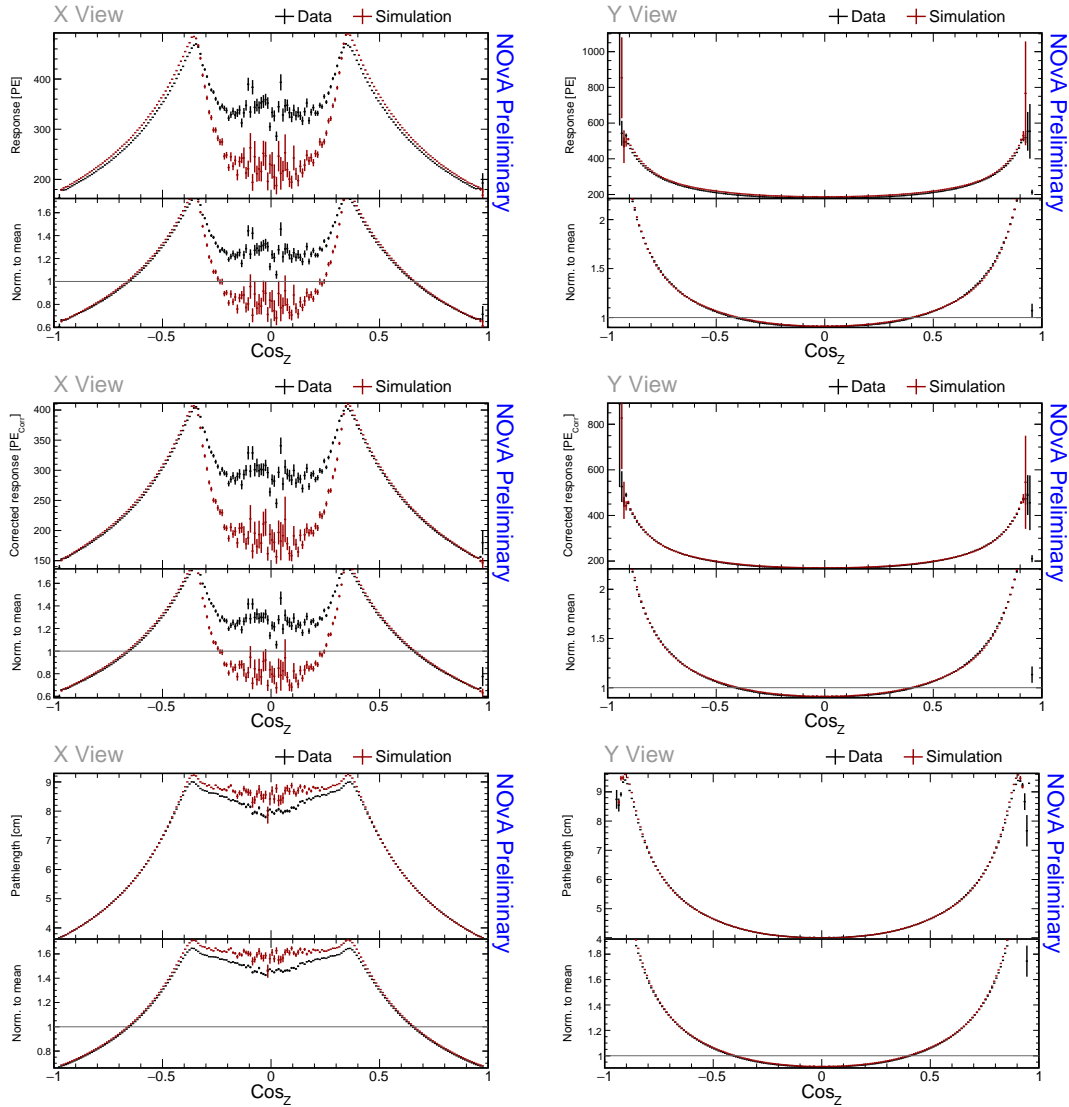


Figure A.21: Distributions of through-going cosmic muons with  $w \in (-80, 80)$  cm as a function of the cosine of the angle from the x axis for stable runs in the Test Beam period 4 data (black) and data-based simulation (red). Bottom panel of each plot shows the ratio of each bin and the mean y axis, separately for data and simulation.